Multi-scale modeling of the additive manufacturing of ceramics by vat photopolymerization

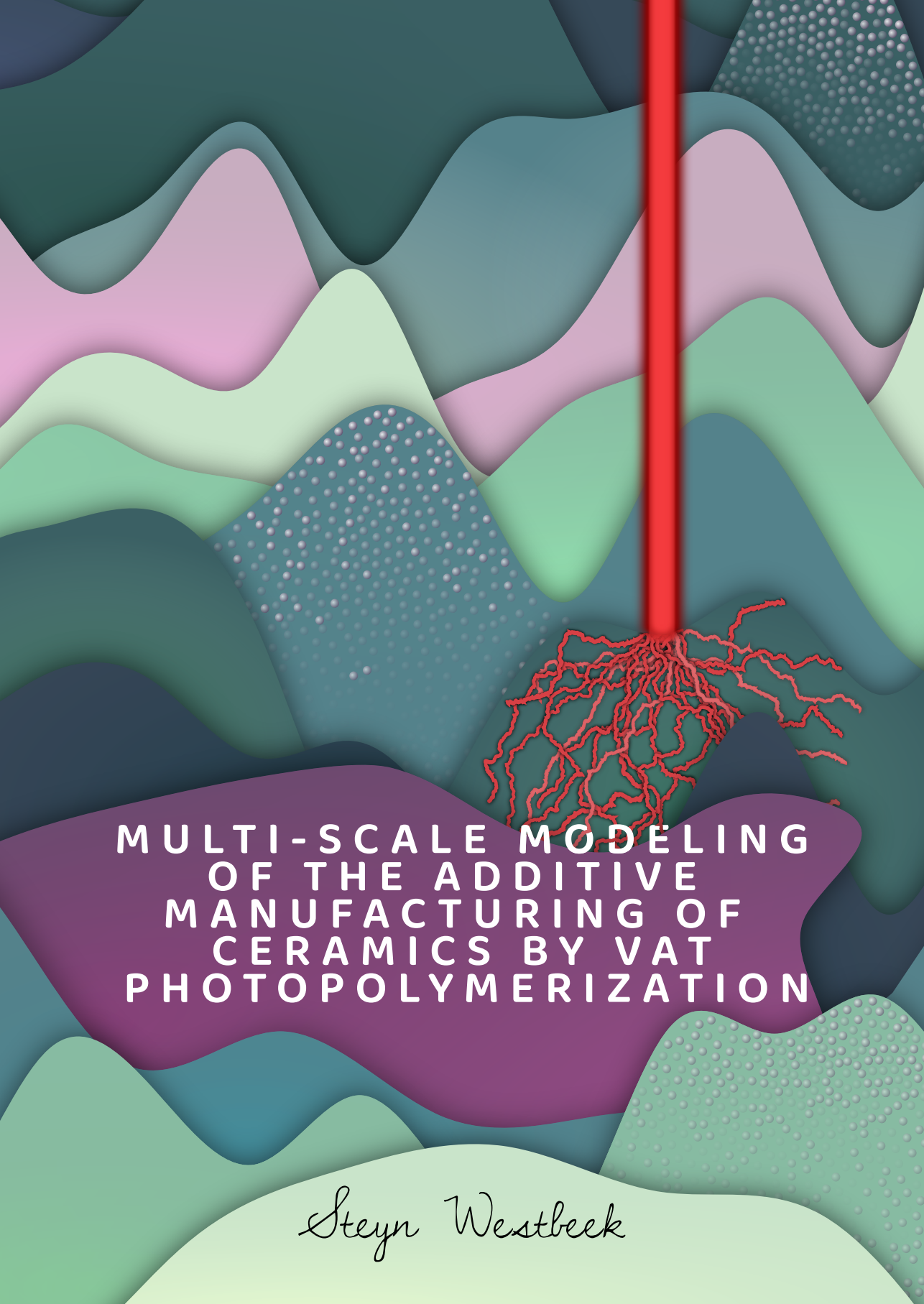

MULTI-SCALE MODELING OF THE ADDITIVE MANUFACTURING OF CERAMICS BY VAT PHOTOPOLYMERIZATION

Steyn Westbeek

Multi-scale modeling of the additive manufacturing of ceramics by vat photopolymerization

Steyn Westbeek

Multi-scale modeling of the additive manufacturing of ceramics by vat photopolymerization

Steyn Westbeek

A catalogue record is available from the Eindhoven University of Technology Library.
ISBN: 978-90-386-5127-9

Cover design by: Steyn Westbeek

Printed by: Off Page

Research financially supported by the TU/e Impuls program and carried out as part of the TNO-TU/e-HTSC AMSYSTEMS project on Additive Manufacturing of Ceramics.

Multi-scale modeling of the additive manufacturing of ceramics by vat photopolymerization

PROEFSCHRIFT

ter verkrijging van de graad van doctor aan de Technische Universiteit Eindhoven, op gezag van de rector magnificus prof.dr.ir. F.P.T. Baaijens, voor een commissie aangewezen door het College voor Promoties, in het openbaar te verdedigen op maandag 26 oktober 2020 om 16:00 uur

door

Steyn Westbeek

geboren te Tilburg

Dit proefschrift is goedgekeurd door de promotoren en de samenstelling van de promotiecommissie is als volgt:

voorzitter:	prof.dr. L.P.H. de Goey
1e promotor:	prof.dr.ir. M.G.D. Geers
copromotoren:	dr.ir. J.A.W. van Dommelen
	dr.ir. J.J.C. Remmers
leden:	prof.dr.ir. T.A.M. Salet
	prof.dr. E. Rank (TU München)
	prof.dr. I. Gibson (UT)
adviseur:	ir. G.E. van Baars (TNO Optomechatronics)

Het onderzoek of ontwerp dat in dit proefschrift wordt beschreven is uitgevoerd in overeenstemming met de TU/e Gedragscode Wetenschapsbeoefening.

"Life isn't about finding yourself. Life is about creating yourself"

George Bernard Shaw

Multi-scale modeling of the additive manufacturing of ceramics by vat photopolymerization

Summary

The unique properties of ceramics, such as excellent mechanical, thermal, electrical, or bio-compatibility characteristics, make them ideal material candidates in many high-tech or biomedical applications. A tailored design is of great benefit in these applications. Complex designs are difficult or even impossible to make using traditional manufacturing techniques, for which 3D printing/additive manufacturing (AM) provides the right answer. An excellent candidate AM technology for the printing of ceramics with high accuracy is vat photopolymerization (VP). Complex ceramic geometries that combine improved functionality and performance are already being printed using VP, however, the typical part dimensions are relatively small, i.e. in the order of cm^3. Upon increasing build volumes, reproducibility and part quality, e.g., geometrical warpage and formation of cracks, become critical limiting factors. It is believed that an enhanced understanding of the intricate AM process is key in overcoming these challenges and to enable large-area AM of ceramics.

This thesis pursues a computational multi-scale and multi-physical modeling approach to obtain an improved comprehension of the VP process for ceramics. One particular step in the ceramic manufacturing process is here of interest, i.e. the geometrical shaping in the 3D printer. In this VP-step, a polymer-ceramic composite part, the so-called "green" phase, is printed by selectively irradiating a photoactive resin with a UV light source in a layer-by-layer fashion. The pre- and post-processing steps, that involve preparation of the ceramic powder filled resin, the "slurry", and subsequent polymer debinding and ceramic sintering, are therefore outside the scope of this research. Previous (experimental) works already illustrated the broadening of the cure profile for ceramic filled resins. The goal of this modeling approach is to predict the corresponding light scattering and the development of residual stresses and deformations in the printed part, in relation to the raw material properties and the print process conditions.

In an initial study, the multi-physical nature of the VP process for ceramics is modeled on a sub-layer length scale. Starting from a flat-deposited layer, neglecting any rheological aspects, the difference in optical properties induces severe light scattering. All material points where the light penetrates experience photopolymerization, which leads to a phase transformation from liquid to solid. The solidification occurs at the expense of chemical shrinkage. Typically, the chemical reaction initiated by the UV light is of an exothermic nature, which, together with the absorption of light, increases the temperature of the resin, inducing a thermal expansion. The developed modeling framework provides a

direct coupling between the scattered light, via polymerization kinetics and temperature evolution, to the build-up of mechanical properties and residual stresses. The model reveals a profound influence of the inclusions on all the considered physics. Apart from the expected difference in mechanical and thermal behavior of the ceramic filled resin, an important finding is the fact that it appears to be difficult to obtain a homogeneous conversion throughout the slurry.

Capturing the broadening of the solidified contour caused by the scattering of light using analytical or numerical methods is not an easy task. The small difference in size of the powder inclusions in comparison to the wavelength of the UV light demands for an electromagnetic wave description that is solved using a finite element scheme to predict light propagation. To fully resolve the wavelength, a highly resolved finite element discretization is used. Consequently, accounting for a multitude of inclusions in the scattering problem is no longer feasible in a three-dimensional setting. The second part of this work establishes the relevance of two-dimensional simulations for the three-dimensional scattering problem at hand. By comparison of the two-dimensional results to equivalent three-dimensional shapes, a clear predictive value of the former is demonstrated.

The next stage in this thesis is the development of a new multi-scale modeling framework, bridging micro-, meso- and macroscopic length-scales. The thermo-mechanical behavior of the different constituents is incorporated at the micro-scale, whereas the light scattering and resulting conversion are evaluated at the intermediate meso-scale. Results from both length scales are homogenized towards an effective continuum, which is subsequently exploited for the simulation of the actual AM process at the macro-scale. This allows for a relatively coarsely discretized and therefore efficient part-scale simulation. Accounting for a section of the (filled) resin vat in an immersed setting enables prediction of key characteristics of the VP process, which would not have been possible using a more commonly used (initially) target geometry conforming pre-meshing technique.

In the final part of this work, the implemented modeling framework is validated in a qualitative sense. Where the multi-scale framework was initially applied to a scanning-laser (stereolithography, SLA) system, the applicability of the modeling framework to a full-area projection (digital light processing, DLP) type system is illustrated in this part. A three-dimensional comparison of (unfilled) printed parts with simulated results shows the importance of the multi-physical aspects on the resulting geometry.

Multi-schaalmodellering van het 3D printen van keramiek door middel van vat fotopolymerisatie

Samenvatting

De unieke eigenschappen van keramiek, zoals uitstekende mechanische, thermische, elektrische of biocompatibele eigenschappen, maken ze tot ideale materiaalkandidaten in vele hightech- of biomedische toepassingen. Een ontwerp op maat is in deze toepassingen van groot belang. Complexe ontwerpen zijn moeilijk of zelfs onmogelijk te maken met behulp van traditionele productietechnieken, waarvoor 3D printen/ additive manufacturing (AM) het juiste antwoord biedt. Een uitstekende kandidaat AM technologie voor het printen van keramiek met hoge nauwkeurigheid is vat fotopolymerisatie (VP). Complexe keramische geometrieën die verbeterde functionaliteit en prestaties combineren worden al geprint met behulp van VP, echter zijn de typische onderdeelafmetingen relatief klein, namelijk in de orde van cm^3. Bij toenemende bouwvolumes worden de reproduceerbaarheid en de kwaliteit van de onderdelen, bijvoorbeeld de geometrische vervorming en de ontwikkeling van scheuren, kritische beperkende factoren. De veronderstelling is dat een beter begrip van het ingewikkelde AM-proces de sleutel is tot het overwinnen van deze uitdagingen om groot-volume AM van keramiek mogelijk te maken.

Dit proefschrift streeft naar een numerieke multi-schaal en multi-fysische modellering om een beter begrip van het VP-proces voor keramiek te verkrijgen. Een specifieke stap in het keramische productieproces is hier van belang, namelijk de geometrische vormgeving in de 3D-printer. In deze VP-stap wordt een polymeer-keramisch composiet onderdeel, de zogenaamde “groene” fase, geprint door selectief en laag voor laag een fotoactieve hars met een UV-lichtbron te bestralen. De voor- en nabewerkingsstappen, die de voorbereiding van de met keramisch poeder gevulde hars, de “slurry”, en de daaropvolgende polymeerdebinding en keramische sintering omvatten, vallen dus buiten het kader van dit onderzoek. Eerdere (experimentele) werken illustreerden al de verbreding van het uithardingsprofiel van keramisch gevulde harsen. Het doel van deze modelleringsaanpak is het voorspellen van de bijbehorende lichtverstrooiing en de ontwikkeling van restspanningen en vervormingen in het geprinte deel, in relatie tot de eigenschappen van de gebruikte materialen en de condities van het printproces.

In een eerste studie wordt het multifysische karakter van het VP-proces voor keramiek gemodelleerd op een sublaaglengte schaal. Uitgaande van een vlakke gedeponeerde laag, waarbij geen rekening wordt gehouden met reologische aspecten, leidt het verschil in optische eigenschappen tot ernstige lichtverstrooiing. Alle materiaalpunten waar het licht doordringt ervaren fotopolymerisatie, wat leidt tot een fasetransformatie van

vloeibaar naar vast. De uitharding gaat ten koste van de chemische krimp. Meestal is de chemische reactie die door het UV-licht in gang wordt gezet van exotherme aard, wat samen met de absorptie van licht de temperatuur van de hars verhoogt. Dit veroorzaakt vervolgens een thermische uitzetting van het materiaal. Het ontwikkelde modelleerraamwerk biedt een directe koppeling tussen het verstrooide licht, via de polymerisatiekinetiek en de temperatuursevolutie, naar de opbouw van de mechanische eigenschappen en restspanningen. Het model toont een sterke invloed van de inclusies op alle beschouwde fysica. Naast het verwachte verschil in mechanisch en thermisch gedrag van de keramisch gevulde hars, is een belangrijke bevinding dat het moeilijk blijkt te zijn om een homogene conversie in de hele suspensie te verkrijgen.

Het vangen van de verbreding van de verharde contour, veroorzaakt door de verstrooiing van het licht, met behulp van analytische of numerieke methoden is geen eenvoudige opgave. Het kleine verschil in grootte van de poederdeeltjes in vergelijking met de golflengte van het UV-licht vraagt om een elektromagnetische golfbeschrijving die wordt opgelost met behulp van de eindige elementenmethode om de lichtverstrooiing te voorspellen. Om de golflengte goed te beschrijven wordt gebruik gemaakt van een gedetailleerde eindige-elementen beschrijving. Als gevolg daarvan is een veelvoud aan inclusies in het verstrooiingsprobleem niet meer haalbaar in een driedimensionale setting. Het tweede deel van dit werk stelt de relevantie vast van tweedimensionale simulaties voor het daadwerkelijke driedimensionale verstrooiingsprobleem. Door de tweedimensionale resultaten te vergelijken met equivalente driedimensionale vormen wordt een duidelijke voorspellende waarde van de eerste aangetoond.

De volgende fase in dit proefschrift is de ontwikkeling van een nieuw multischaal modelleringsraamwerk dat micro-, meso- en macroscopische lengteschalen overbrugt. Het thermo-mechanische gedrag van de verschillende bestanddelen wordt opgenomen op de microschaal, terwijl de lichtverstrooiing en de resulterende conversie worden geëvalueerd op de tussenliggende mesoschaal. De resultaten van beide lengteschalen worden gehomogeniseerd naar een effectief continuüm, dat vervolgens wordt gebruikt voor de simulatie van het eigenlijke AM-proces op macroschaal. Dit maakt een relatief grove discretisatie en dus efficiënte productschaal simulatie mogelijk. Door een deel van het vat met daarin (gevulde) hars in een (initieel) vloeibare toestand te beschouwen, kunnen de belangrijkste kenmerken van het VP-proces worden voorspeld. Dit zou niet mogelijk zijn geweest met behulp van een meer algemeen gebruikte (in eerste instantie) geometrieconforme discretisatie van de beoogde geomerie.

In het laatste deel van dit werk wordt het geïmplementeerde modelleringsraamwerk in kwalitatieve zin gevalideerd. Waar het multischaalraamwerk in eerste instantie werd toegepast op een scannende-laser (stereolithografie, SLA) systeem, wordt in dit deel de toepasbaarheid van het modelleringsraamwerk op een volledig oppervlak belichting (digital light processing, DLP) type systeem geïllustreerd. Een driedimensionale vergelijking van (ongevulde) geprinte onderdelen met gesimuleerde resultaten toont het belang van de multi-fysische aspecten op de resulterende geometrie.

Contents

Nomenclature

α	Absorption/attenuation coefficient [$^{1}/_{m}$]
γ	Electric conductivity [Sm]
∂	Layer thickness [m]
ΔH	Polymerization heat [$^{J}/_{mol}$]
ε	Electrical permittivity [$^{F}/_{m}$]
$\boldsymbol{\varepsilon}$	Strain tensor [-]
ϵ	Exposure [$^{J}/_{m^2}$]
ζ	Wave number [$^{rad}/_{m}$]
θ	Rotation angle [°]
ι	Resin/process constant affecting inhibition [$^{W}/_{m^2}$]
$\varkappa$	Extinction coefficient [-]
λ	Wavelength [m]
μ	Magnetic permeability [$^{H}/_{m}$]
ν	Poisson's ratio [-]
Π	Pixel pitch, i.e. the distance between the centers of two adjacent pixels [m]
ρ	Volumetric mass density [$^{kg}/_{m^3}$]
σ	Stress tensor [Pa]
τ	Temporal width of the Gaussian "bell" shape [s]
τ_d	Time delay [s]
υ	Thermal expansion coefficient [$^{1}/_{K}$]
φ	Particle filling/volume fraction [-]
ψ	Quantum yield for initiation [-]
ω	Angular frequency [$^{rad}/_{s}$]
a	Molar absorptivity [$^{L}/_{mol\,m}$]
$\mathcal{A}$	Area [m^2]
$\mathcal{B}$	Conversion scaling parameter [-]
c	Speed of light [$^{m}/_{s}$]
c_p	Heat capacity [$^{J}/_{(kg\,K)}$]
C_d	Cure depth [m]
C_w	Cure width [m]
${}^4\boldsymbol{\mathcal{C}}$	Fourth-order elastic stiffness tensor [Pa]
D_p	Penetration depth where the irradiance has reduced to e^{-1} of the initial value [m]
$\mathfrak{e}$	Emissivity [-]
e_0	Initial multiplication factor of the resin's stiffness [-]
E	Young's modulus [Pa]
$\vec{E}$	Electric field [$^{V}/_{m}$]
$\mathcal{E}_p$	Conversion based intensity effectiveness [-]
g	Gravitational acceleration (9.81) [$^{m}/_{s^2}$]
h	Convective heat transfer coefficient [$^{W}/_{m^2K}$]
$\vec{H}$	Magnetic field [$^{A}/_{m}$]
I	Intensity/irradiance [$^{W}/_{m^2}$]
$\boldsymbol{I}$	Unit tensor [-]
$\mathcal{I}_I$	Intensity inhomogeneity [-]
$\vec{J}$	Electric current [V]
k	Thermal conductivity [$^{W}/_{(m\,K)}$]
k_t	Termination rate constant [$^{L}/_{(mol\,s)}$]
k_p	Propagation rate constant [$^{L}/_{(mol\,s)}$]
$_m$	Denotes a parameter belonging to the *micro*-scale
$_\mathcal{M}$	Denotes a parameter belonging to the *meso*-scale
$_M$	Denotes a parameter belonging to the *macro*-scale
n	Refractive index [-]
p	Conversion level of polymerization [-]
$\mathcal{P}$	Polymerization constant [$^{m}/_{\sqrt{W}}$]
$\mathcal{S}$	Stefan-Boltzmann constant (5.67×10^{-8}) [$^{W}/_{(m^2K^4)}$]
$\vec{S}$	Poynting vector [$^{W}/_{m^2}$]
t	Time [s]
T	Temperature [K]
V	Volume [m^3]
w_0	Intensity distribution's $^{1}/_{e^2}$ Gaussian half-width [m]
$[x]$	Concentration of species x [$^{mol}/_{l}$]

1 Introduction

Ceramics are one of the oldest materials made by humans and advanced ceramics—besides metals and polymers—represent one of the most promising classes of materials for the key technologies of the twenty-first century [1, 2]. By definition ceramics are inorganic materials, which are typically crystalline in nature and contain metallic and non-metalic components. As a result, ceramics typically show brittle behavior at room temperature, poor electrical and thermal conductivity, high hardness and strength, with favorable load-bearing capability in compression compared to tensile loading, insensitivity in harsh chemical and thermal environments and biocompatibility [1]. By utilizing these unique properties, ceramics can potentially save energy, reduce wear, and increase the lifetime of components in a broad range of applications [3]. In an attempt to give an overall impression, one might think of applications in wear-resistant coatings, cutting tools, engine/turbine components, spacecraft insulation tiles, packages for integrated circuits or biomedical applications such as hip implants [1].

Advanced (also referred to as technical) ceramics have, however, always been challenging to shape and process, which can be attributed to their characteristic properties. To mitigate this and to tailor the fabrication process to the intended component, over 70 ways to fabricate ceramics exist—all with certain advantages and disadvantages [1, 4]. These processes can be divided into 'dry' and 'wet' processes. In 'dry' processes, the ceramic powder is processed directly before it is sintered—*sintering* is the process of forming a solid mass of material by heat or pressure without liquefaction. The second class, i.e. the 'wet' process, is more common. In this category of processes, a liquid is added in the shaping process, cf. the water added in the forming process of clay before it is fired. An alternative common addition that acts as a 'wet' binder material is a liquid polymer. The most commonly used shaping processes include slip casting, dry pressing, tape casting, gel casting and injection molding [5].

A number of disadvantages can be identified for these processes in view of using them for the fabrication of complex geometries. To accurately form the component,

(high-precision) molds are required. This makes the fabrication process suitable for mass production, but not for prototypes or limited series [3]. Additionally, after shaping and sintering the component into a final dense form, mechanical post-processing may still be required. Due to the high strength/hardness of ceramics, this requires highly specialized tools. The actual associated cost of this post-processing varies, but may constitute up to 80% of the total manufacturing costs [6]. Lastly, although the usage of molds allows for considerable design freedom, certain shapes, e.g., cavities, inner bores and grooves and small angled bends, remain difficult to realize [7].

Additive manufacturing (AM) can overcome each of these issues. Many potential application areas of ceramics greatly benefit from the additional design flexibility and the convenience of small series production. These range from microsystems, such as labs/organs-on-a-chip [8], intricate scaffolds for tissue engineering [9], microelectro-mechanical systems (MEMS), photonic crystals [10] or large(r) scale applications such as jewelry, personalized biomedical implants with open cellular structures or dental applications [10–12], heat-exchangers with complex shaped integrated cooling channels [13, 14], turbine blades and mechanically durable (but lightweight) structures [15, 16] in a broad sense. Some polymer derived ('wet') ceramic examples fabricated using AM are shown in Fig. 1.1.

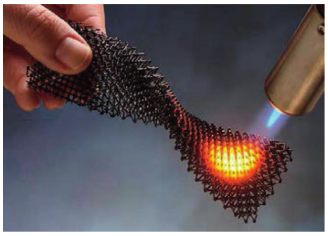

(a) SiC ceramic mesh [17]

(b) Zirconia dental crowns [18]

(c) Alumina heat exchanger [14]

Figure 1.1 Examples of polymer derived ceramics (using the AM technique vat photopolymerization).

1.1 Additive manufacturing of ceramics

Although additive manufacturing, or the more popular terminology: 3D printing, might seem like a very recent technology, it originated in the 1980s with the filing of multiple patents (in parallel in both Japan, France and the USA) that described the generation of a three-dimensional geometry by selectively adding material one layer at a time [19]. To a large extent, this describes the very essence of AM, i.e. translating a virtual geometry into physical objects in a direct fashion. A key aspect of AM is that the virtual-to-physical translation takes place—regardless of geometrical specifications—without having to adjust the manufacturing process itself. Additionally, AM saves the costs associated with expensive molds and/or enables the production of designs that cannot

be molded or fabricated otherwise. To do so, typically, the virtual volume is divided into a series of two-dimensional cross-sections with a finite thickness that are fed into the AM apparatus. The most prominent differences that distinguish one AM technology from the other are the used material and (inter- and intra-) layer-bonding method. The most generally accepted grouping method (adopted into ASTM and ISO standards) is based on commonality in machine architecture and material transformation physics and defines 7 process categories [19], which are:

- Vat photopolymerization; uses a vat of liquid photopolymer resin that is cured, i.e. solidified, by a selective supply of energy.
- Powder bed fusion; where powder material in a container is directly sintered or melted together.
- Material extrusion; an extrusion process using a nozzle to directly deposit material in a certain pattern.
- Material jetting; which is equivalent to regular ink-jet printing in a multi-layered fashion.
- Binder jetting; a process which combines a powder bed with a jetting process. The binder material is selectively added to generate the bonded cross-section.
- Sheet lamination; starts with sheets of material which are deposited one at a time.
- Direct energy deposition; uses a combined energy and material deposition device to, respectively, process and deposit the material simultaneously.

In principle, techniques exist in all of these categories that can be used to produce ceramic components [7, 16, 20–22].

The technique that is considered in this thesis is vat photopolymerization (VP), which provides considerable benefits regarding surface finish and resolution [23, 24]. The basic principle of VP is illustrated in Fig. 1.2. The process starts with the deposition of a layer of a photoactive resin, as indicated in Fig. 1.2a. There are numerous techniques to do so, all devised in attempts to generate an as-flat-as-possible layer [25]. After this so-called *recoating*-step—the step where an untreated coating, i.e. layer, is (re-)applied—irradiation (Fig. 1.2b) starts. By irradiating selectively with UV-light, the photopolymerization reaction is initiated in the intended areas, thus only solidifying the component's cross-section. Figure 1.2 illustrates the irradiation process for a scanning-laser based approach; an alternative approach is a projection-based system which cures an entire layer at once [26]. After a layer is completely irradiated, the build platform moves downwards (Fig. 1.2c) and the process repeats itself (Fig. 1.2d-f), layer after layer. In contrast to the free-surface and top-down irradiation system depicted in Fig. 1.2, inverse systems also exist. In these so-called bottom-up or constrained-surface systems, the component is suspended to the build-plate which moves upwards, while the irradiation originates from underneath a transparent base of the vat.

In order to use this (polymer-based) process for the fabrication of ceramic components, a number of pre- and post-processing steps are required, as indicated in Fig. 1.3. The different process steps will be elaborated in the following, with analogies to conventional techniques to provide some common ground in processing of ceramics.

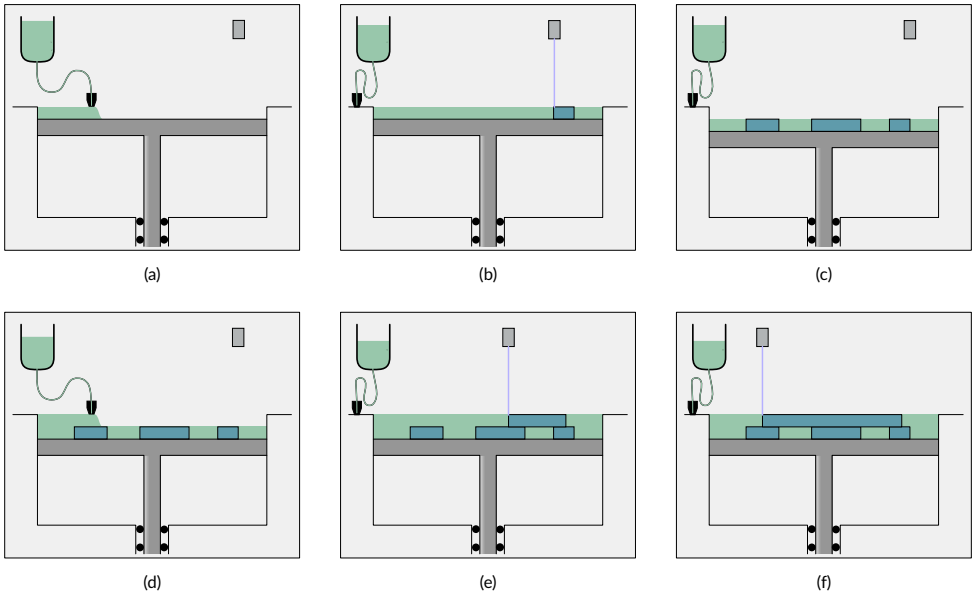

Figure 1.2 Illustration of the VP process. The process starts with the deposition of a layer of resin (a), after which selective irradiation starts (b,c). As soon as the layer is completed, the build plate moves downward and the process repeats itself (d-f).

Whereas the regular VP process starts with a UV-curable resin, which typically consists of a monomer and a photoinitiator, a high solid loading of ceramic powder is dispersed into the resin in the initial process step for VP of ceramics. The resulting highly viscous fluid is termed a *slurry* and serves as feed material into the VP process. Additional components that may be added to the resin/slurry to tailor illumination properties or facilitate the recoating behavior are, e.g., an inert dye, diluent, dispersant and/or plasticizing agent [27–29]. The preparation of a powder filled suspension is essentially a form of gel casting [30]. For successful subsequent post-processing, a ceramic volume fraction of at least 50 vol.% is required. The second step in the process is the actual printing process, cf. Fig. 1.3, which in its simplest form represents a repetitive tape casting process, where a very thin and uniform layer of slurry is (also) deposited by a recoater and then

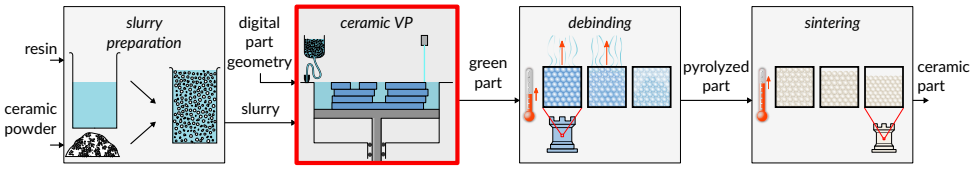

Figure 1.3 Overview of the steps involved in the ceramic additive manufacturing process through vat photopolymerization. This thesis solely focuses on the highlighted ceramic VP process.

solidified [5, 31]. As soon as the final layer is cured and the AM process is completed, the printed parts—a build job typically contains a large number of components, closely packed together—need to be harvested from the build-plate and uncured slurry should be removed in a cleaning step. What remains are polymer-ceramic composite parts in the *green* phase, which is an intermediate phase in the ceramic forming process. This concludes the geometrical shaping step in the fabrication process of ceramics. Two post-processing steps are still required, as illustrated in Fig. 1.3. Firstly, the polymer binder material is removed in a *debinding* step at an elevated temperature, i.e. through pyrolysis; a subsequent high-temperature sintering provides the final ceramic component [32–35]. Shrinkage occurs during the transformation from polymer matrix with powder filler to the (ideally fully dense) solid ceramic component. These steps equally apply to the ceramic injection molding process [31].

Provided that extensive knowledge is available on the pre- and post-processing steps in the field of polymer-derived ceramics, this thesis solely focuses on the additive manufacturing step itself, i.e. as highlighted in Fig. 1.3. This choice is further motivated by the finding that the green body formation is of utmost importance for the quality of the resulting ceramic component, as each defect introduced in this phase persists even after successful sintering [36].

The VP process is a very interesting process from many points of view—even more so with a powder filler. Regarding the length-scales in the printer, the smallest relevant dimension is either the UV wavelength (~400 nm) or the size of the powder inclusions, depending on the slurry formulation [37]. Subsequent relevant length-scales originate from the AM process, i.e. layer thicknesses are tens of μm, while multi-layer part sizes may reach (many) cms.

Based on the multitude of relevant physics, ceramic VP is a particularly intriguing process. In a traditional VP process, the relevance of the wavelength is limited to the absorption efficiency of the photoinitiator. For filled resins, this is a relevant parameter for light scattering as well, as the magnitude of the light scattering is dominated by the difference in characterstic length-scale of the inclusion and the light's wavelength [38, 39]. Additionally, the contrast between the refractive index of the resin and the ceramic inclusion plays a prominent role [31, 40–43]. As shown experimentally, the resulting cured polymer geometry can be considerably different from the expected geometry—based on the input light source and the unfilled resin's absorption. Typically, in ceramic filled resins, the solidified contour becomes (much) wider while its depth reduces. This broadening effect is illustrated in Figure 1.4 [31]. Light penetrating into the resin/slurry induces the photopolymerization reaction, transforming monomers to long-chained polymers.

The resulting mechanical properties of the green part are determined by the progress (and even trajectory) of the chemical reaction, i.e. the *degree of conversion*, and the molecular structure of the polymer formed, in terms of the amount of crosslinking between the (long) polymer chains [23, 44–50]. In the end, the presence of residual monomer is highly undesirable in the printed component [51]. The

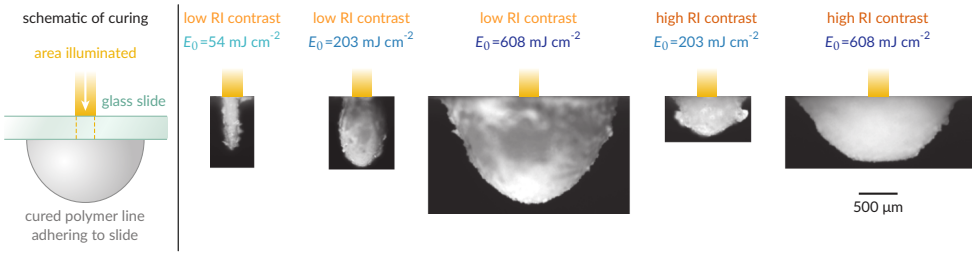

Figure 1.4 Solidified contour for silicon dioxide (SiO_2) using two different resins with varying refractive index, i.e. low and high contract with the powder filler. Additionally, the effect of different energy doses (E_0) is depicted. Slightly adapted from [31].

photopolymerization reaction itself is an exothermic reaction [44]—which, as such, generates heat—and induces shrinkage by a reduction of inter-molecular spacing [52, 53]. While the matrix material evolves upon irradiation by the light source, from a mechanical point of view the solid inclusions are inert. Concerning the temperature evolution, the inclusions (mainly) serve as a heat sink.

These contradictions make the multi-physical process even more intricate. This is also illustrated by the recoating step, where a higher viscosity needs to be considered and the presence of solid inclusions increases the shear forces [16].

A similar assessment can be made on the relevant time-scales. The transit time of light, i.e. a photon, through a layer is of the order of a picosecond (~10^{-12} s), whereas the kinetic reaction duration is typically in the order of (several) microseconds (~10^{-6} s) for a laser scanning system and up to (a few) seconds for a projection-based system, due to the lower intensity input [19, 54]. It is expected that other physical phenomena are coupled to the reaction time. As soon as the layer irradiation is completed, a new layer is added and the process is repeated at another relevant time-interval, until the component is completed—after the largest relevant time-scale.

1.2 Scope, state-of-the-art and objective

The complex multi-scale and multi-physical nature of the vat photopolymerization process for ceramics is not sufficiently understood. Key challenges that limit the adoption of AM for the fabrication of ceramics are to increase the monolithic part density, printable component size and wall thicknesses, to prevent crack formation and the requirement to print 'predictive' geometries [16]. Examples of defects that occur in the ceramic VP process are illustrated in Figure 1.5 [23, 28, 45, 55]. For AM in general, the variation in product quality from part-to-part and print-job-to-print-job, i.e. repeatability, and the speed of the printing process, i.e. productivity, are limiting factors. In order to advance the current state-of-the-art of AM, modeling, sensing and control are considered of utmost importance [57].

The research in this thesis is part of a triptych, which combined covers all these focus

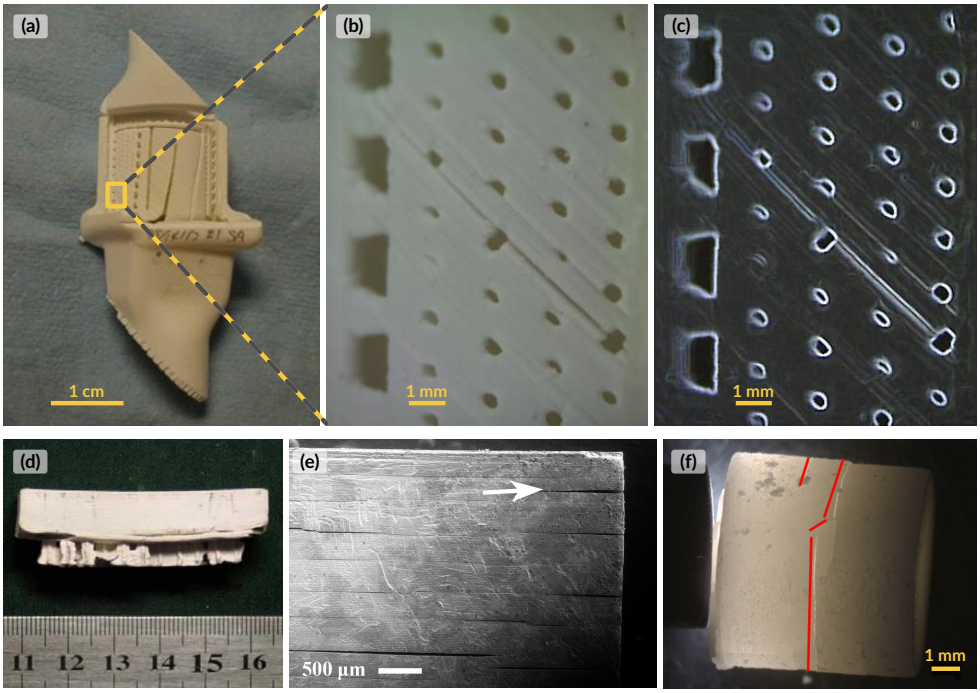

Figure 1.5 (a) and (b) show an airfoil mold in the green phase, with a silica powder filler. The crack shown in the close-up view in (b) is depicted after sintering in (c). Slightly adapted from [55, 56]. An example of warpage is shown in (d) for silica in the green phase [45]. (e) provides an example of debonding in a post-sintered alumina sample (note that 25 µm thick layers were used in the VP process) [28]. A cracked zirconia sintered sample is shown in (f) [23].

areas. Firstly, the work of Kozhevnikov et al. [58, 59] addresses the modeling of the recoating process. Bottom-up VP systems provide a nice flat layer, but as soon as the cross-sectional area increases the bonding force becomes too high. In a top-down system the latter issue is resolved, but it becomes more challenging to obtain a flat layer, which is where the modeling approach comes in. The second research line, i.e. the work of Hafkamp et al. [25, 60–62], uses a systems engineering approach to integrate sensing and control into the VP apparatus, with the focus mainly directed towards the (closed-loop control of the) photopolymerization reaction. The research in this thesis completes the triptych—it might be considered the middle section, with respect to the other two research lines—through the modeling of the photopolymerization process. With the use of a dedicated finite element model, the photopolymerisation process will be simulated to obtain a physically based description of the mechanical properties of the printed, green product. The motivating assumption herein is that the quality of the green product, i.e. its structural properties, the presence of residual stresses and thermal effects, is of paramount importance for the final product.

Essentially, the application of numerical modeling approaches to improve the understanding of the VP process (for unfilled resins) is not new. A broad range of techniques—both mathematical and numerical—has been applied by several authors, starting from Jacobs' cure depth (exposure threshold) model [54]. In subsequent works, a distinction can be made between two different alternative approaches. Attempts to *(i)* capture the effect of the layered nature of the AM process (using the finite element method) while considering individual layers as homogeneous [55, 63–65] or those that *(ii)* incorporate more detailed physics affecting the spatial evolution of the degree of conversion as a function of the illumination source [66–75]. Whereas the first category of approaches is applicable for AM in general, the latter type of models is tailored towards VP. Examples that attempt a similar approach for powder filled resins are more scarce. A notable exception is Ref. [76], where experimental work is used to determine the apparent irradiation characteristics of the filled resin in order to predict the solidified contour. More common are empirical approaches that account for the presence of inclusions—and for the associated broadening (and shallowing) of the cure width (and depth)—by extending the exposure threshold model developed by Jacobs [31, 41, 43, 77].

Generally speaking, these approaches have a number of limitations. The threshold cure model, for example, is a binary (uncured/cured) model which does not allow for nuance in the evolution of mechanical properties. On the other hand, the general approaches (which capture the layered nature of the AM process) are efficient in modeling at the entire part-scale, but are based on the assumption of a homogeneous effective shrinkage. As a consequence, these models are restricted to a certain (predefined) set of process parameters. Additionally, to efficiently capture the layered nature of the process, the finite element mesh is generated in advance, based on the target geometry. The predicted printed geometry is therefore merely a deformed version of the target geometry, whereas the process physics, e.g., illumination profile, light absorption and

scattering, can induce a significant deviation. Lastly, the models that account for detailed process physics are typically restricted to a few (two-dimensional) layers and only predict the (evolution of the) degree of conversion. There are no models available in literature that account for the presence of the powder filler on the thermo-chemo-mechanical response of the slurry.

On the basis of the state-of-the-art of modeling of ceramic VP described above, the following research questions (RQs) are addressed in this thesis:

RQ. I What are the relevant physics in the ceramic VP process and how can these be captured accurately and efficiently?

RQ. II How does the presence of the inclusions influence the VP process at the particle-length-scale?

RQ. III What is the effect of the geometry of the ceramic powder filler in the VP process?

RQ. IV How can the broad range of relevant length- and time-scales be simulated accurately and efficiently?

RQ. V How can the printed geometry, i.e. the solidified volume including its distortion/defects, be predicted qualitatively?

1.3 Outline of the thesis

In order to answer these RQs, this thesis is structured as sketched in Fig. 1.6. The multi-

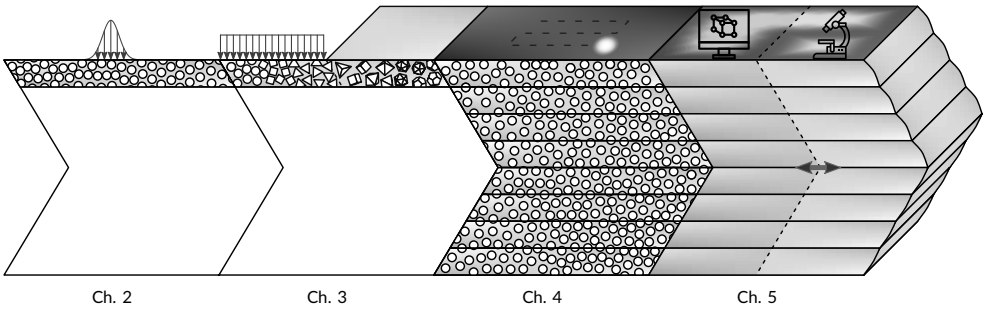

Figure 1.6 Graphical overview of the scope of individual thesis chapters.

physical description of the problem will first be addressed in Chapter 2. A Gaussian laser will serve as energy source into the two-dimensional model problem, of which the dimensions are smaller than a (typical) layer thickness. In Chapter 3, the step towards the actual three-dimensional setting is made. Through a parametric approach, the influence of the particle geometry on the photopolymerization reaction emanating as a result from a homogeneous irradiation is investigated. Furthermore, the predictive value

of two-dimensional analyses is evaluated for the three-dimensional physical problem. Chapter 4 translates the findings of Chapters 2 and 3 to a multi-layer three-dimensional laser scanning ceramic VP process. To capture the relevant effects efficiently, a multi-scale approach is applied which distinguishes between a microscopic, mesoscopic and macroscopic length-scale. The work in Chapters 2 to 4 captures the expected trends while providing interesting insights. Chapter 5 provides a first attempt to qualitatively validate the developed modeling framework. The predictive capability is assessed for an unfilled resin, printed using a bottom-up projection-based system, through geometrical comparison with experimentally obtained printed components. Finally, the thesis is concluded and remaining questions and challenges are highlighted in Chapter 6.

2

Multi-physical modeling of the photopolymerization process with a ceramic filler

Abstract

Additive manufacturing (AM) of ceramics through vat photopolymerization is a promising technique in which a ceramic filled photopolymer is selectively solidified in a layer-wise manner towards the final part geometry. Large scale adoption and optimization of AM for ceramics requires an in depth understanding of the process, which is pursued through a theoretical-numerical approach in this work.

A modeling framework is proposed that integrates the coupled effect of four relevant physical mechanisms: *(i)* light propagation through the heterogeneous matter; *(ii)* conversion of the photopolymer; *(iii)* thermal effects and *(iv)* evolution of mechanical properties upon solidification. Interestingly, the inclusion of ceramic particles (compared to the regular vat photopolymerization process) has a marked influence for each individual physical mechanism. Even though the individual key ingredients are established, the coupled and integrated framework provides innovative insights, demonstrating how difficult it is to achieve homogeneous polymerization for ceramic-filled resins.

Reproduced from: Westbeek, S., van Dommelen, J. A. W., Remmers, J. J. C. & Geers, M. G. D. Multiphysical modeling of the photopolymerization process for additive manufacturing of ceramics. *European Journal of Mechanics - A/Solids* **71,** 210–223 (Sept. 2018)

2.1 Introduction

The speed at which rapid prototyping evolved to additive manufacturing (AM), or 3D printing, illustrates how strongly its potential evolved in the past decade[19]. Many different AM technologies exist to fabricate ceramics [4]. The different techniques can be classified into seven distinct categories according to ASTM/ISO standardization [19]. The majority of the research has, however, focused on the development of porous structures. A twofold justification can be recognized for this [16]. On the one hand, the most logical motivation is that AM distinguishes itself from conventional production techniques by enabling of complex shapes with controllable porosity. On the other hand many of the available techniques are intrinsically suited for targeted shapes and detailed structures. For the particular additive manufacturing technique considered here, i.e. a patterned photopolymerization of individual layers (termed vat photopolymerization or stereolithography), these trends can also be recognized [31].

In order to produce ceramic parts through vat photopolymerization, additional processing steps are introduced, as illustrated in Fig. 1.3. Initially, ceramic powder is mixed into the photopolymeric solution to a high filling degree such that a viscous suspension, a slurry, is obtained. Based on a three-dimensional computer model of the desired geometry, the subsequent vat photopolymerization is a repetitive process of depositing a layer of slurry, selective illumination by UV light and lowering the building platform [54]. This AM technique ultimately results in the so-called green part, which can be considered as an intermediate composite part of ceramic inclusions in a polymer matrix. To retrieve the final dense ceramic, a subsequent pyrolysis and sintering step are required at different elevated temperatures, respectively to evaporate the polymer binder and sinter the dense monolithic part.

The addition of ceramic inclusions has a profound effect on the relevant physical processes in the stereolithography step. Starting already with the layer deposition, i.e. recoating, the higher viscosity needs to be considered since it increases the shear forces [16]. Upon illumination, the inclusions introduce significant light scattering, which is dominated by the difference in refractive index between the resin and the ceramic [31, 40–43]. As shown experimentally, the resulting cured polymer geometry can be considerably different from the expected geometry for unfilled liquids (as a function of the light source). Furthermore, the addition of solid particles reduces effective shrinkage, counter-acted by the polymerization shrinkage, which leads to increased stress concentrations.

Generally, the limiting factors in the wide adoption of AM in industry are reproducibility, productivity and scalability [57]. For ceramics in specific, the main challenges are: increasing the monolithic part density, increasing feasible product sizes and wall thickness and avoiding the formation of cracks [16]. A better understanding of the ceramics stereolithography process, in this case pursued through numerical modeling, is considered key in overcoming these problems [57].

Such a modeling approach should include the physical processes mentioned above.

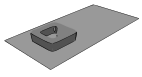

Different authors have used numerical modeling to improve the understanding of the stereolithography process, starting from Jacobs' cure depth model [54]. In subsequent works, a distinction can be made between attempts to capture the effect of the layered nature of the AM process [55, 63–65] or to incorporate more detailed physics affecting the polymerized profile as a function of the illumination source [66, 68–70, 79]. Whereas the first category of approaches is applicable for AM in general, the latter type of models is very specific for a certain AM technique. In comparison, for the modeling of laser powder bed or direct deposition processes the laser-material interaction induces sintering or melting directly by an increased temperature [80, 81].

The model presented in this chapter can be classified among the latter category, but, to the authors' knowledge, distinguishes itself in developing a framework that relates light penetration via conversion to the buildup of mechanical properties, with full account for the presence of the inclusions. At the same time, the effect of secondary physical phenomena such as generation of heat, chemical/thermal strain and the development of internal stresses can be accounted for. The theoretical formulation of this framework will be addressed first, after which dedicated verification steps of the implementation are conducted. The relevance of the developed model will be demonstrated using an academic example problem.

2.2 *Physical and mathematical framework*

The photopolymerization process of the filled resin is a complex multiphysical process. This section addresses the relevant physical ingredients of the modeling approach, followed by a description of the proposed multiphysical coupling.

2.2.1 *Illumination*

The first relevant phenomenon is the light scattering introduced upon illumination/irradiation of the slurry. Before addressing the particulate medium, the conventional vat photopolymerization modeling process for homogeneous media is reviewed.

Absorption In a homogeneous medium without the presence of scatterers, the attenuation of light is typically absorption dominated [82]. In that specific case, the absorbance $\mathfrak{a}$ is formulated through the Beer-Lambert law as [83]

$$\mathfrak{a} = -\log\left(\frac{I}{I_0}\right) = a[C^*]l, \tag{2.1}$$

where I_0 and I are the incident intensity and the intensity at depth l into the sample, respectively, a is the molar absorptivity and $[C^*]$ the concentration of the absorbing species. A relation providing the irradiance at a particular depth in the sample is obtained by rewriting Eq. (2.1) as [44, 84]

$$I(l) = I_0 e^{-\ln(10)a[C^*]l} = I_0 e^{-\alpha l} \quad [\mathrm{W/m^2}], \tag{2.2}$$

in which $\alpha = \ln(10)a[C^*]$ denotes the absorption/attenuation coefficient.

Within the field of vat photopolymerization, a modified version of Eq. (2.2) is often applied, which uses the so-called penetration depth D_p [54] as

$$D_p = \frac{1}{\ln(10)a[C^*]}. \tag{2.3}$$

Substituting the latter into Eq. (2.2) gives

$$I(l) = I_0 e^{-l/D_p}, \tag{2.4}$$

from which D_p can be interpreted as the depth where the irradiance has reduced to about 37 % (cf. $e^{-1} = 0.3679$) of the initial value [19, 54].

Wavelike behavior The impact of the inclusions on the vat photopolymerization process of ceramic filled resins has been clearly illustrated by e.g. Refs. [31, 40–43]. Experimental investigation shows that the ratio of cure depth to cure width decreases both for increasing the illumination intensity and for an increase in refractive index difference between the resin and the inclusions [31].

As already stated before, the Beer-Lambert law is no longer adequate if scattering is to be accounted for. Different theoretical and numerical methods exist to incorporate the effect of the ceramic inclusions. Due to the large filling fraction and the small difference between light wavelength and particle dimensions, both in the order of 1 µm, a wave description is required here [85, 86]. Phenomena such as interference and diffraction play an important role in this regime, where the ratio of the feature size to wavelength is smaller than ten. Refractive optics such as ray tracing are not able to capture these phenomena and should be applied only when the scattering object is over 100 times the size of the wavelength [85]. Additionally, the large filling fraction introduces so-called multiple scattering which prohibits the application of single-scattering approaches such as the theoretical Mie theory, which is only applicable for highly dilute suspensions [86, 87]. Within this work, the wave response is predicted by solving Maxwell's equations for electromagnetics using the finite element method (FEM) [88, 89].

In a finite element framework, the Maxwell equations (which are a function of both the magnetic and electric fields) are usually rewritten into a single formula. Constitutive relations are used to eliminate the dependence of the electric field on the magnetic field or vice versa [90–92]. In the former case, the equilibrium equation can be written as [93]

$$\vec{\nabla} \times \left(\frac{1}{\mu} \vec{\nabla} \times \vec{E} \right) + \varepsilon \frac{\partial^2 \vec{E}}{\partial t^2} + \gamma \frac{\partial \vec{E}}{\partial t} = -\frac{\partial \vec{J}^{\text{imp}}}{\partial t}, \tag{2.5}$$

where $\vec{E}$ is the electric field, μ the magnetic permeability, ε the electrical permittivity, γ the electric conductivity, $\vec{\nabla}\times$ the curl-operator and $\vec{J}^{\text{imp}}$ the imposed electrical current density and t denotes the time. By definition the total current density $\vec{J}$ is equal to

$\vec{J}^{\text{imp}} + \gamma\vec{E}$. When written in the frequency domain, under the assumption that the electric field takes the form $\vec{E}(\vec{x},t) = \Re\left(\vec{E}(\vec{x})e^{i\omega t}\right)$ [93, 94], the relation yields

$$\vec{\nabla}\times\left(\frac{1}{\mu}\vec{\nabla}\times\vec{E}\right) - \left(\omega^2\varepsilon - i\omega\gamma\right)\vec{E} = -i\omega\vec{J}^{\text{imp}}, \tag{2.6}$$

where ω is the angular frequency. The imposed current density will be assumed zero in the following. Furthermore, a separation of the material properties, i.e. μ, ε and γ into $\mu_0\mu_r$, $\varepsilon_0\varepsilon_r$ and $\gamma_0\gamma_r$, is introduced, where the property x, i.e. either μ, ε or γ, can be divided into a contribution in free space x_0 with appropriate units and a relative one x_r. Additionally, the light wave number ζ in free space is introduced as [94, 95]

$$\zeta_0 = \frac{\omega}{c_0} = \omega\sqrt{\mu_0\varepsilon_0} \tag{2.7}$$

with c_0 the speed of light in vacuum. This allows rewriting Eq. (2.6) as

$$\vec{\nabla}\times\left(\frac{1}{\mu_r}\vec{\nabla}\times\vec{E}\right) - \zeta_0^2\left(\varepsilon_r - \frac{i\gamma}{\varepsilon_0\omega}\right)\vec{E} = \vec{0}. \tag{2.8}$$

The latter is often simplified further using a complex form of the permittivity, e.g.

$$\tilde{\varepsilon_r} = \varepsilon_r - \frac{i\gamma}{\varepsilon_0\omega}. \tag{2.9}$$

Since ceramics and polymers are typically dielectric, the relative magnetic permeability μ_r is (very close to) unity [95]. Consequently, the complex relative permittivity can be written as

$$\tilde{\varepsilon_r} = (n - i\kappa)^2 \equiv \tilde{n}^2, \tag{2.10}$$

such that the inhomogeneous vector curl-curl equation becomes [95]

$$\vec{\nabla}\times\left(\vec{\nabla}\times\vec{E}\right) = \zeta_0^2\tilde{n}^2\vec{E}. \tag{2.11}$$

Note that the magnetic field can be (re-)obtained through the original Maxwell's equations, i.e. through Faraday's law as [90, 93, 95]

$$\vec{H} = -\frac{i}{\omega\mu}\vec{\nabla}\times\vec{E}, \tag{2.12}$$

where $\vec{H}$ is the magnetic field.

This notation is convenient in optics considering $n = \lambda_0/\lambda$ is the refractive index and κ is the extinction coefficient of the material. As the name suggests, κ captures a

similar phenomenon as the absorption coefficient α in Eq. (2.2), and they can be related through [95–97]

$$\kappa = \frac{\alpha c}{2\omega} = \frac{\alpha \lambda}{4\pi}. \tag{2.13}$$

The electric and magnetic fields are related to the local intensity through the Poynting vector

$$\vec{S} = \vec{E} \times \vec{H}^*, \tag{2.14}$$

where $\vec{H}^*$ denotes the complex conjugate of $\vec{H}$. The intensity then follows from the magnitude of the time averaged Poynting vector [94, 95, 98], i.e.

$$I = \|\langle \vec{S} \rangle\| = \left\| \frac{1}{2} \Re \left\{ \vec{E} \times \vec{H}^* \right\} \right\|. \tag{2.15}$$

In the limit case of a homogeneous (non-scattering) medium, Eq. (2.15) and Eq. (2.2) provide the same intensity field information. For heterogeneous media, Eq. (2.15) provides the near-field information required to describe the polymerization process.

2.2.2 *Polymerization*

The light energy flux propagating through the resin is a direct initiator for the polymerization reaction. In order to quantify polymerization, a degree of conversion is defined based on the current and initial monomer concentration [53] ($[M]$ and $[M]_0$, respectively) as

$$p = \frac{[M]_0 - [M]}{[M]_0}. \tag{2.16}$$

To relate the conversion to the intensity a rate type kinetic evolution equation will be used.

Cure kinetics The resins that are generally used in vat photopolymerization of ceramics are acrylate-based [31], which implies kinetics of the free-radical (chain) polymerization type [99]. A reaction of this type consists of three sequential steps, thus called a chain reaction, i.e. initiation, propagation and termination.

The initiation step begins with the creation of free radicals by the initiator molecule. The rate of radical generation is driven by the amount of light absorbed [44, 100]. A generally used expression for this is written in terms of the rate of initiation R_i as

$$R_i = 2\psi I_a, \tag{2.17}$$

where ψ is the quantum yield for initiation and I_a the absorbed light intensity [99]. The primary or initiator radical reacts with a monomer to form the chain-initiation species.

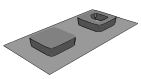

During propagation the initiated chains grow into long chains. At some point the propagation reaction arrests and termination occurs. This phenomenon mainly originates from two reactive species, combining into a non-reactive polymer. As a result from the propagation reaction, the monomer concentration decreases as the conversion progresses, which forms the motivation for Eq. (2.16).

Formally, the monomer evolution can be specified as

$$-\frac{d[M]}{dt} = R_i + R_p, \tag{2.18}$$

where R_p is the rate of propagation. The rate of monomer disappearance, which is identical to the rate of polymerization, is thus equal to the rate of propagation. In order to derive an equation for the monomer evolution, the rate of propagation is written as

$$R_p = k_p[M\bullet][M] \tag{2.19}$$

where k_p is the rate constant for propagation and $[M\bullet]$ is the concentration of chain radicals. Subsequently, a steady-state assumption is made on the concentration of radicals [53, 99, 100], i.e.

$$R_i = R_t = 2k_t[M\bullet]^2, \tag{2.20}$$

with k_t the rate constant for termination. Eq. (2.20) provides a relation for $[M\bullet]$ as a function of R_i, which, together with Eq. (2.17), can be substituted in Eq. (2.19) to obtain

$$R_p = -\frac{d[M]}{dt} = k_p[M]\left(\frac{\psi I_a}{k_t}\right)^{1/2}. \tag{2.21}$$

Such a formulation allows to account for temperature dependent effects through the kinetic parameters, by expressing them as an Arrhenius-type relationship [99]. Accounting for e.g. oxygen as an inhibitor species can also be done [70]. Furthermore, it is possible to account for photobleaching of the solution through a time-dependent (absorbed) intensity, which is caused by the depletion of the initiator [71–74]. Additionally, the polymerization may effect the refractive index of the polymer [101].

In the following, the cure kinetics are simplified further by lumping the different parameters in Eq. (2.21). The polymerization rate is then written as

$$R_p = -\frac{d[M]}{dt} = \mathcal{P}\sqrt{I}[M], \tag{2.22}$$

where $\mathcal{P}$ is the lumped polymerization constant, i.e. no time dependence is accounted for, and the absorbed intensity I_a is replaced by the actual intensity I. Note that the latter implies that the absorbed intensity I_a is assumed to be a constant fraction of the actual intensity I. Diffusional effects are not accounted for.

2.2.3 Thermodynamics

In a typical photo-polymeric suspension, heat generation is twofold. Firstly the photopolymerization reaction is exothermic, thus generating heat. Secondly, light absorption by the photoinitiator or its decomposition products, the dye, the monomer or polymer constitutes a thermal source. However, due to transparency for ultraviolet wavelengths, the absorption of most monomer and polymers is negligible in the considered regime.

The energy balance equation which incorporates these effects is adapted from [44] as

$$\rho c_p \frac{dT}{dt} = \nabla \cdot (k \nabla T) - \Delta H \frac{d[M]}{dt} + aI[C^*], \tag{2.23}$$

where the first two terms are the standard heat conduction terms, the third is the exothermic heat generation by the reaction and the last term accounts for heat generation by light absorption. The terms ρ, c_p and k in the first two terms correspond to the mass density, the heat capacity and the thermal conductivity, respectively. In the latter terms of Eq. (2.23), ΔH is the polymerization heat and a is the molar absorptivity. Under the assumption that the initiator is the only absorbing species, the latter $[C^*]$ can be replaced by $[In]$. It can also be noticed that the formulation in Eq. (2.23) does not contain direct heat sources and mechanical dissipation is neglected. Thermal equilibrium is also required in the formulation of the constitutive behavior for the inclusions, although be it without source terms. Consequently, the description for the inclusions is limited to the first two terms in Eq. (2.23). Note that a perfect interface between the two materials is assumed, i.e. the presence of voids or other irregularities is not accounted for.

2.2.4 Mechanics

In this work the mechanical response is linear elastic and restricted to small deformations. The total strain tensor ε is decomposed according to

$$\varepsilon = \varepsilon_e + \varepsilon_{ch} + \varepsilon_{th}, \tag{2.24}$$

into an elastic, chemical and thermal component, respectively. This is sufficient to illustrate the effect of the coupling between individual phenomena. Note that both matrix and inclusions undergo thermal strains, but ε_{ch} is limited to the resin. Explicitly accounting for the individual components' behavior through a full-field approach provides insights into e.g. the residual stress development.

Chemical shrinkage An effect that occurs upon conversion of monomer molecules into long polymer chains is the contraction of inter-molecular spacing. Specifically, the distance corresponding to the van der Waals interaction is replaced by a reduced intra-molecular covalent bond [52, 53]. The amount of volumetric shrinkage $\frac{\Delta V}{V}$ can

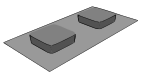

be estimated semi-analytically as a function of the conversion, through [102]

$$\frac{\Delta V}{V} = 22.5p\frac{\sum_i (f_i\chi_i)}{M_{mi}\chi_i}\rho, \tag{2.25}$$

where f_i, χ_i and M_{mi} are the monomer functionality, mole fraction and molecular mass, respectively, p is the degree of conversion which follows from Eq. (2.16) and ρ is the initial density of the monomer mixture. The factor 22.5 is the experimentally derived volume change per mole of the reacting group [55, 102, 103], which is here assumed to be an acrylate. The linear shrinkage strain can then be written as

$$\varepsilon_{\text{ch}} = \frac{1}{3}\frac{\Delta V}{V} I, \tag{2.26}$$

where isotropic shrinkage is assumed and, correspondingly, I is the unit tensor. In the following this is reformulated as

$$\varepsilon_{\text{ch}} = p\varepsilon_{\text{ch,max}} I, \tag{2.27}$$

with $\varepsilon_{\text{ch,max}}$ following from Eqs. (2.25) and (2.26) with $p = 1$. Whereas this assumes a linear and direct relationship between conversion and shrinkage, models where the shrinkage lags behind the conversion also exist [104], albeit that these models are often of a phenomenological nature. Note that the ceramic inclusions do not undergo a chemical transformation, i.e. the chemical shrinkage is restricted to the resin.

Thermal expansion The thermal strains are formulated according to the classical isotropic form

$$\varepsilon_{\text{th}} = \upsilon\,(T - T_{\text{ref}})\, I, \tag{2.28}$$

where υ is the thermal expansion coefficient of the material and T and T_{ref} the current and reference temperature, respectively. Thermal straining affects both the resin and the ceramic inclusions, each with its respective thermal expansion coefficient.

Solidification The build-up of mechanical properties in the matrix material is referred to as solidification, i.e. the elongation and cross-linking of polymer chains upon (photo)polymerization introducing solid-like behavior. Generally, the point where the material transforms from a liquid into a solid is termed the gel-point. From this point onward a direct relation between the conversion level and the elastic [54, 105], viscous [106–108] or even plastic properties [109] exists.

Transient phenomena will be ignored here, i.e. the solidification only consists in a conversion dependent Young's modulus. The relation between conversion and elasticity

is taken direct and linear from the gel-point p_{gel} onwards [107], where the stiffness up to the gel-point is assumed to be $e_0 E_{pol}$ with $e_0 \ll 1$. Mathematically this reads as

$$\begin{aligned} E(p) &= e_0 E_{pol} && \text{for } p < p_{gel} \\ E(p) &= \left(\frac{1 - e_0}{1 - p_{gel}} \left(p - p_{gel} \right) + e_0 \right) E_{pol} && \text{for } p \geq p_{gel} \end{aligned} \tag{2.29}$$

where $E(p)$ is the conversion dependent Young's modulus of the monomer/polymer. The resin and inclusion's stress tensors σ are related to the elastic strain tensors ε through the classical isotropic Hooke's law. Other mechanistic properties, such as the coefficient of thermal expansion, are taken constant, i.e. independent of the conversion, for simplicity.

2.2.5 *Coupling of physical phenomena*

The complete coupling between all phenomena introduced in the previous Sections 2.2.1 to 2.2.4 is illustrated in Fig. 2.1. A key assumption in the formulation of the multiphysical framework is the separation of time scales by separating between the frequency and time domain. This is justified by the large difference in time scales of the light propagation and the kinetics. For a vector scanning technique, as considered here, the transit time of a photon through a layer is in the order of a picosecond (~10^{-12} s), whereas the kinetic reaction duration is typically of the order of (several) microseconds (~10^{-6} s) [19, 54]. It is expected that the other physical phenomena are coupled to the reaction time.

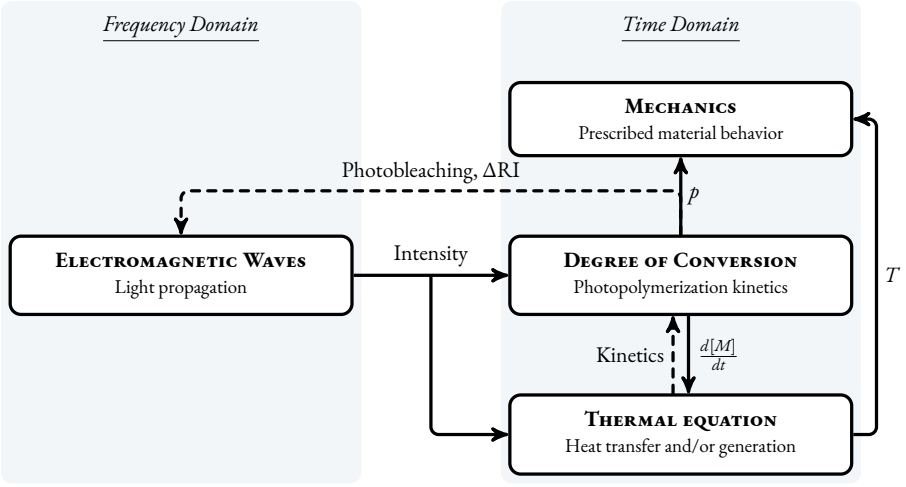

Figure 2.1 Overview of the proposed multiphysical coupling. Dashed lines have been mentioned in Section 2.2 but are currently not incorporated in the modeling framework.

From a numerical point of view, this implies that a steady-state response is obtained for the light propagation in the harmonic frequency domain, corresponding to the light source conditions. Subsequently, Eq. (2.15) is used to extract the effective time average intensity field, which provides the required input for the time-domain simulation of the chemical conversion (and absorption heat) and the emanating phenomena indicated in Fig. 2.1.

2.2.6 *Implementational aspects*

Solving Maxwell's equations in a finite element framework imposes additional requirements on the discretization. In order to properly resolve the wavelike behavior, a minimal number of 10 elements is required over the wavelength [94], whereas the actual wavelength inside the different constituents is typically reduced by a refractive index > 1, according to $\lambda = \lambda_0/n$. This clearly poses a restriction on the feasibility of solving large structures, considering the wavelength of the applied UV light is only approximately 400 nm. Restricting the simulation to a finite domain requires special absorbing boundary conditions to prevent scattering from the bounding frame. This requirement is incorporated in the form of a so-called perfectly matched layer (PML) [110]. Furthermore, in order to prevent spurious solutions in inhomogeneous media, a special type of elements is used with degrees of freedom assigned to the edges instead of the nodes, referred to as edge elements. The requirement for these vector or Nédélec elements originates from the lack of enforcement of the Maxwell divergence condition by regular nodal elements, which has been described in detail in Refs. [90, 91, 111, 112]. The complete modeling framework as depicted in Fig. 2.1 is implemented in the finite element package Comsol 5.0 [113]. A fully-coupled approach is used, employing a direct solver. The backward Euler time stepping is automated through a variable-order variable-step-size backward differentiation algorithm [113]. No special measures were required to ensure stability.

2.3 *Verification*

Before investigating the different physical phenomena in the example problem considered in Section 2.4, the correctness of the numerical framework is assessed first. To do so, the different components of the modeling framework are compared to analytic solutions using identical parameter-sets in the following.

2.3.1 *Intensity*

An important component of the proposed model (cf. Fig. 2.1) is the electromagnetic wave description, particularly the near-field information predicted for the intensity field. It remains to be verified whether the numerical implementation of the Maxwell's equations correctly approximates the expected scattering. To this purpose, the predicted result for a single scattering particle is compared to the analytic near-field Mie theory

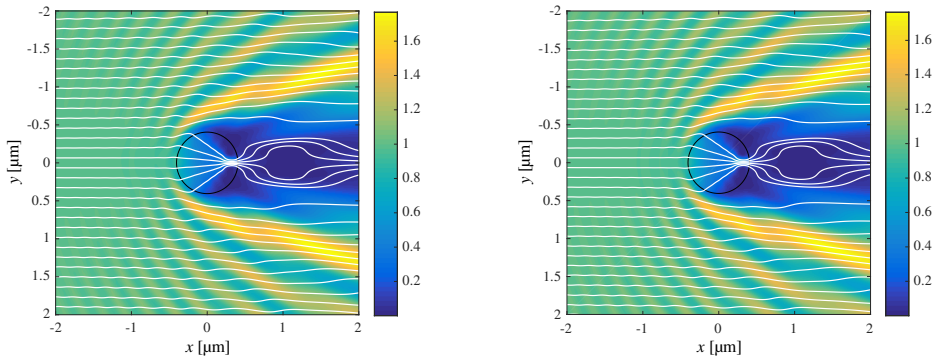

(a) Computed normalized intensity profile

(b) Normalized intensity profile obtained using MatScat [114]

Figure 2.2 Comparison of results for the field intensity obtained from the present framework and MatScat for a particle with $r = \lambda$, $\tilde{\varepsilon}_r = 4 - 0.5i$. Intensity is normalized by the source intensity. Streamlines of the Poynting vector are depicted in white.

implementation by Schäfer et al. [114]. An example result is shown in Fig. 2.2. Here the matrix material and the particle have a (complex) relative permittivity of $\tilde{\varepsilon}_r = 1$ and $\tilde{\varepsilon}_r = 4 - 0.5i$, respectively. In the current example, absorption by the polymer is neglected. The input source is a homogeneous plane wave propagating towards the right with a polarization in the direction perpendicular to the xy-plane, i.e. the out-of-plane z-direction. Note that in the case of a polymer matrix, this material would also absorb light, i.e. have a complex component in the permittivity, but the implemented Mie theory does not allow for this. The radius of the particle is equal to the wavelength $\lambda = 400$ nm. In order to visualize the results in Fig. 2.2a, the field data obtained with the implemented numerical framework was interpolated using natural neighbor interpolation.

The depicted intensity profile and power flow lines in Fig. 2.2 clearly reveal that the wavelike behavior, e.g. not only refraction and attenuation but also diffraction, is correctly captured. The mean difference in the depicted field (also accounting for interpolation errors) is only 1%. Fig. 2.2 also emphasizes the relevance of a wave description for these length scales.

2.3.2 *Conversion*

The polymerization model is implemented through the Comsol PDE interface [113]. In order to verify this part of the implementation, a domain is polymerized by a constant and homogeneous intensity field I_0. This allows for an analytical solution for $d[M]/dt$ derived from Eq. (2.22) as

$$\frac{d[M]}{dt} = -[M]_0 \mathcal{P} \sqrt{I_0}\, e^{-\mathcal{P}\sqrt{I_0}\, t}. \tag{2.30}$$

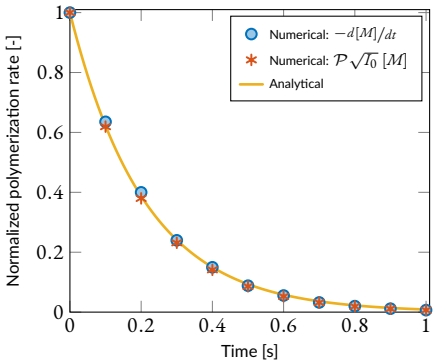

Figure 2.3 Comparison of the numerical derived $d[M]/dt$ with the right hand side of Eq. (2.22) and the analytic form resulting from constant intensity illumination of I_0. Values are normalized by $\frac{d[M]}{dt}(t=0)$ from Eq. (2.30).

Due to the homogeneous intensity, the considered domain can be from one to three-dimensional. Eq. (2.30) is then compared to the evolution of the numerically derived $\mathcal{P}\sqrt{I_0}[M]$. Parameter values as specified in Tables 2.1 and 2.3, with $I_0 = I_{\max}$ are used. Furthermore, because $\mathrm{d}[M]/\mathrm{d}t$ enters the thermal balance in Eq. (2.23), the numerical time derivation is also included in the comparison. The solution for a two-dimensional domain of $1 \times 1\ \mu\mathrm{m}^2$ is shown in Fig. 2.3. Small deviations from the analytic result are observed in Fig. 2.3, particularly where the slope is the highest, but overall the correspondence is adequate.

2.3.3 *Temperature*

A similar approach compared to the previous conversion verification in Section 2.3.2 with a homogeneous illumination is also used in the thermal verification assuming thermally insulated boundaries. The result of this comparison is shown in Fig. 2.4 for a homogeneous $1 \times 1\ \mu\mathrm{m}^2$ domain where the analytical (combined) prediction is derived from Eq. (2.23) as

$$T = T_0 + \frac{1}{\rho c_p}\left(\underbrace{\Delta H[M]_0\left(\exp\left(-t\mathcal{P}\sqrt{I_0}\right)-1\right)}_{\text{chemical}} + \underbrace{aI_0[In]_0 t}_{\text{absorption}}\right) \tag{2.31}$$

Parameter values are again adopted from Tables 2.1 and 2.3 with $I_0 = I_{\max}$. For the depicted absorption contribution to the temperature profile, the chemical component is set to zero and vice versa. The large temperature increase seen in Fig. 2.4 results from the material parameters and can also be seen in Ref. [44]. It is clear that the contribution of heat from absorption is less significant compared to the exothermic heat for the considered light intensity. Again, Fig. 2.4 shows adequate correspondence of the numerical results compared to the analytic prediction.

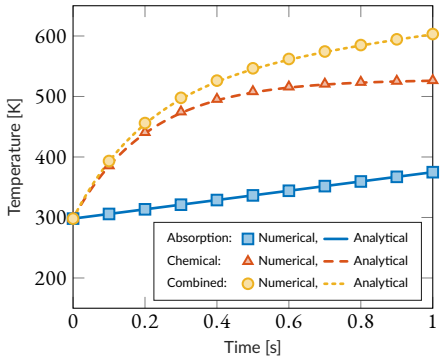

Figure 2.4 Comparison of the numerically obtained temperature increase with the analytical solution in terms of the absorption, exothermic and combined heat.

2.3.4 Stress

Upon solidification, the polymer resin generally shrinks, as clarified in Section 2.2.4. At the same time, due to the exothermic nature of the reaction, thermal expansion occurs. As these strains, together with the conversion dependent mechanical properties, induce a stress build-up in the photopolymerization process, it is key to account for the combined effect correctly. This is illustrated in Fig. 2.5 for the same homogeneous $1 \times 1\ \mu m^2$ domain. The square domain's lower left corner is fixed, while the bottom edge is only constrained in the vertical direction. The left, right and upper edge are unconstrained. Fig. 2.5 depicts the stresses predicted numerically in a constrained, i.e. plane strain z-direction and compares them to the analytical result. The analytical stress components

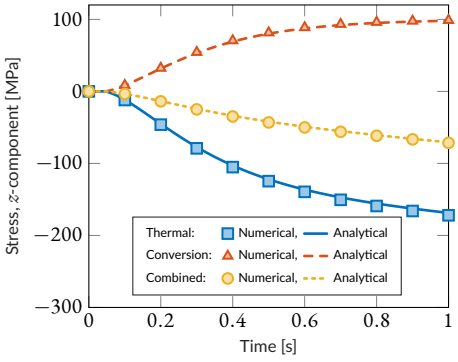

Figure 2.5 Comparison of the numerically obtained stress with the analytical response in the constrained (plane strain) z-direction, for the thermal, chemical and combined components. The difference is the propagated error from the polymerization and thermal prediction.

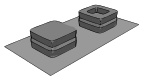

in the constrained direction can be obtained as

$$\sigma_{z,\mathrm{ch}} = -\varepsilon_{\mathrm{ch,max}} p E \tag{2.32}$$

and

$$\sigma_{z,\mathrm{th}} = -\upsilon \left(T - T_{\mathrm{ref}}\right) E, \tag{2.33}$$

where $E = E(p)$ through Eq. (2.29) and $T = T(p)$ through Eq. (2.31). The initial zero slope of the lines depicted in Fig. 2.5 at $t = 0$ s illustrates the effect of the gel-point. Note that the numerical prediction uses the previously discussed addressed numerical values as input. The difference between the numerical and analytical value is therefore the error that propagated through the polymerization and thermal model, starting from the homogeneous intensity.

2.4 Application to an example problem

The goal of the example problem is to demonstrate the potential of the described approach and to illustrate the influence of the ceramic inclusions in the photopolymerization process. The necessary model input will be addressed in Section 2.4.2, after which Section 2.4.3 discusses the results.

2.4.1 Problem description

In order to illustrate the effect of the ceramic inclusions, three distinct geometries are considered, which are depicted in Figs. 2.6a to 2.6c: *(1)* an unfilled resin (Fig. 2.6a); *(2)* a slurry with an inclusion filling fraction φ of 0.4 distributed in a hexagonal grid (Fig. 2.6b); *(3)* a random distribution of particles with $\varphi = 0.4$ (Fig. 2.6c). The size of the considered square domains is $11 \times 11\ \mu\mathrm{m}^2$, whereas the particles have a uniform diameter of 1 µm. The only difference between the different configurations is the distribution of the ceramic inclusions, i.e. the properties and boundary/initial conditions are identical. This allows to study the relevance of the particulate inclusions and the randomness in their distribution. In the following, the unfilled resin, the matrix with particles positioned in a hexagonal grid and the arbitrarily distributed geometry will be referred to as case *A*, *B* and *C*, respectively.

Fig. 2.7 indicates the boundary conditions for the different physical models. The boundary conditions for the electromagnetic simulation are depicted in Fig. 2.7a. The top surface acts as a port for the incoming light intensity, which shows a Gaussian (laser) profile with a maximum intensity I_{max} at $x = 0$. The profile's spatial dependence is formulated as

$$I_{\mathrm{port}} = I_{\mathrm{max}} e^{-x^2/w_0^2}, \tag{2.34}$$

where w_0 is the beam half width where the intensity drops to $1/e^2$ of the value on the beam axis. The wave propagates in the negative y-direction with a polarization in the

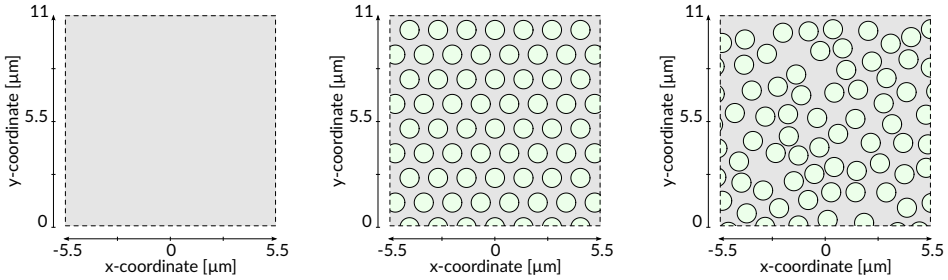

(a) Unfilled resin: *A* **(b)** Hexagonal grid: *B* **(c)** Random distribution: *C*

Figure 2.6 Example problem geometries with $\varphi = 0$ in (a) and $\varphi = 0.4$ in (b) and (c).

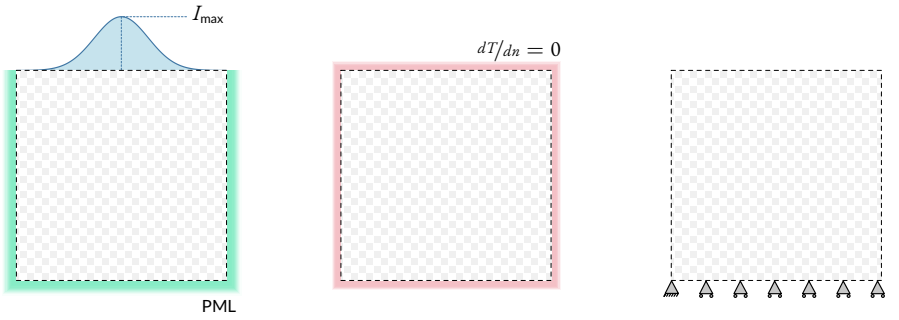

(a) Electromagnetic **(b)** Thermal **(c)** Mechanical

Figure 2.7 Light (a), thermal (b) and mechanical (c) boundary conditions for the example problems introduced in Fig. 2.6. The polymerization reaction (not depicted) is limited to the resin and no flux occurs across the boundaries.

direction perpendicular to the *xy*-plane. Additionally, a Gaussian pulse is introduced, entailing an explicit time dependence, such that Eq. (2.34) can be extended to

$$I_{\text{port}} = I_{\max} e^{-x^2/w_0^2} \, e^{-(t-t_{\max})^2/2\tau^2} \tag{2.35}$$

where $t_{\max}$ is the time where the peak intensity occurs, and τ is a characteristic for the width temporal of the Gaussian "bell" shape. In order to simulate a finite domain and to prevent spurious reflections from the domain boundaries, absorbing boundary conditions are enforced at the bottom and left/right edges, in the form of a perfectly matched layer (PML) [94, 110]. Note a PML essentially extends the computational domain. Actual time steps taken by the backward differentiation time-stepping algorithm do not exceed 0.01 s, allowing to completely resolve the pulsed light excitation and the emanating physics.

The polymerization reaction, as introduced in Section 2.2.2, only actively influences the resin domain. No flux conditions are enforced on the outer boundaries and along the interfaces with the inclusions.

Fig. 2.7b illustrates the thermally insulated conditions assumed for the heat balance Eq. (2.23), i.e. $^{dT}/_{dn} = 0$. The result from these conditions is that the generated heat is internally contained and the thermal effect of the included particles is easily deduced.

Finally, the mechanical boundary conditions are illustrated in Fig. 2.7c. The left bottom point is constrained in all directions, whereas for the remainder of the bottom edge the vertical displacement is suppressed. The left, right and top edges are not constrained. A plane stress assumption is made in the two-dimensional representation. These particular choices prevent the buildup of macroscopic (average) stresses. Consequently, the buildup of microscopic stress around the rigid-like inclusions can be easily identified.

2.4.2 *Model parameters*

In order to illustrate the capabilities of the proposed model, a representative set of parameters is introduced. The material parameters are provided in Tables 2.1 and 2.2 for the resin and ceramic inclusions, respectively.

The first section in Tables 2.1 and 2.2 provides the required material input with respect to the electromagnetic modeling. Alumina particles are chosen as they provide a relatively large contrast in refractive index compared to the resin, cf. 1.78 to 1.5. Whereas the refractive index of alumina is a well-established value [101], the value for the resin is only approximate considering the broad range in monomer refractive indices and its increase during polymerization [28, 101]. The ceramic inclusions are assumed to be transparent for UV-light [31]. Consequently, only the resin's extinction coefficient is

Table 2.1: Material properties for the resin.

Parameter	Value	Unit	Description	Source
n	1.5	[-]	Refractive index	[28, 101]
$[In]_0$	5	[mol/L]	Initial initiator concentration	
a_{In}	150	[L/(mol cm)]	Molar absorptivity initiator	[44]
$[M]_0$	8.2	[mol/L]	Initial monomer concentration	[44]
$\mathcal{P}$	0.15	$[\mathrm{m}/(\mathrm{sW}^{\frac{1}{2}})]$	Polymerization rate constant	[115]
c_p	1700	[J/(kg K)]	Heat capacity	[113]
ρ	1150	[kg/m^3]	Density	[113]
k	0.26	[W/(m K)]	Thermal conductivity	[113]
ΔH	$5.48 \cdot 10^4$	[J/mol]	Polymerization heat	[44]
E_{pol}	$2 \cdot 10^9$	[Pa]	Young's modulus at $p = 1$	[113]
e_0	$1 \cdot 10^{-3}$	[-]	Initial multiplication factor E_{pol}	
p_{gel}	0.2	[-]	Gel-point for conversion	[31]
ν	0.4	[-]	Poisson's ratio	[113]
$\varepsilon_{\mathrm{ch,max}}$	-0.05	[-]	Maximum shrinkage strain	[55]
υ	$280 \cdot 10^{-6}$	[1/K]	Coeff. of thermal expansion	[113]

Table 2.2: Material properties for the alumina inclusions.

Parameter	Value	Unit	Description	Source
n	1.78	[-]	Refractive index	[101]
κ	0	[-]	Extinction coefficient	[31]
c_p	900	[J/(kg K)]	Heat capacity	[113]
ρ	3900	[kg/m^3]	Density	[113]
k	27	[W/(m K)]	Thermal conductivity	[113]
E	$300 \cdot 10^9$	[Pa]	Young's modulus	[113]
ν	0.222	[-]	Poisson's ratio	[113]
υ	$8 \cdot 10^{-6}$	[1/K]	Coeff. of thermal expansion	[113]

nonzero, and obtained through Eq. (2.13) using $\alpha = \ln(10) a_{In} [In]$ (cf. Section 2.2.1). The (initial) initiator magnitude $[In]_0$ is increased with respect to Ref. [44] to enhance the effect of absorption in the considered domain. As a consequence the light extinction increases, but the path the light traverses remains the same.

For the polymerization prediction, the initial monomer concentration and the polymerization rate constant suffice. The initial monomer concentration is adopted from Ref. [44]. The magnitude of the polymerization rate constant is motivated by fitting of Eq. (2.22) to Fig. 6 from Ref. [115] whilst accounting for the intensity dependence.

Thermal properties such as heat capacity and thermal conductivity for both the alumina particles and the representative polymer (i.e. nylon was chosen in this case) follow from Ref. [113]. The polymerization heat is adopted from Ref. [44].

The Young's modulus (fully polymerized for the resin), the Poisson's ratio and thermal expansion values (assumed constant) follow from Ref. [113]. The initially small value of the modulus of the monomer is obtained by pre-multiplication of the fully polymerized Young's modulus with a value $e_0 = 1 \cdot 10^{-3}$. A representative linear chemical shrinkage strain active in the resin upon polymerization is chosen as 5% [55].

Initial and boundary conditions are specified in Table 2.3. Firstly, $I_{\max}$ and w_0 define the shape of the incoming light source at $t = t_{\max}$, whereas secondly, τ dictates the time

Table 2.3: Initial and boundary conditions.

Parameter	Value	Unit	Description
$I_{\max}$	1000	[W/m^2]	Incident peak light intensity
w_0	2	[µm]	$1/e^2$ half-width of Gaussian beam
$t_{\max}$	0.5	[s]	Time of peak intensity
τ	$0.4/3$	[s]	Pulse temporal standard deviation
λ	400	[nm]	Wavelength, vacuum
T_0	293	[K]	Initial temperature

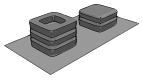

dependence of the input wave and, thirdly, λ is the wavelength. The initial temperature is set to 20 °C. Using the specified ultraviolet wavelength λ and the resin's and inclusion's refractive index n from Tables 2.1 and 2.2, the coupled multi-physical example problems incorporate $\mathcal{O}(10 \text{ million})$ degrees of freedom.

2.4.3 *Results and discussion*

One of the key phenomena incorporated in the modeling framework is the propagation of the laser light through the matter. The intensity from the light is also the initiator for the onset of polymerization and consequently the generation of heat and the build-up of mechanical resistance and stresses. In this case, the predicted light intensity is a function of the electric field. The maximum electric wave amplitude which occurs at $t = t_{\max} = 0.5$ s for the adopted polarization is depicted in Fig. 2.8. The result is shown at maximum illumination, because of the linearity in the Maxwell's equations, i.e. the wave magnitude throughout the domain scales linearly with the source magnitude. Fig. 2.8 illustrates the effect of the difference in refractive index on the wave propagation through and around inclusions for cases *B* and *C*, introducing effects such as interference and diffraction. For case *A*, the result of the planar wave (which remains planar) shows a Gaussian distribution in magnitude over the width and the effect of extinction at increasing penetration depth. The same distribution can also be perceived in the intensity profile depicted in Fig. 2.9. Besides the intensity, which is normalized by the maximum intensity at the input port $I_{\max}$, this figure also shows the streamlines of the power flow, i.e. the direction of the Poynting vector from Eq. (2.14). Here, the wavelike pattern has vanished but the interference and diffractional effects are more pronounced. Whereas case *A* illustrates the expected intensity profile from the Beer-Lambert law, cases *B* and *C* show a highly irregular light propagation. In addition to the inhomogeneous nature of the intensity, also large intensifications occur as a result from interference. From both the flow streamlines and the intensity concentrations, it is clear that the light still predominantly propagates towards the bottom of the specimen in case *B*. Nevertheless, a more severe scattering occurs in case *C*, where the inclusions are randomly distributed.

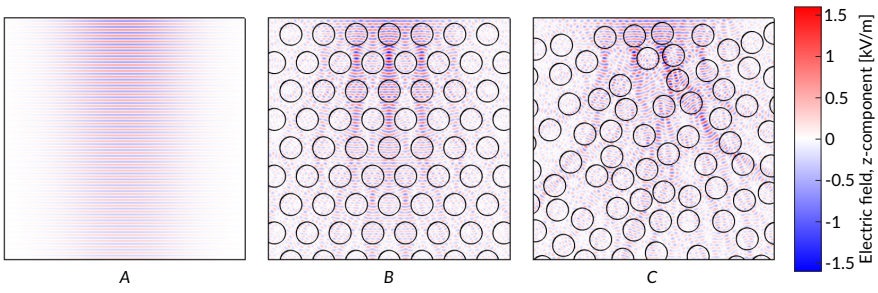

Figure 2.8 Electric field in the z-direction in the different geometries at $t = t_{\max} = 0.5$ s.

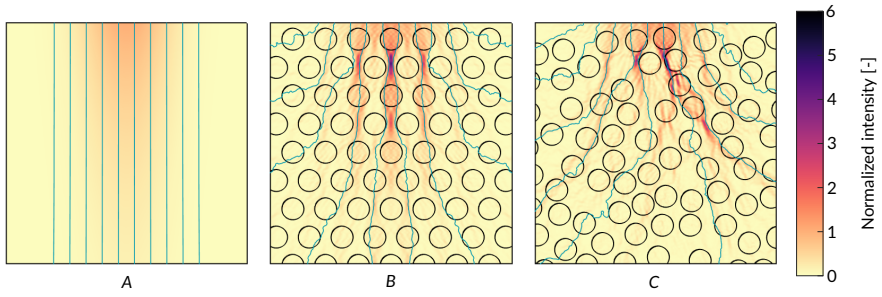

Figure 2.9 Intensity normalized with I_{max} and flow direction, i.e. direction of the Poynting vector, in the three geometries at $t = t_{max} = 0.5$ s.

The latter trend also pushes through to the polymerization reaction as shown in Fig. 2.10. It shows the time dependent polymerization at $t = 0.2, 0.5$ and 1 s. These times are taken before, at and after the peak in illumination, respectively. Unlike case *A*, the cases with particles have a highly inhomogeneous conversion level after the pulsed illumination (at $t = 1$ s). This effect will reduce with a moving laser and/or by accounting for a more irregular geometry of the inclusions. Nonetheless, it clearly illustrates the challenge to obtain a homogeneously polymerized product. This is an essential quality requirement, since the presence of residual monomer has been identified in relation to the formation of cracks during post-processing of the green part [51]. The average, minimum and maximum degree of conversion value obtained for the three different cases as a function of time are depicted in Fig. 2.11. As depicted, the average degree of conversion is higher for cases *B* and *C* with a value of $p_{mean} = 0.47$ and 0.45, respectively, compared to $p_{mean} = 0.41$ for case *A*. Note that this does not necessarily imply that one case is better than the other. The polymerization efficiency as reported here is dependent on the choice of domain dimensions, e.g. case *A* will be more efficient for a domain with a higher depth-to-width ratio. Fig. 2.11 does, however, further emphasize the pronounced inhomogeneity in the filled resin, considering the larger band between the minimum and the maximum value.

A direct result from the illumination and the polymerization is the accumulation of heat. Due to the small dimensions and the considered boundary conditions, the temperature remains essentially homogeneous throughout the simulated domain, i.e. the temperature difference is only in the order of 10^{-2} K. At $t = 1$ s, the maximum temperature obtained in cases *A*, *B* and *C* is 388, 344 and 342 K, respectively. The most important conclusion is that the temperature increase is more significant in the unfilled resin. The explanation for this is twofold; firstly, the inclusions do not contribute to the reaction heat and, secondly, they act as a heat sink. The minor difference between case *B* and *C* results from the contrast in the average degree of conversion at $t = 1$ s, as shown in Fig. 2.11.

Finally, the polymerization results in residual stresses. In the solidification process a number of interesting effects accumulate. First, the conversion induces a chemical

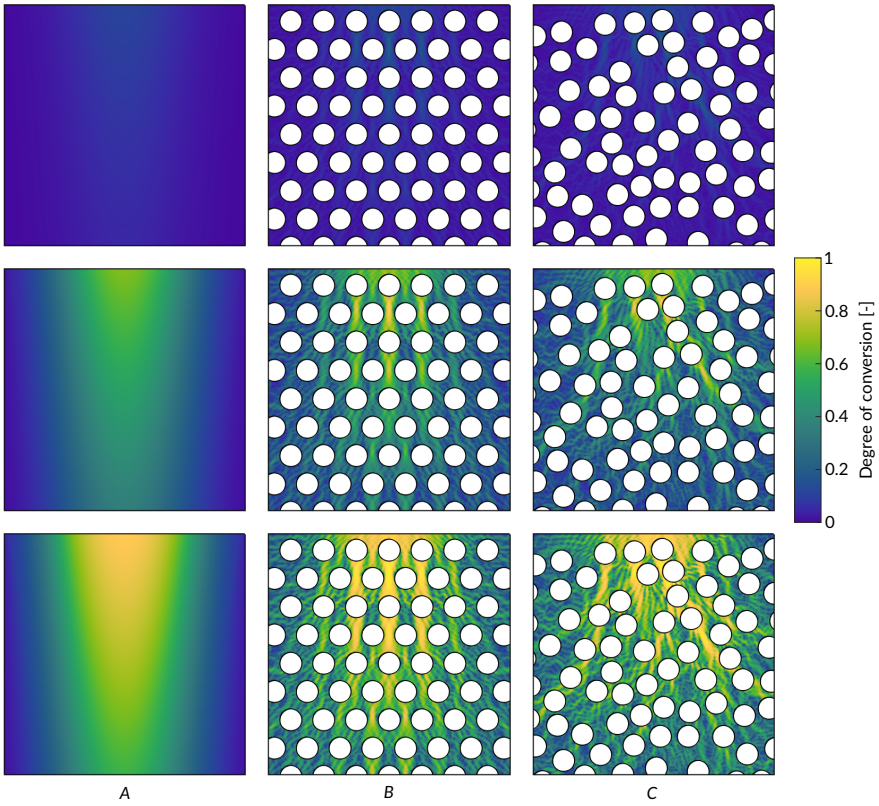

Figure 2.10 Degree of conversion p in the different geometries at $t = 0.2, 0.5$ and 1 s.

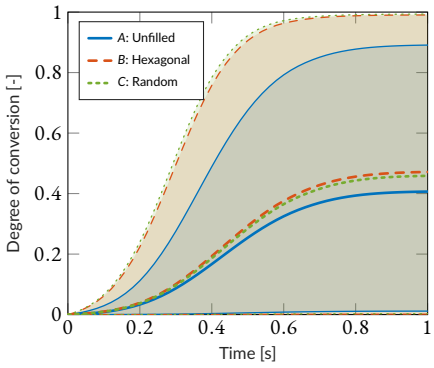

Figure 2.11 Evolution of the degree of conversion p for the different geometries with its mean value indicated by a thick line and the upper and lower bounds with a thin line.

shrinkage in the resin following Eq. (2.27). Additionally, the polymerization reaction induced heat results in thermal expansion according to Eq. (2.28). The effect of the conversion is the build-up of stiffness, which is assumed linear after the gel-point as according to Eq. (2.29). Fig. 2.12 depicts the combined effect of these phenomena. The deformations, constituted by the simultaneous polymer chemical shrinkage and the composite's thermal expansion, illustrate the effect of the rigid-like ceramic inclusions. More severe warpage occurs in case *A* compared to cases *B* and *C*. Additionally, case *A* is the only geometry that effectively exhibits a volumetric expansion due to a higher temperature increase and effective thermal expansion coefficient. As larger deformations usually entail stress relaxation, the development of residual stresses is much smaller in case *A* compared to cases *B* and *C*. In order to highlight the stress concentrations, the color range is limited from $[0-60]$ MPa in Fig. 2.12, however, the peak stresses for case *A*, *B* and *C* at $t = 1$ s are 14, 76 and 128 MPa, respectively. The higher stress concentration in case *C* primarily originates from the more inhomogeneous particle distribution, compared to the hexagonal one. Juxtaposing Figs. 2.10 and 2.12 demonstrates the effect of introducing the gel-point in the solidification, i.e. it acts as a threshold for the development of stress. Overall, the stressed region in cases *A* and *B* is fairly narrow and deep, whereas case *C* illustrates a wider region of stress evolution. This is consistent with the more homogeneous contour of the deformed geometry.

The response of the example problems after cooling down to $T = T_0$ is shown in Fig. 2.13, using the same color bar as Fig. 2.12 to emphasize the difference. Elimination of thermal expansion induces an increased stress for cases *B* and *C*, with peak stresses of 106 and 234 MPa, respectively. Due to the homogeneous thermal expansion, the peak stress remains 14 MPa in case *A*. With respect to the resulting deformations, the most notable difference occurs in case *A*, where the effective behavior is no longer a volumetric expansion. Due to the lower thermal expansion coefficient of the inclusions, the difference is less severe for the filled cases. Consequently, in case *A* the distortion reduces after cooling down, whereas for cases *B* and *C* it is less affected.

The presented example problem illustrates the significant effect of the addition of the inclusions on the propagation of light, the conversion reaction, the accumulation of heat and the solidification process. The expected curing pattern occurring in the homogeneous case *A* becomes severely distorted when randomly distributed inclusions are incorporated as in case *C*. In the present analysis the randomness is limited to the particle distribution only. The addition of more irregularities, such as particle size and shape, will have a supplementary effect on the dispersion of light through the matter. Additionally, the filling fraction of 40 % can be considered low with respect to ideal conditions for the post-processing of the green part. A higher filling fraction further increases the light dispersion. Cases *B* and *C* clearly highlight the relevance of the proposed approach to the model the coupled physical phenomena.

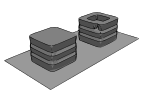

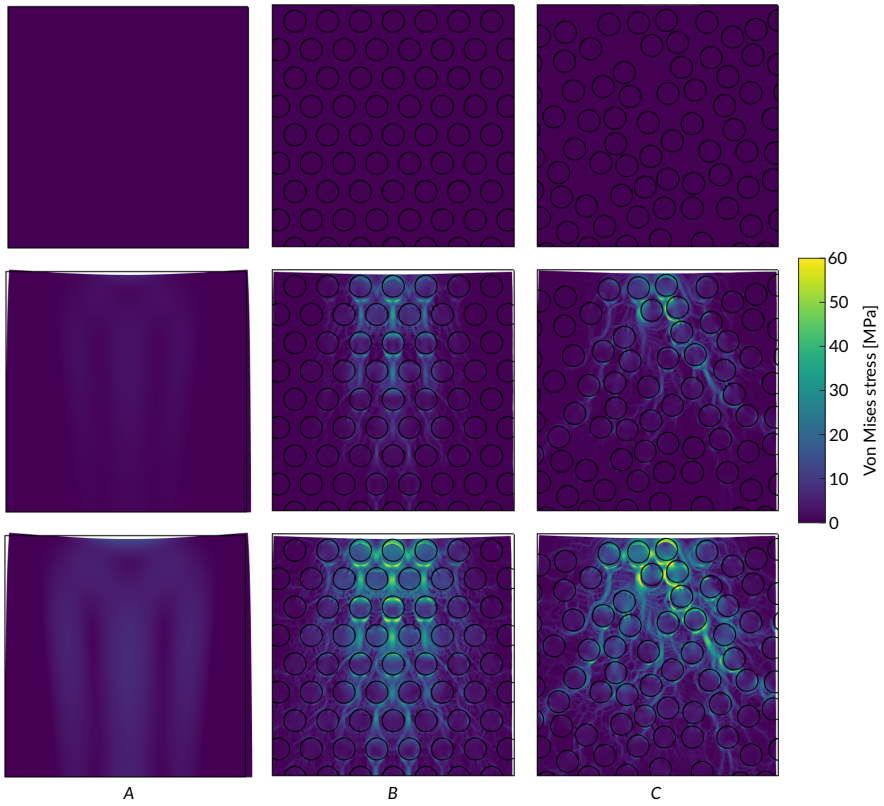

Figure 2.12 Von Mises stress and deformation in the different geometries at $t = 0.2, 0.5$ and 1 s. Solid lines depict the initial geometry. Deformations are scaled by a factor of 2. The peak stresses at $t = 1$ s are 14 MPa, 76 MPa and 128 MPa for cases *A*, *B* and *C*, respectively.

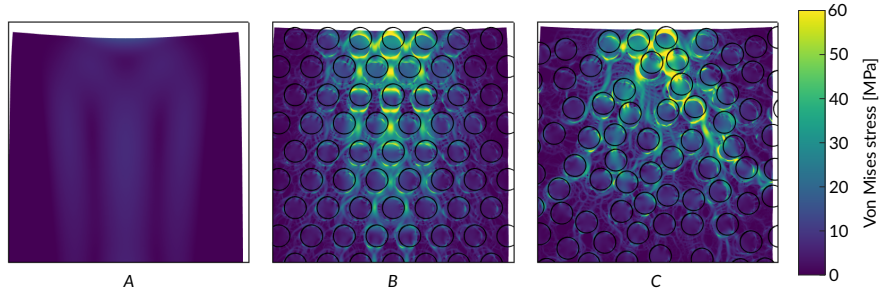

Figure 2.13 Von Mises stress and deformation in the different geometries after illumination and cooling down to $T = T_0$. Solid lines depict the initial geometry. Deformations are scaled by a factor of 2. The peak stresses are now 14 MPa, 106 MPa and 234 MPa for cases *A*, *B* and *C*, respectively. Color bar is adopted from Fig. 2.12.

2.5 Conclusions

This chapter proposes a coupled solution framework capturing distinct physical phenomena occurring in the vat photopolymerization process for ceramics. The numerical framework provides a direct coupling between a light source, via polymerization kinetics and temperature evolution, to the build-up of mechanical properties and residual stresses, resolved in space and time.

Accounting for the wavelike behavior of light illustrates the pronounced effects emerging when the size of microstructural features, i.e. the size of the particles, is of the same order as the wavelength, which is typical in AM for ceramics. The current polymerization model is relatively simple, only accounting for the dependence on monomer concentration and light intensity. Yet, it already highlights the impact of the resulting inhomogeneous intensity on the solidification. The absorption of light combined with the exothermic polymerization causes the slurry to heat up. Due to the adopted thermally insulated boundary conditions, the final temperature is an upper bound, where the inclusions again have an influence. The accompanying thermal expansion is countered by a chemical shrinkage as polymerization progresses. This is illustrated in the proposed example problem, where a more homogeneous conversion results in a more homogeneous shrinkage. At the same time, the presence of rigid inclusions increases the magnitude of residual stresses. These trends remain after cooling down to the initial temperature, where the confined chemical shrinkage causes an increased residual stress state.

The model provides novel insights in the coupling between different physical phenomena in the photopolymerization process. The original and innovative contribution of this chapter is a direct coupling between light scattering effects and photopolymerization related phenomena on a micro scale for a particulate medium. Whereas the framework can also be used for cure modeling in homogeneous resins, its real added value becomes clear in the presence of scattering particles with a size in the order of the wavelength. Although the considered model problems are two-dimensional, the developed modeling framework can also be devoted to three-dimensional cases. Future work will investigate to what extent the identified trends translate to three dimensions. It is expected that many of the model ingredients with respect to the distinct physical phenomena can be easily tailored to specific (slurry) systems of interest.

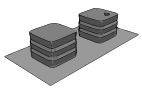

3

Influence of particle shape on the irradiation step and the resulting photopolymerization

Abstract

Additive manufacturing (AM) of ceramics through a vat photopolymerization (VP) process is a promising technique due to the high intrinsic resolution and the evanescence of stresses introduced during the layerwise additive manufacturing process. Compared to the regular vat photopolymerization process, the addition of ceramic powder increases physical complexity. Hence, large scale adoption and optimization of AM for ceramics requires a thorough understanding of the underlying physics. This work focuses on the light scattering introduced through a complex interplay between optical properties of different constituents and its effect on the photopolymerization. The effect of the shape of the ceramic particle is investigated for isolated and multiple particle cases using a parametric analysis with regular convex polygons. Although the analysis of two-dimensional isolated particle shapes indicates a preference for one shape over the other, this difference vanishes in a multiple-scattering situation. A three-dimensional analysis furthermore shows that a two-dimensional approximation of the three-dimensional scattering problem is relevant and can be used to further the process understanding of ceramic VP.

Reproduced from: Westbeek, S., van Dommelen, J. A. W., Remmers, J. J. C. & Geers, M. G. D. Influence of particle shape in the additive manufacturing process for ceramics. *Computers & Mathematics with Applications* **78,** 2360–2376 (Oct. 2019)

3.1 Introduction

Fabricating ceramics through additive manufacturing (AM) techniques is promising, facilitating near-net product fabrication that would not be feasible using conventional production techniques. Although it is possible to produce monolithic ceramics through a single-step process, the most prevailing and prosperous strategies fall into the multiple-step category [4, 16, 21].

The multi-step AM production approach considered here is based on vat photopolymerization (VP) and is shown in Fig. 1.3. Initially, ceramic powder with a particle diameter of the order of 1 µm is dispersed into a photopolymeric resin with a high filling fraction, typically of the order of 50–60 vol%. The resulting highly viscous fluid, termed a slurry, is then the base material for the indirect VP process. An intermediate "green" part is produced by a repetitive process of depositing a layer of slurry, patterned irradiation by UV light with a wavelength in the order of $\mathcal{O}$(400 nm) and lowering the base platform [54]. The green part, a composite material of ceramic inclusions in a polymer matrix is then subjected to a series of heat treatments, which can be subdivided into a debinding step where the polymer is evaporated and a subsequent sintering step where the part is sintered into a dense monolithic part [31]. Note that the concept of polymer derived ceramics is not new and the AM step can be replaced by other conventional polymer-forming techniques, such as injection molding [117]. Consequently, extensive knowledge and experience exists on the polymer-to-ceramic conversion [16, 117]. The real interest therefore lies in the part shaping step by AM, i.e. the highlighted block in Fig. 1.3.

With the maturing of AM techniques in general, the need for suitable simulation tools to improve fundamental understanding of the process increases. A clear motivation for this can be found in the most prominent factors limiting a wide adoption of AM in industry, namely reproducibility, productivity and scalability [57]. For ceramics in particular, a number of additional challenges consist in increasing the material density, increasing feasible product sizes and wall thicknesses and avoiding the formation of cracks [16].

Another challenge in VP for ceramics is the light scattering introduced by the dispersed inclusions. This phenomenon is dominated by the difference in refractive indices between the resin and the ceramic particles [31, 40–43]. As a result, the cured polymer geometry can be considerably different from the expected geometry for unfilled solutions (as a function of the light source). Additionally, the light dispersion through the slurry is also much less homogeneous due to an interplay between diffraction and interference at the considered length scales [78]. The inhomogeneous intensity distribution might, in turn, lead to an inhomogeneous polymer conversion or even the presence of residual monomer. The latter has been identified as a cause for crack formation during post-processing of the green part [51]. From the polymer-to-ceramic production chain it is known that high-quality green parts require a powder compact with a highly homogeneous microstructure and powder packing density [16]. The

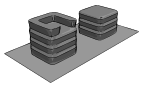

influence of powder shape is however less studied and clear guidelines are missing. In view of the light scattering phenomena, the actual shape might play an important role in reaching a homogeneous as possible final conversion. This work therefore aims to identify the influence of the particle shape in the vat photopolymerization step in the AM process.

Within the field of VP for ceramics, the primary interest in experimental and computational analysis has been focused on estimating the slurry's cure depth. Different factors have been recognized which influence the result, including the difference between refractive indices of the resin and powder, the powder volume fraction and (mean) diameter, and the light wavelength [31, 42, 118, 119]. Typically, this dependence was found empirically. Similar approaches also exist to relate the cure depth to the cure width [42, 118]. Many analytical approaches, such as the Kubelka-Munk theory, are limited to a two-way prediction, i.e. transmission and reflection in the opposite direction [120–122]. In order to numerically predict the full cure profile as a result of the applied light source, Sun & Zhang [123, 124] implemented a Monte-Carlo ray tracing approach using Mie single-scattering theory to determine the probability density function for the scattering direction. An early warning that using a spherical shape (through e.g. Mie theory) for non-spherical particles may lead to ambiguous results was made by Thiele & French [88]. They concluded this on the basis of a finite element scattering analysis of one (or two) representative rutile titania particle(s) in a coating.

In this work, a finite element model is used to obtain the near-field intensity field induced by the particle's shape, governing photopolymerization. In the following section the theory underlying this approach is addressed and two parameters are introduced to quantify the effect of the particle shape on the homogeneity of the intensity distribution and the resulting photopolymerization. The influence of particle geometry and orientation is first investigated in a two-dimensional setting in Section 3.3, using academic model problems with parametrized regular and convex polygon shapes. The translation to three-dimensions is made in Section 3.4, on platonic solids and shapes introduced to investigate the representative nature of a two-dimensional simulation in order to address a realistic three-dimensional configuration.

3.2 Mathematical framework

To identify the relevant phenomena induced by the particular shape of the inclusions on the electromagnetics fields, Maxwell equations are solved capturing the wave-like behavior of light. The reasoning for this is twofold. Firstly, due to the large filling fraction and the small difference between light wavelength and particle dimensions, which are both of the order of 1 μm, a wave description is required [85, 86]. Phenomena such as interference and diffraction play an important role in this regime, where the ratio of the feature size to wavelength is smaller than ten. Refractive optics such as ray tracing are not able to capture these phenomena and should be applied only when the scattering object is over 100 times the size of the wavelength [85]. Secondly, the large

filling fraction introduces so-called multiple-scattering that prohibits the application of single-scattering approaches such as the Mie theory, which is only applicable for highly dilute suspensions [86, 87]. The theory described next is used to analyze the shape influence on the intensity homogeneity using both single- and multiple-particle and both 2D and 3D models in Sections 3.3 and 3.4.

3.2.1 *Wave equation*

In a numerical solution framework, the Maxwell equations are typically combined into a single formula. To this end, constitutive equations are used to eliminate the dependence of the electric field on the magnetic field or reversely. Here the former is used, such that the equilibrium equation reads [93]

$$\vec{\nabla} \times \left(\frac{1}{\mu} \vec{\nabla} \times \vec{E} \right) + \varepsilon \frac{\partial^2 \vec{E}}{\partial t^2} + \gamma \frac{\partial \vec{E}}{\partial t} = - \frac{\partial \vec{J}^{\text{imp}}}{\partial t}, \tag{3.1}$$

where $\vec{E}$ is the electric field, μ the magnetic permeability, ε the electrical permittivity, γ the electrical conductivity, $\vec{\nabla}\times$ the curl-operator, $\vec{J}^{\text{imp}}$ the imposed electrical current density and t the time. By definition, the total current density $\vec{J}$ is equal to $\vec{J}^{\text{imp}} + \gamma \vec{E}$. Alternatively, under the assumption that the electric field takes the time harmonic form $\vec{E}(\vec{x}, t) = \Re\left(\vec{E}(\vec{x}) e^{i\omega t} \right)$, Eq. (3.1) can be rewritten in the frequency domain yielding [93, 94]

$$\vec{\nabla} \times \left(\frac{1}{\mu} \vec{\nabla} \times \vec{E} \right) - \left(\omega^2 \varepsilon - i\omega\gamma \right) \vec{E} = -i\omega \vec{J}^{\text{imp}}, \tag{3.2}$$

where ω is the angular frequency. The analogy to light modeling becomes apparent by introducing the wave number k in free space as [94, 95]

$$k_0 = \frac{\omega}{c_0} = \omega \sqrt{\mu_0 \varepsilon_0}, \tag{3.3}$$

with c_0 the speed of light in vacuum and μ_0 and ε_0 the permeability and permittivity in vacuum. Considering the values in free space, μ_0 and ε_0, are constant, a relative dimensionless material parameter is often introduced in the form of μ_r and ε_r, with $\mu = \mu_0 \mu_r$ and $\varepsilon = \varepsilon_0 \varepsilon_r$. This, together with Eq. (3.3), allows rewriting Eq. (3.2) as

$$\vec{\nabla} \times \left(\frac{1}{\mu_r} \vec{\nabla} \times \vec{E} \right) - k_0^2 \left(\varepsilon_r - \frac{i\gamma}{\varepsilon_0 \omega} \right) \vec{E} = \vec{0}. \tag{3.4}$$

The second term is often simplified further using a complex form of the permittivity, i.e.

$$\tilde{\varepsilon_r} = \varepsilon_r - \frac{i\gamma}{\varepsilon_0 \omega}. \tag{3.5}$$

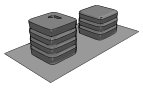

Since ceramics and polymers are typically dielectric, the relative magnetic permeability μ_r is (very close to) unity [95]. Consequently, the complex relative permittivity can be written as

$$\tilde{\varepsilon}_r = (n - i\kappa)^2 \equiv \tilde{n}^2, \tag{3.6}$$

where n is the refractive index and κ the extinction coefficient of the material. Using $\mu_r = 1$, the inhomogeneous vector curl-curl equation becomes [95]

$$\vec{\nabla} \times \left(\vec{\nabla} \times \vec{E} \right) = k_0^2 \tilde{n}^2 \vec{E}. \tag{3.7}$$

This differential equation is solved using the finite element framework. Note that the magnetic field $\vec{H}$ can be recovered through the original Maxwell's equations, i.e. through Faraday's law as [90, 93, 95]

$$\vec{H} = -\frac{i}{\omega\mu} \vec{\nabla} \times \vec{E}. \tag{3.8}$$

3.2.2 *Boundary conditions*

The vector wave equation for the electric field must be complemented by appropriate boundary conditions. A visualization of the applied conditions is provided in Fig. 3.1.

Along the interface between different media, i.e. the matrix and inclusion material in this case as illustrated by the red line in Fig. 3.1, the jump conditions must be satisfied [90, 125]:

$$\begin{aligned} \vec{n} \times \left[\vec{E} \right] &= \vec{0}, \\ \vec{n} \cdot \left[(i\omega\varepsilon + \gamma) \vec{E} \right] &= 0, \end{aligned} \tag{3.9}$$

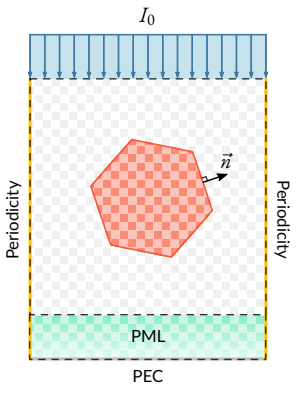

Figure 3.1 Illustration of the considered boundary conditions.

where $[\cdot]$ denotes the jump of the quantities from one side of the interface to the other and $\vec{n}$ is the unit normal outward vector. A Neumann boundary acting as the port condition for the incoming light is provided as

$$\vec{n} \times \left(\frac{1}{\mu} \vec{\nabla} \times \vec{E} \right) = -i\omega \vec{J}_s^{\,\mathrm{imp}}, \tag{3.10}$$

with $\vec{J}_s^{\,\mathrm{imp}}$ an imposed electrical surface current tangent to the boundary. The corresponding source intensity I_0, which will be defined in Section 3.2.4, is illustrated by the blue arrows in Fig. 3.1. In order to truncate the computational domain, an absorbing boundary condition is used in the form of a perfectly matched layer (PML) [110]. A PML can be considered as a finite layer surrounding the physical domain where the principle of coordinate stretching is applied through modification of the material parameters [90, 126]. Typically, the domain extended by the PML is bounded by a perfect electric conductor (PEC) or Dirichlet boundary condition, which reads

$$\vec{n} \times \vec{E} = \vec{0}. \tag{3.11}$$

Alternatively, the considered domain size is also reduced by using periodic boundary conditions as indicated in Fig. 3.1. Within electromagnetics the corresponding boundary condition stems from Bloch-Floquet's theorem, which states that fields on opposite surfaces are related through a constant phase shift [90, 127].

3.2.3 Discretization

Using regular FE elements in inhomogeneous electromagnetic problems can lead to non-physical or spurious solutions, primarily due to the lack of enforcement of the divergence condition [90]. Furthermore, imposing boundary conditions is inconvenient at material interfaces and conducting surfaces. Lastly, treating conducting and dielectric edges and corners is cumbersome due to the associated singularities. A common solution to these problems was proposed in the 1980s in the form of vector elements that assign degrees of freedom to the edges rather than to the nodes of the elements, thus called edge, vector or Nédélec elements [90, 91, 111, 112]. The degrees of freedom of these edge elements typically correspond to the integral of the tangential component (of either $\vec{E}$ or $\vec{H}$) along the edges of the patches. Because a quadrilateral mesh shows a larger cumulative phase error in comparison to a triangular mesh, the latter will be used in the following [90]. In this work the finite element package Comsol 5.0 [94] is used for the corresponding numerical analyses.

3.2.4 Photopolymerization

Although the numerical framework solves for the electric and magnetic fields, the real interest here lies in the (resulting) photopolymerization. In order to relate the electromagnetic waves to the chemical reaction, a conversion to light intensity/irradiance

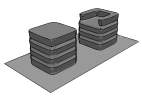

is required. The electric and magnetic fields are akin to the local intensity through the Poynting vector:

$$\vec{S} = \vec{E} \times \vec{H}^*, \tag{3.12}$$

where $\vec{H}^*$ denotes the complex conjugate of the magnetic field $\vec{H}$ and $\vec{S}$ represents the directional energy flux in $\mathrm{W/m^2}$. The intensity then simply follows from the magnitude of the time averaged Poynting vector [94, 95, 98], i.e.

$$I = \|\langle \vec{S} \rangle\| = \left\| \frac{1}{2} \Re\left\{ \vec{E} \times \vec{H}^* \right\} \right\|, \tag{3.13}$$

where $\langle \cdot \rangle$ indicates a time average and $\|\cdot\|$ the L^2-norm. For heterogeneous media, Eq. (3.13) provides the near-field information required to describe the polymerization process.

In order to quantify the influence of the ceramic powder, one option is to compare the local resulting intensity to the expected intensity without the presence of inclusions. If the magnitude of the absorption is neglected and a homogeneous plane wave source is assumed, a quantifier for the *intensity inhomogeneity*, $\mathcal{I}_I$, can be formulated as

$$\mathcal{I}_I = \frac{1}{V I_0} \int |I_0 - I(x)| dV, \tag{3.14}$$

where V denotes the considered volume, I_0 and $I(x)$ are the (uniform and constant) source intensity and composite intensity field, respectively, and the brackets $|\cdot|$ indicate the absolute value of the term in between. Note that Eq. (3.14) equals the volume average of the absolute intensity difference compared to the unfilled resin.

The light intensity is related to the photopolymerization through the polymerization rate, i.e. the conversion rate of monomer [78]:

$$R_p = -\frac{d[M]}{dt} = \mathcal{P}_M \sqrt{I}[M], \tag{3.15}$$

where $[M]$ is the monomer concentration and $\mathcal{P}_M$ is a lumped polymerization factor. $\mathcal{P}_M$ can be a function of conversion, initiator, inhibitor, temperature, etc [53, 70, 99, 100]. The degree of conversion is defined as the concentration of monomer that has been converted into polymer normalized to the initial monomer concentration, i.e. [53]

$$p = \frac{[M]_0 - [M]}{[M]_0}, \tag{3.16}$$

with $[M]_0$ the initial monomer concentration. To quantify the polymerization due to the inhomogeneous intensity field (compared to the homogeneous unfilled situation), a

second inhomogeneity quantification term is formulated and termed the *conversion based intensity effectiveness*:

$$\mathcal{E}_p = \frac{1}{V}\int \frac{e - \exp\left(1 - \sqrt{I(x)/I_0}\right)}{e-1} dV, \tag{3.17}$$

where $e = \exp(1)$. Note that $\exp\left(-\sqrt{I(x)/I_0}\right)$ in Eq. (3.17) is the functional term motivated by Eqs. (3.15) and (3.16), whereas the remaining terms are merely introduced to ensure $\mathcal{E}_p\left(I(x) = I_0\right) = 1$ and $\mathcal{E}_p\left(I(x) = 0\right) = 0$.

3.3 Analysis of the role of the inclusion shape

The influence of the inclusion shape is first analyzed in a two-dimensional framework. The motivation for this lies in the numerical efficiency of the analysis compared to a three-dimensional formulation. The question whether the resulting conclusions translate to 3D is addressed in Section 3.4. The analysis is first conducted on an isolated particle, subsequently moving to a more realistically filled resin.

3.3.1 Model formulation

The mathematical framework described in the previous section allows for an electromagnetic analysis of a particle-filled resin. Focus is put on isolating the effect of the inclusion shape, initially through a single-scattering analysis.

3.3.1.1 Isolated shape analysis

To parametrize and systematize the two-dimensional shape analysis, regular convex polygons of order n are used, as displayed in Fig. 3.2. The volume of the different shapes is equal to that of the 1 µm diameter circular shape denoted with $n = \infty$.

To accommodate the scatter-analysis, the electric field $\vec{E}$ is split into a background plane-wave excitation field $\vec{E}_0$ and a resulting scattered field $\vec{E}_s$, i.e. $\vec{E} = \vec{E}_0 + \vec{E}_s$, while only solving the latter [128]. To do so, the scatterer (which is embeded in the domain of interest) is bounded by an artificial layer, where the PML is applied [129]. Note that

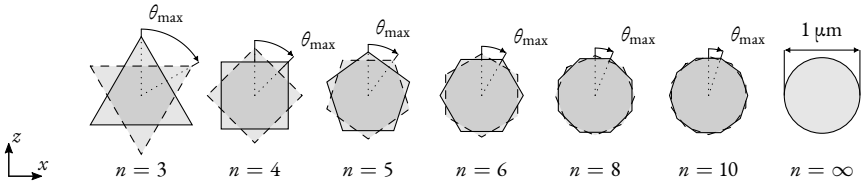

Figure 3.2 Different polygonal shapes with identical volume of which the orientation is specified by the unique rotation angle θ_{max} (denoted by the arrow).

in contrast to the boundary conditions illustrated in Fig. 3.1, here a PML surrounds the whole physical domain along all four edges. The physical embedded domain has dimensions of $x \times z = 8 \times 8\ \mu m^2$, with the inclusion centered in the horizontal middle and 2 μm from the top. The light with intensity I_0 is propagating from a uniform source in the negative z-direction, i.e. from top to bottom. This configuration puts the scatterer close to the light source with sufficient space on the other side to display the resulting inhomogeneity. The width is also chosen 8 μm to capture scattering effects in the direction perpendicular to the illumination resulting from different orientations. These domain dimensions were found to provide converged trends in the results, without being unnecessarily large. To investigate the effect of the inclusions' orientation with respect to the incoming light, they are rotated over an angle $\theta = 0$ to $\theta = \theta_{max}$ as illustrated in Fig. 3.2, where $\theta_{max} = \pi/n$ rad. Note that this is only half of the polygon's rotation symmetry angle due to symmetry of the defined problem.

3.3.1.2 *Multiple-scattering*

Although the model with a single inclusion provides a clear insight into the effect of the orientation of an isolated particle, a typical slurry will have a high filling content of particles with an arbitrary orientation. To investigate the cumulative effect of many scattering events, a multi-particle model is also used. The physical domain in this model is $x \times z = 6.5 \times 11.5\ \mu m^2$ and contains 38 inclusions, such that the filling fraction equals $\varphi = 0.40$. Uniformly distributed light enters the domain through the top edge with intensity I_0. The left and right boundaries are coupled through Bloch-Floquet periodic boundary conditions and the domain is extended through a PML at the bottom, see Fig. 3.1.

3.3.1.3 *Material properties and model parameters*

The required material properties for the models in Sections 3.3.1.1 and 3.3.1.2 are provided in Table 3.1 and representative for a typical acrylic resin with alumina powder as the ceramic filler. In the considered domains, the absorption of the resin has been neglected because its effect would be insignificant within the considered length scales [78]. At these wavelengths the absorption of the ceramic inclusions can also be

Table 3.1: Considered material properties and model parameters.

Parameter	Value	Unit	Description	Source
r_o	0.5	[μm]	Radius of spherical particle	
n_r	1.5	[-]	Refractive index of resin	[28, 101]
n_c	1.78	[-]	Refractive index of alumina powder	[101]
λ	400	[nm]	Wavelength of UV light in vacuum	
I_o	100	[W/m^2]	Light source intensity	

neglected [31]. The applied light source intensity I_0 and wavelength λ are also specified in Table 3.1.

3.3.2 *Results*

Before presenting the more representative case of multiple-scattering in Section 3.3.2.2, the impact of a single inclusion's shape and orientation on the light propagation is addressed first.

3.3.2.1 *Analysis on isolated particle*

The different inclusions displayed in Fig. 3.2 are rotated over 13 unique angles from $\theta_1 = 0$ to $\theta_{13} = \theta_{max}$. The resulting total intensity field in the $8 \times 8\ \mu m^2$ domains for the intermediate rotation angle (θ_7) are displayed in Fig. 3.3. The graphs

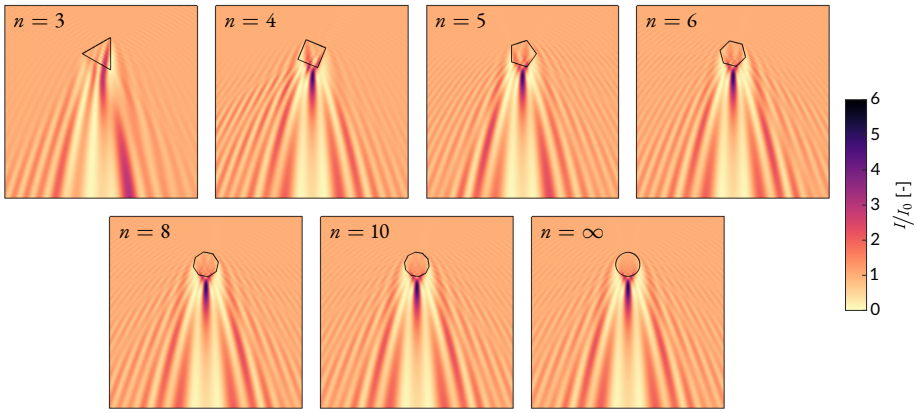

Figure 3.3 Normalized intensity field I/I_0 in the $8 \times 8\ \mu m^2$ domain for $n = 3, 4, 5, 6, 8, 10$ and ∞ at $\theta_7 = \pi/2n$.

illustrate the influence of the inclusions on the intensity field I, compared to the initially homogeneous intensity distribution I_0, which is used to normalize the results. Notice that already for polygons with $n = 6$ and higher, there is no clear (visible) difference in the resulting field compared to the circular inclusion. In order to quantify the effect of the shape and orientation of the particles, Fig. 3.4 shows the resulting intensity inhomogeneity parameter $\mathcal{I}_I$. The graph reveals several interesting trends. First of all, the peak inhomogeneity for all shapes coincides with the maximum rotation angle. By the choice of the initial orientation, i.e. with an edge facing downwards (cf. Fig. 3.2), the peak intensity at θ_{max} thus corresponds to a corner pointing in the direction of light propagation. Secondly, as illustrated by the average $\mathcal{I}_I$ (the dashed blue line in Fig. 3.4), the corresponding value largely coincides with the result for the intermediate rotation angle as depicted in Fig. 3.3. Additionally, the dominant trend in the angle dependency

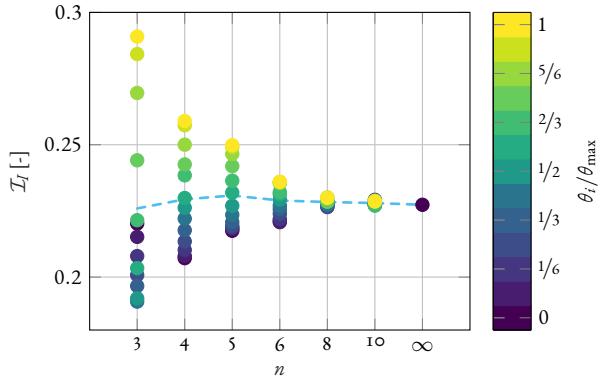

Figure 3.4 $\mathcal{I}_I$ distribution for the different polygonal shapes over 13 equidistant angles from $\theta = 0$ to θ_{max}. The average value is indicated by the blue dashed line.

is a decrease in $\mathcal{I}_I$ for $\theta \rightarrow 0$. The exception here is the triangular particle, which for increasing rotation angles initially shows a decrease followed by a steeply increasing inhomogeneity. Overall, the bandwidth of $\mathcal{I}_I$-values increases with a reduction in the polygon-order n. The latter two trends are further highlighted in Fig. 3.5, which displays $\mathcal{I}_I$ as a function of the actual orientation angle. Whereas all lines for $n > 3$ initially have a positive slope, the line with $n = 3$ initially descends. Fig. 3.5 also reflects the rotational symmetry for the intensity inhomogeneity of the different polygons analyzed.

An alternative intensity inhomogeneity quantification parameter, linked to its effect on the conversion, was introduced in Section 3.2.4, termed $\mathcal{E}_p$, for which the results are provided in Fig. 3.6. Considering both Figs. 3.4 and 3.6, similar trends emerge with respect to, e.g., range of $\mathcal{I}_I$ and $\mathcal{E}_p$ values for the corresponding polygon order. Whereas $\mathcal{I}_I$ did not show a clear trend with respect to the average inhomogeneity for increasing

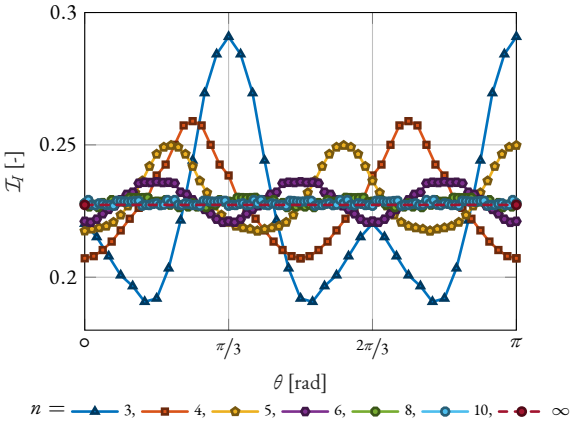

Figure 3.5 $\mathcal{I}_I$ as a function of the inclusion orientation θ.

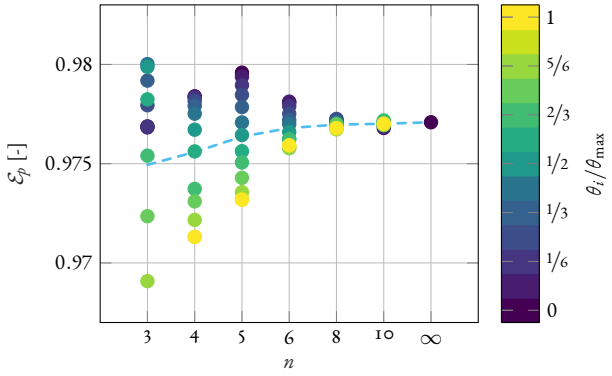

Figure 3.6 $\mathcal{E}_p$ distribution for the different polygonal shapes over 13 equidistant angles along θ_{max}. The average value is indicated by the blue dashed line.

polygon order, the average $\mathcal{E}_p$ does show a clear improvement of conversion effectiveness for increasing n. The orientation dependence for $\mathcal{E}_p$ appears to be of opposite sign compared to that of $\mathcal{I}_I$, indicating that while the inhomogeneity in the intensity-field decreases, the conversion effectiveness increases.

3.3.2.2 Analysis on multiple-scattering

The case of a single inclusion is not representative for a slurry with a high solid filling fraction. Here, a filling fraction of $\varphi = 0.40$ is considered for 50 different realizations of randomly positioned and oriented polygons of a single type in a horizontally periodic 6.5×11.5 μm^2 domain. Three realizations for the different polygons (n) are depicted in Fig. 3.7, including the resulting intensity field. At first glance, no characteristic features can be identified that are coherent for a specific polygonal order. To scrutinize possible hidden trends in these results, a statistical analysis is performed on the inhomogeneity parameters. The results of this analysis are displayed in Fig. 3.8. Note that the horizontal spread for each n has only been added to reveal overlapping values. For each polygon shape the central red line inside the boxes indicates the mean value and the light red and blue box represent the standard error of the mean within a 95% confidence interval and the standard deviation, respectively. Based on Fig. 3.8, no trends can be identified in either $\mathcal{I}_I$ or $\mathcal{E}_p$. It has been verified that there is no inclination towards certain orientation angles for any of the polygons, i.e. the inclusions are randomly oriented. Note that the multiple-scattering significantly increases the inhomogeneity in the intensity $\mathcal{I}_I$ compared to the single scattering situation, but this trend is not repeated by $\mathcal{E}_p$, implying that although the inhomogeneity in the intensity field increases, the average conversion effectiveness is analogous to the single-scattering case. An interesting finding is the occurrence of $\mathcal{E}_p$-values larger than 1, which are attributed to the choice of model (both material and boundary) conditions. Due to the introduction of multiple-scattering and the periodic boundary conditions, the incoming light is partially refracted towards

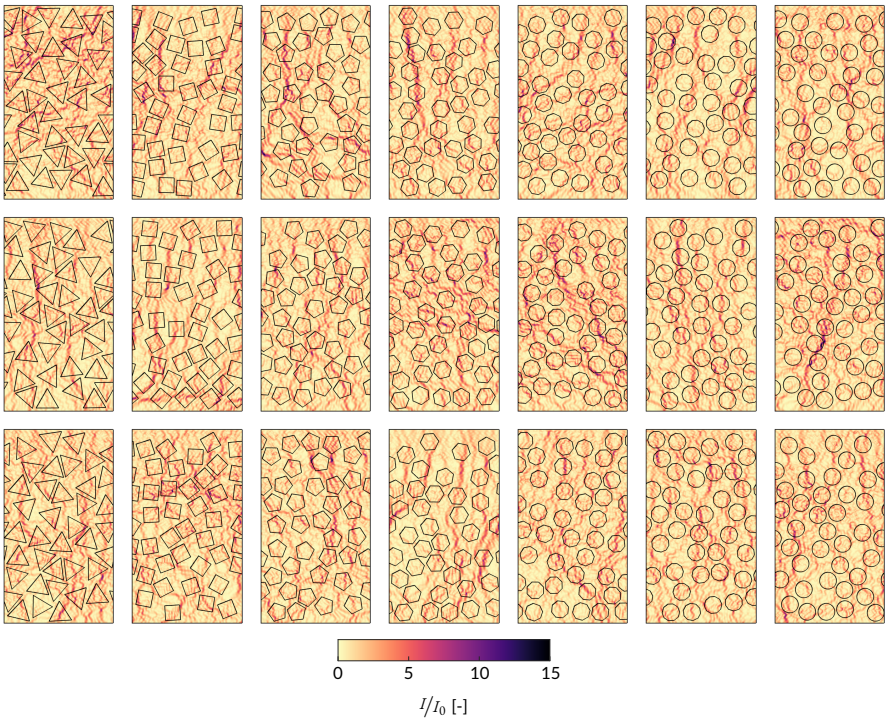

Figure 3.7 Intensity field for (from left to right) $n = 3, 4, 5, 6, 8, 10$ and ∞ for three different random realizations.

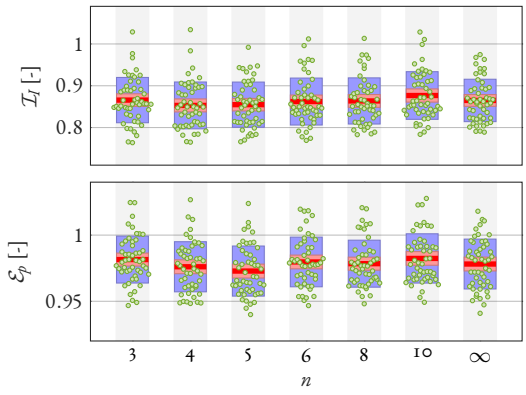

Figure 3.8 Distribution of $\mathcal{I}_I$ and $\mathcal{E}_p$ for 50 random realizations per polygonal shape. For each shape, the result of the 50 realizations is displayed by the markers. The red line indicates the average value, the light red box its 95% confidence interval and the blue box the standard deviation.

the horizontal direction, causing the average intensity in the domain to increase. The resulting higher peak intensity (cf. Fig. 3.7) in turn causes the increased $\mathcal{I}_I$-values. Note that the average in- and out-flow components of the intensity $\langle S_y \rangle$ are still equivalent to I_0. Considering a non-periodic setting this convincingly illustrates the effect of broadening of the cure profile as observed experimentally. Even though the scattering events (in these infinitely periodic domains) increase the local average intensity, the mean $\mathcal{E}_p$-value is still below 1, i.e. a homogeneous intensity profile equal to I_0 still leads to more effective photopolymerization. Note that the corresponding homogeneous conversion would also be preferential considering the absence of residual monomer.

3.4 Three-dimensional analysis

Multiple inclusion simulations similar to the ones illustrated in Fig. 3.7 quickly become computationally very demanding in a three-dimensional framework. To alleviate this, it will therefore be verified whether the dominant trends in two-dimensions (qualitatively or quantitatively) can be extrapolated to three-dimensional powder processes.

3.4.1 Model formulation

The most logical extension translating the two-dimensional regular, convex polygons to three-dimensional particles is to use platonic solids, which are regular, convex polyhedra. In total there are five of those geometries, i.e. the tetrahedron, hexahedron or cube, octahedron, dodecahedron and icosahedron [130]. Here, the latter four, as illustrated in Fig. 3.9, are considered and compared to the perfect sphere. The sizes are scaled such

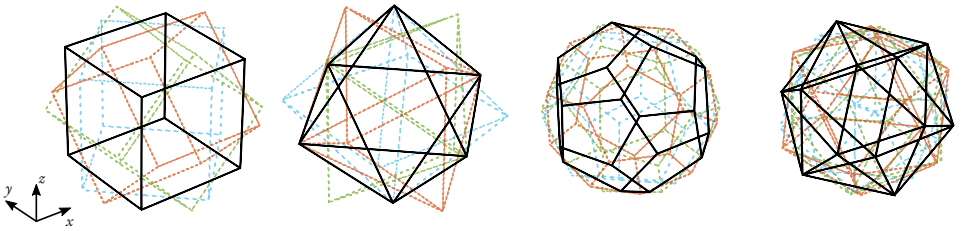

(a) Hexahedron (12, 6) **(b)** Octahedron (12, 8) **(c)** Dodecahedron (30, 12) **(d)** Icosahedron (30, 20)

Figure 3.9 Platonic solids and the considered orientations (along the major axis) with the number of edges e and faces f denoted as (e, f).

that the volumes of all considered geometries are equal to that of the sphere with 0.5 µm radius. Whereas the hexahedron and octahedron and the dodecahedron and icosahedron have the same number of edges, respectively 6 and 12, the number of faces increases from 6, 8, 12 to 20. Consequently, judging from the number of faces, from left to right in Fig. 3.9 the shapes are ordered to more and more resemble the sphere. Whereas in a two-dimensional simulation the orientation of the inclusions can only be varied along the

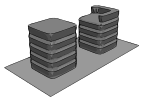

out-of-plane y-axis, now two perpendicular axes, x and z, can also be considered. The initial inclusion orientation (the black solid line in Fig. 3.9) with its local 1-, 2- and 3-axis aligned with the global x-, y- and z-axis, respectively, is rotated around the x-, y- and z-axis. The rotations over the major axes are illustrated by the dashed lines in Fig. 3.9.

In order to provide a direct relationship between the two-dimensional results and the corresponding three-dimensional representation, a second series of 3D shapes are considered. In converting the 2D geometries from Fig. 3.2 to 3D, instead of performing an out-of-plane extrusion, the even-n shapes are revolved around the z-axis. This revolution is both applied to the initial geometry with $\theta_0 = 0$ and the geometry with $\theta_0 = \theta_{\max}$ (angles in Fig. 3.2). The resulting three-dimensional geometries are shown for $\theta_0 = 0$ and $\theta_0 = \theta_{\max}$ in Figs. 3.10a to 3.10d and Figs. 3.10e to 3.10h, respectively. The three-dimensional shapes will next be rotated around the y-axis (equivalent to the

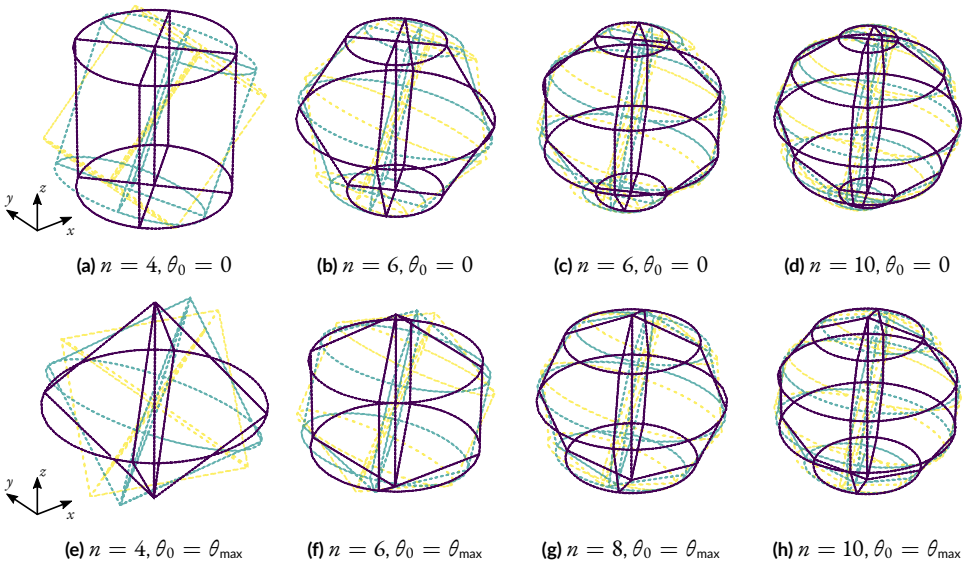

Figure 3.10 Two-dimensional shapes revolved around the z-axis in a 3D shape, by using the 2D configuration with either $\theta_0 = 0$ (Figs. a-d) or $\theta_0 = \theta_{\max}$ (Figs. e-h). Shape color corresponds to the $\theta_i/\theta_{\max}$ bar in Figs. 3.4, 3.6 and 3.12.

two-dimensional analysis) over angles from $\theta = 0$ to $\theta = \theta_{\max}$ as indicated in Fig. 3.10 by the lighter wireframe geometries at $\theta = \frac{1}{2}\theta_{\max}$ and $\theta_{\max}$.

For both three-dimensional models, i.e. with platonic solid inclusions and revolved geometries, the computational domain is limited to $x \times y \times z = 1.5 \times 1.5 \times 2.5$ μm^3, with periodic boundary conditions on the xz- and yz-planes. The light enters the domain from the top and the bottom surface is extended by an absorbing PML, in accordance with Fig. 3.1. The inclusion is placed 0.75 μm from the top surface in the horizontal middle and model parameters follow from Table 3.1.

3.4.2 Results

The platonic shapes as described in Section 3.4.1 are analyzed first to examine the influence of geometry and orientation. A comparison to two-dimensional results follows in Section 3.4.2.2.

3.4.2.1 Platonic solid geometries

Compared to the initial orientation, the black solid line in Fig. 3.9, the platonic shapes are rotated around the x, y and z-axis over intervals from $0 - 90$ degrees. Consequently, at least a full rotational symmetry is captured for the individual shapes. The $0-90$ degree interval is subdivided into both $[0, 30, 60, 90]$ and $[0, 45, 90]$ degree combinations. This does not provide a full orientation map, but still involves $4^3 + 3^3 = 91$ possible orientations (not subtracting multiply defined combinations). To further reduce this orientation set, the considered orientations are limited to the ones with a uniquely oriented 3-axis. This limiting choice implies that for each 3-axis orientation, only a single 1- and 2-axis orientation is evaluated. Here, the convention is used that the local inclusion axes initially correspond to the global axes, i.e without rotation the local 1, 2 and 3-axis coincide with the x, y and z-axis, respectively. A total number of 61 orientations, i.e. simulations, were finally considered to investigate the shape orientation dependence of the platonic solids. It is interesting to emphasize the resulting computational demand for these. Whereas the two-dimensional simulations can still be performed on a portable system with 8 GB of RAM using a direct solver for $\mathcal{O}(2.5 \text{ million})$ degrees-of-freedom, the three-dimensional simulations considered here require approximately 60 GB of RAM using a GMRES iterative solver with a multi-grid preconditioner for $\mathcal{O}(8 \text{ million})$ degrees-of-freedom.

The results of this analysis are visualized in Fig. 3.11 for both $\mathcal{I}_I$ and $\mathcal{E}_p$. The result for the sphere is also included for comparison. Note that the restricted range of angles may not provide a full statistical analysis, but it is merely used to identify the spread in the obtained results. Similar to previous graphs, the central red line indicates the mean value and the light red and blue box represent the standard error of the 95% confidence interval of the mean and the standard deviation, respectively. The horizontal spacing between data points only serves to separate overlapping data points. Note that a quantitative comparison to the results of the two-dimensional isolated shape analysis should not be done here, given the reduced domain size and periodic boundary conditions applied here. The physical geometry reflects a horizontal layer with inclusions arranged in a regular grid. Consequently, neighboring particles do influence the light propagation and, although periodic at the particle scale, more resembles the multiple-scattering case.

Fig. 3.11 shows a trend of increasing inhomogeneity $\mathcal{I}_I$ from left to right, so the order hexahedron - octahedron - dodecahedron - icosahadron indeed converges to the sphere. Equivalently, the spread in results narrows towards the sphere, which is independent of the orientation. The distinction between the number of edges, 12 versus 30 for the former and latter two shapes, can also be identified from the spread in data-points.

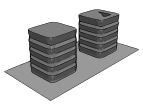

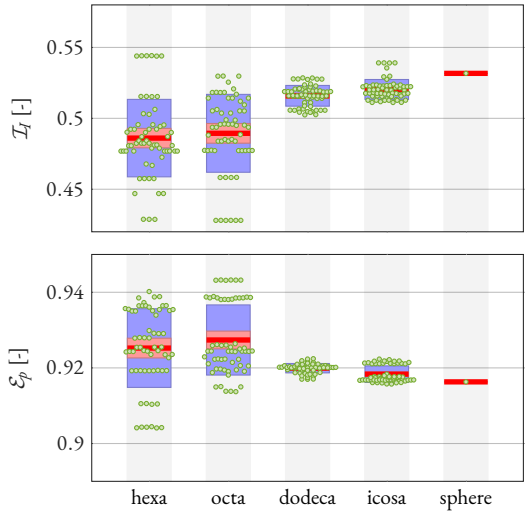

Figure 3.11 $\mathcal{I}_I$ and $\mathcal{E}_p$ results for the three-dimensional shapes for rotations over the x-, y- and z-axis of angles in range from $[0 : 30/45 : 90]$ deg. The red line indicates the average value, the light red box its 95% confidence interval and the blue box the standard deviation.

Comparing the hexa with the octa and the dodeca with the icosa, both pairs have a similar bandwidth with respect to the average confidence interval and the standard deviation. Similar conclusions can also be drawn from the $\mathcal{E}_p$-values, although the reduction in $\mathcal{I}_I$ translates to an increasing effectiveness $\mathcal{E}_p$. For these boundary conditions there appears to be a preference for lower order polyhedra, which contradicts the isolated two-dimensional analysis in Fig. 3.6. In comparison to the two-dimensional multiple-scattering simulation (cf. Fig. 3.8), the smaller magnitude of $\mathcal{I}_I$-values indicates that the regular grid does not promote significant horizontal light propagation. As a consequence the conversion effectiveness is now further reduced compared to the homogeneous case. The set of orientation angles considered induces a clear separation between two clusters of $\mathcal{E}_p$-values for the icosahedron while for the hexahedron and octahedron multiple orientations exist with clustered or equal $\mathcal{E}_p$-values. For a complete angle dependency the reader is referred to Appendix A where Figs. A.1 and A.2 display the results for $\mathcal{I}_I$ and $\mathcal{E}_p$ in polar graphs. The results from the analysis on platonic solids provide interesting insights, but it remains interesting to deduce whether a two-dimensional analysis is adequate in representing a three-dimensional physical process.

3.4.2.2 Revolved three-dimensional geometries

To facilitate a 2D-3D comparison, the second series of geometries is considered next, see Fig. 3.10. In order to make the comparison to the 2D results, the results for the revolved shapes in Fig. 3.10 are compared to two-dimensional simulations on a $x \times z = 1.5 \times$

2.5 μm^2 domain which is also periodic in the horizontal direction. As a consequence, the two-dimensional cross-section in the $y = 0$ plane is equal for the two- and three-dimensional analysis. Comparing the two- and three-dimensional results in fact implies a comparison between an extruded and a revolved three-dimensional polygon, respectively. The resulting $\mathcal{I}_I$ and $\mathcal{E}_p$-values are displayed in Fig. 3.12. The open circles denote the result from the two-dimensional model with periodic boundary conditions, which are clearly different from the results in Figs. 3.4 and 3.6. A first prominent difference is the magnitude of the $\mathcal{I}_I$ and $\mathcal{E}_p$-values. The $\mathcal{I}_I$-values are significantly higher in this case, because the domain of interest is smaller and inclusions are more closely packed together. Such an increase of $\mathcal{I}_I$ was already identified in the multiple-scattering simulations but also hold in the regular grid considered here. The $\mathcal{E}_p$-values on the other hand differ more from 1, i.e. the conversion based intensity effectiveness reduces. These findings indicate that although higher peak intensities exist, the average effective conversion decreases compared to the homogeneous domain or even the isolated particle case. The single exception to these conclusions is the point where the square ($n = 4$) is oriented at θ_{max}. In this orientation the corners of the square are close together, which results in a strong interaction between neighboring particles as reflected by both the $\mathcal{I}_I$ and $\mathcal{E}_p$-value. Similarly to some of the realizations in the two-dimensional multiple-scattering simulations, the effectiveness appears to be higher than in the homogeneous situation. This can again be attributed to the horizontal interactions and illustrates the significant

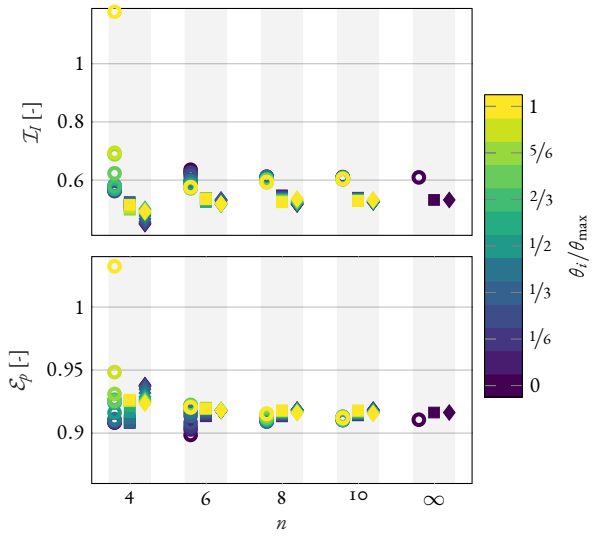

Figure 3.12 Results of the two-dimensional versus three-dimensional revolved shape analysis. Circles are the 2D results, the squares correspond to 3D shapes with a side initially perpendicular to the incoming light (Figs. 3.10a to 3.10d) and the rhombus depicts 3D shapes with corners initially aligned with the light direction (Figs. 3.10e to 3.10h).

effect of orientation for non-spherical particles. Another remarkable observation is that due to the difference in boundary conditions the trend in average $\mathcal{I}_I$- and $\mathcal{E}_p$-values is opposite to the one in Figs. 3.4 and 3.6, respectively. The slope of the $\mathcal{I}_I$ average shows opposite behavior compared to Fig. 3.4 and the effectiveness $\mathcal{E}_p$ improves for increasing polygon order. This clearly illustrates that using single scattering theories for multiple-scattering physics is not appropriate.

The high $\mathcal{I}_I$- and $\mathcal{E}_p$-values for $n = 4$ are not found in the three-dimensional simulations represented by the square and rhombus symbols in Fig. 3.12. This can most likely be attributed to the increase in average distance between the faces of neighboring particles. The squares in Fig. 3.12 correspond to revolved shapes with a side initially perpendicular to the incoming light (Figs. 3.10a to 3.10d), similar to the two-dimensional analysis, and the rhombus depicts results for revolved shapes with their corners initially aligned with the light direction (Figs. 3.10e to 3.10h). In a general sense, $\mathcal{I}_I$-values are higher in a two-dimensional setting but the bandwidth of results overlaps to a large extent with respect to $\mathcal{E}_p$. This indicates that although the inhomogeneity in the intensity field is overestimated in a two-dimensional setting, the effectiveness of the resulting conversion is equivalent. As expected from the initial orientation similarity, the orientation angle dependence of the shapes with $\theta_0 = 0$ is fairly similar to the two-dimensional analysis. This is more obvious for $\mathcal{E}_p$ than for $\mathcal{I}_I$, where $n = 4$ and 6 do not show this dependence. The $\mathcal{I}_I$- and $\mathcal{E}_p$-values for the revolved shapes with $\theta_0 = 0$ and $\theta_0 = \theta_{\max}$ are highly analogous. Compared to the platonic shapes, the $\mathcal{I}_I$-values are slightly higher (on average) for the revolved shapes, but the $\mathcal{E}_p$ is of the same order suggesting equivalent conversion effectiveness for all considered three-dimensional shapes. A conclusion that can be drawn from Fig. 3.12 is that although the intensity profile might be different on the local scale, the effective emanating conversion in a three-dimensional setting is approximated correctly by a two-dimensional analysis.

3.5 *Conclusions*

The role of the powder in the additive manufacturing process for ceramics can not be neglected. Clear effects were already identified in the initial attempts to print ceramics through vat photopolymerization, e.g. the pronounced broadening of the cure profile [31]. This work aimed to identify and quantify the effects introduced by particles in the VP process for ceramics, using a physics-based numerical modeling approach.

The numerical framework solves Maxwell's electromagnetic equations to capture the relevant effects emerging when the size of the particles is of the same order as the wavelength. From the resulting electric and magnetic vector field quantities, the field variable of interest can be obtained, i.e. the intensity or irradiance, which is the driving force for the photopolymerization reaction. The difference in refractive index combined with the inclusion geometry induces a large inhomogeneity in the intensity field due to the combined effects of reflection, refraction, interference and diffraction. The latter two physical effects can only be captured through a full wave description of the light.

In order to quantify the effect of the inclusions, two unique intensity-based quantities are defined. The first one, the *intensity inhomogeneity* $\mathcal{I}_I$, quantifies the deviation from the disturbed intensity field compared to the uniform homogeneous case. The second one, the *conversion based intensity effectiveness* $\mathcal{E}_p$, relates the non-homogeneous intensity field to the emanating polymerization reaction, without introducing additional material parameters. To parametrize the powder shape, particles are represented by polygonal (in 2D) or polyhedral (in 3D) shapes. This illustrates the academic nature of the study, considering the possible degree of randomness in actual powder shape, but at the same time allows for a clear and insightful study of the emerging effects.

Models with a single two-dimensional inclusion in a large uniform domain showed a small but clear trend favoring a higher-order polygon with respect to $\mathcal{E}_p$, on the other hand $\mathcal{I}_I$ does not show a clear trend. With respect to orientation dependence, lower $\mathcal{I}_I$ but higher $\mathcal{E}_p$ are found when the orientation is such that a flat side is opposite and perpendicular to the light origin, as is the case for $\theta = 0$ in the considered models. Moving towards the more realistic multiple-scattering situation, all influences of particle geometry vanishes and there is no statistical preference for one polygon shape over the other. A practical transformation of multiple particle models to a three-dimensional setting is computationally demanding. To restrict computational requirements, models with a single incorporated inclusion and prescribed periodicity in the direction perpendicular to the illumination direction are proposed. The difference of these horizontally stacked particles compared to the isolated case is already significant in a two-dimensional setting. No clear trend can be identified for $\mathcal{I}_I$, but the effectiveness $\mathcal{E}_p$ now increases for reducing polygon order. This finding illustrates the necessity of accounting for multiple-scattering. The considered three-dimensional shapes (both platonic and revolved polygons) show the same trend in $\mathcal{E}_p$, i.e. a reducing value for more sphere-like geometries. The intensity inhomogeneity $\mathcal{I}_I$ on the other hand increases towards the sphere. By comparing results of a two-dimensional simulation to three-dimensional equivalent revolved shapes, it becomes clear that the two-dimensional simulations do have a clear predictive value. Although the inhomogeneity in the intensity field is slightly overestimated in the two-dimensional framework, the correspondence is excellent compared to $\mathcal{I}_I = 0$ for the homogeneous case. Furthermore, the photopolymerization effectiveness $\mathcal{E}_p$ is very analogous for both two- and three-dimensions. Considering the interest lies in the conversion homogeneity resulting from the illumination step, the trends in the $\mathcal{E}_p$-value are deemed more important.

This study provides interesting insights for light scattering in a ceramic-resin system where typical properties of alumina and photopolymer resin are used. Nonetheless, it allows for other particle-matrix systems as well. The study illustrates the relevance of a two-dimensional analysis, preventing the need for highly computationally demanding three-dimensional simulations. However, a more generalized three-dimensional domain, with randomized placement and orientation, still needs to be explored.

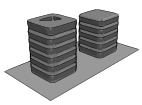

4

Multi-scale process simulation for particle filled vat photopolymerization

Abstract

The majority of research into vat photopolymerization (VP), has been focused on experimental investigations of the influence of process and material parameters. In a specific application of the VP technique, where the resin is filled with particles, this empirical approach has its limitations. In order to fully understand the relation between process parameters and the material properties a detailed numerical analysis is needed. In this chapter a multi-scale and multi-physical simulation approach to unravel such relations in the complex production process is presented. Using a homogenization approach, the influence of the filler particles, in this case alumina, on the light scattering, conversion characteristics and resulting effective thermal and mechanical properties is determined. The effective composite material and scattering properties are then used as input in a process simulation framework. This enables prediction of key filled-VP characteristics at a structural level. A mesh sensitivity analysis at the component scale reveals that adequate predictions may be obtained with a rather course discretization, facilitating multi-physics VP part simulations.

Reproduced from: Westbeek, S., Remmers, J. J. C., van Dommelen, J. A. W. & Geers, M. G. D. Multi-scale process simulation for additive manufacturing through particle filled vat photopolymerization. *Computational Materials Science* **180,** 109647 (July 2020)

4.1 Introduction

Additive manufacturing (AM) through vat photopolymerization (VP) or stereolithography is a powerful additive process based on selective UV illumination of a photo-reactive resin in a layer-by-layer fashion. VP is generally recognized as an AM technique with an excellent resolution in combination with high surface quality [23]. Although traditional photopolymerizable materials are limited to acrylic and epoxy resins [132], through the addition of a solid phase powder, the VP process can also be used to print other materials, for example in dental applications [53]. Appropriate subsequent binder removal even facilitates fabrication of dense monolithic non-polymer parts [16].

The current work considers a multi-step process for the fabrication of ceramics, as illustrated in Fig. 1.3, with the focus on the (highlighted) AM step itself. It should however be noted that the applicability of this work is not limited to ceramics only, but also includes other particle filled and even unfilled traditional VP resins.

The introduction of the ceramic powder in the polymer resin increases the complexity of the relevant physical processes involved. Besides rheological aspects (outside the scope of this work) in depositing the new layer of powder filled resin [58], i.e. the slurry, the presence of the powder strongly affects the illumination step. The powder particles typically have different optical properties than the resin, introducing light scattering. Due to the high filling fraction, this may have a profound effect on the shape and size of the cured profile [31]. A similar contrast in properties also holds for the thermomechanical characteristics. While typical resins show shrinkage during solidification, the rigid-like inclusions introduce inhomogeneities in the strain field and act as heat sinks for the exothermic heat generation [78]. These effects, although introduced at the small length scale of the particles, have a profound influence on the resolution and quality of the resulting printed composite part. A better understanding of the VP process for filled resins is therefore considered key to predict or resolve problems related to these effects [57], either before or during printing [62].

Starting from the pioneering work of Jacobs [54], different papers provide a better understanding of the VP process through mathematical/numerical approaches that can be categorized in two categories. Firstly, an extensive number of works focus on the development of more sophisticated polymerization models. Based on the illumination conditions, these contributions predict the spatial evolution of the degree of conversion whilst accounting for the photopolymerization kinetics [66–68], the presence of inhibitor species such as oxygen [69, 70] and photobleaching due to initiator consumption [71–75]. Examples that attempt a similar approach for powder filled resins are more scarce. A notable example is Ref. [76] where experimental work is used to determine the optical properties of the filled resin, to subsequently apply these in a simulation model to predict the solidified contour. More common are approaches that extend the exposure threshold model developed by Jacobs to account for the broadening (and shallowing) of the cure width (and depth) by the presence of inclusions

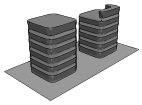

through emperical expressions [31, 41, 43, 60, 77]. Apart from the aforementioned photopolymerization models, secondly, phenomenological approaches exist that aim to capture the mechanical effect of the layered process due to shrinkage [55, 63–65, 133] or the resulting part's tensile strength [134], while considering individual layers as homogeneous.

To obtain an improved comprehension of the influence of a particle filler in the VP process, a numerical multi-scale process simulation framework is developed in this work that captures the effect of the inclusions, starting from the illumination of the monomer resin until the development of residual stresses and deformation in the printed part after solidification. The developed simulation framework distinguishes itself in three ways compared to (the aforementioned) published literature. *(i)* It combines the multi-physical nature of Ref. [78] with a multi-scale framework to capture the influence of the inclusions on the print process occurring at the component scale. *(ii)* The effective behavior is extracted in a homogenization approach starting from properties of individual constituents. *(iii)* It leads to a hybrid model compared to the two aforementioned approaches in literature, combining inhomogeneous layer conversion (kinetics) with the development of mechanical stress and deformation through process simulation.

This chapter presents a detailed description of the developed multi-scale VP process simulation framework for particle filled resins, with particular application to an alumina (Al_2O_3) ceramic slurry in a process with a scanning Gaussian UV laser source. The following section will introduce the relevant length scales and the physical background. The derivation of effective material properties is presented in Section 4.3. In order to demonstrate the relevance of the developed framework, it is applied to an illustrative academic case study in Section 4.4.

4.2 Mathematical description of the multiscale modeling framework

The relevant physical phenomena occur at a large variety of length scales, ranging from the wavelength of the UV light source, via the powder inclusions to a single layer and even the full component scale. To put this into dimensional numbers, the wavelength is in the order of $\mathcal{O}(400\ \text{nm})$, particles have diameters in the same order up to a few µm, layer thicknesses are 10s of µm with part sizes stretching (many) cms. Although the wavelength itself has little importance for unfilled polymer resins where the Beer-Lambert law is sufficient to predict light absorption, its relevance in particle filled resins has been shown in our previous contributions, cf. Refs. [78, 116]. The corresponding length scales vary from the light wavelength and particle diameter to the penetration depth of the light, which is typically somewhat larger than the layer thickness in VP applications. From a (thermo)mechanical point of view, the range of relevant length scales stretches even further, from the particle size (µm) to the full component dimensions (cm). Simulating all physical effects related to the presence of the inclusions in a single process simulation framework is therefore an unfeasible task.

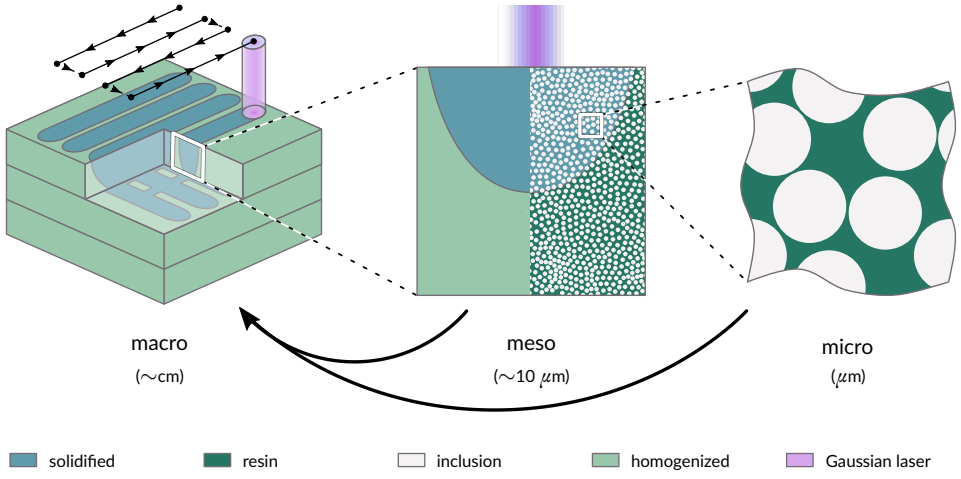

Figure 4.1 Graphical description of the multi-scale framework. From left to right the three depicted length scales are the macro-scale, the meso-scale and the micro-scale. The macro-scale graph illustrates insufficient cure introduced by a (too) large hatch-spacing

To account for the presence of the inclusions in the process simulation, a multi-scale framework is here proposed, consisting of three coupled length scales as depicted in Fig. 4.1. The full part scale where process boundary conditions are considered is referred to as the *macro-scale*, a length scale where homogenized effective properties are used. These are determined from the intermediate *meso-scale*, governed by light scattering and the *micro-scale* with heterogeneous local effective thermo-chemo-mechanical properties. These scales are depicted from left to right respectively in Fig. 4.1.

To relate thermo-chemo-mechanical properties on the micro-scale to the macro-scale, two requirements are assumed to hold; i.e. *(i)* the macroscopic domain spans a size much larger than the microscopic domain and *(ii)* the time needed to impose changes at the macro-scale is much larger than the time needed to reach a steady-state at the micro-scale [135]. This implies separation of scales in both space and time. Assuming that individual layers have a clear role in the residual stresses and deformations in the final part, the separation of scales is less pronounced for the meso- to macro-scale. The mathematical description and physical interpretation of the distinct length scales together with the imposed assumptions is addressed in the following Sections 4.2.1 to 4.2.4, starting with the micro-scale. The problems at the individual length scales are solved using tailored finite element formulations.

4.2.1 Microscopic problem formulation

The smallest length scale considered is the micro-scale ($_m$), where the presence of the inclusions inside the conversion dependent monomer-to-polymer matrix is accounted

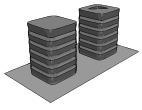

for in a continuum setting, also known as a representative volume element (RVE). Using appropriate scale-transition relations, the micro-scale behavior is translated to effective macro-scale constitutive laws. A total of three physical descriptions with appropriate assumptions are relevant at this RVE scale, i.e. *(i)* the chemical evolution in the matrix material and *(ii)* thermal and *(iii)* mechanical constitutive descriptions of the different constituents. These will be addressed in the following Sections 4.2.1.1 to 4.2.1.3, respectively.

4.2.1.1 Chemical evolution

The micro-scale is considered to be small and of size l, with only a limited number of inclusions contained inside the considered volume. Using this restriction, a convenient assumption is to consider the intensity to be homogeneous throughout the volume. For the case of a homogeneous unfilled resin, this assumption makes perfect sense as long as the depth of light penetration, D_p, is much larger than the microscopic size l, i.e. $l \ll D_p$. Note that formally D_p is the length in thickness direction where the irradiance has reduced to $1/e$ of the initial value that originates from a modified version of the Beer-Lambert law [19, 54]. Requiring that the magnitude of D_p for the filled resin is still $\gg l$, the light intensity at the micro-scale can also be assumed homogeneous, despite of the light scattering in the slurry.

For the description of the polymer conversion, a simple square root intensity dependent monomer conversion is adopted [78]:

$$R_p = -\frac{d[M]}{dt} = \mathcal{P}\sqrt{I}[M], \tag{4.1}$$

where R_p is the rate of polymerization, $[M]$ the monomer concentration, t the time, I the light intensity and $\mathcal{P}$ a lumped rate constant for the polymerization process. The corresponding degree of conversion of the matrix material at the micro-scale p_m is a linear and weighted difference of the current and initial monomer concentration, $[M]$ and $[M]_0$, respectively, formulated as

$$p_m = \frac{[M]_{0,m} - [M]_m}{[M]_{0,m}}. \tag{4.2}$$

4.2.1.2 Thermal behavior

Thermal equilibrium A direct result of the two-scale transition setting introduced above is a simple form of the thermal equilibrium equation inside the micro-scale constituents, both matrix and inclusions, without transient terms, i.e. [135–137]

$$-\vec{\nabla}_m \cdot \vec{q}_m = 0 \quad \text{with} \quad \vec{q}_m = -k_m \vec{\nabla} T_m, \tag{4.3}$$

where $\vec{q}_m$ is the heat flux vector introduced in the form of Fourier's law, in which T_m is the temperature and k_m the thermal conduction coefficient.

Heat source The assumption of an instantaneous steady-state at the micro-scale does not eliminate the possible existence of a heat source term at the macro-scale. In this work, heat generation, $\hat{r}_m$, is restricted to the matrix material. The combined effect of heat generated by photopolymerization and by light absorption is described as [44]:

$$\hat{r}_m = -\Delta H_m \left(\frac{d[M]}{dt} \right)_m + a_m I_m \left[C^* \right]_m. \tag{4.4}$$

The first contribution in $\hat{r}_m$ is attributed to the exothermic heat, with ΔH_m the polymerization heat. The second contribution originates from heat by light absorption, where a_m is the molar absorptivity and $[C^*]_m$ the concentration of the absorbing species. Note that in opaque ceramic inclusions, the last term in Eq. (4.4), i.e. light absorption, can be relevant, but for the alumina particles considered here, the absorption is negligible at the considered wavelength [31].

4.2.1.3 Mechanical constitutive behavior

Requiring the RVE to be in equilibrium and in the absence of body forces—which, compared to the divergence term, induce a negligible (volumetric) contribution due to the small domain size—the divergence term in the balance of linear momentum becomes dominant, which leads to

$$\vec{\nabla}_m \cdot \sigma_m = \vec{0}, \tag{4.5}$$

where σ_m is the micro-scale stress tensor. The relation between the microscopic strains and stresses in both phases follows directly from the isotropic Hooke's law, i.e.

$$\sigma_m = {}^4\boldsymbol{\mathcal{C}}_m : \varepsilon_{e,m} \tag{4.6}$$

where $\varepsilon_{e,m}$ is the elastic strain tensor and ${}^4\boldsymbol{\mathcal{C}}_m$ is the fourth-order elastic stiffness tensor [138] for which the relevant parameters, in this case Young's modulus E and Poisson's ratio ν, are introduced in the following.

Even though the constitutive behavior is assumed to be purely elastic, non-elastic strains and conversion dependent mechanical properties are accounted for. With respect to the former, the total strain tensor $\boldsymbol{\varepsilon}$ is decomposed into an elastic, thermal and chemical component, according to

$$\boldsymbol{\varepsilon}_m = \boldsymbol{\varepsilon}_{e,m} + \boldsymbol{\varepsilon}_{th,m} + \boldsymbol{\varepsilon}_{ch,m}, \tag{4.7}$$

respectively. For the inclusion material, the chemical strain is equal to zero and the total strain in Eq. (4.7) reduces to the first two terms, i.e. elastic and thermal strain. The thermal component in both constituents, i.e. matrix and inclusions, follows the classical description for thermal expansion in an isotropic form, i.e.

$$\boldsymbol{\varepsilon}_{th,m} = \upsilon_m \left(T_m - T_{ref,m} \right) I, \tag{4.8}$$

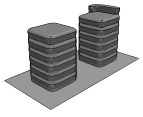

with υ_m the thermal expansion coefficient, $T_{\mathrm{ref},m}$ a reference temperature and I the unity tensor. The chemical strain in the resin is assumed to be linearly related to the degree of conversion using the shrinkage strain at maximum conversion as a scaling factor [78]:

$$\varepsilon_{\mathrm{ch},m} = p_m \varepsilon_{\mathrm{ch,max},m} I. \tag{4.9}$$

The inclusion properties are assumed constant at the micro-scale, however, solidification in the matrix material is accounted for by introduction of a conversion-dependent Young's modulus E_{p} that reads [78]

$$\begin{aligned} E_{\mathrm{p},m}(p_m) &= e_0 E_{\mathrm{pol}} && \text{for } p_m < p_{\mathrm{gel}}, \\ E_{\mathrm{p},m}(p_m) &= \left(\frac{1-e_0}{1-p_{\mathrm{gel}}} \left(p_m - p_{\mathrm{gel}} \right) + e_0 \right) E_{\mathrm{pol}} && \text{for } p_m \geq p_{\mathrm{gel}}. \end{aligned} \tag{4.10}$$

Initially when the resin is in a monomeric phase the mechanical properties are insignificant as ensured by multiplication with $e_0 \ll 1$. After the gel-point, p_{gel}, is reached and solidification initiates, the Young's modulus starts to increase linearly with increasing conversion to a value of E_{pol} for fully polymerized material.

4.2.2 *Mesoscopic problem formulation*

The meso-scale ($\mathcal{M}$) is introduced to account for the effect of the particles on the light intensity profile. Whereas knowledge of the light source intensity profile and the resin's penetration depth D_p is sufficient to predict the cured profile in a traditional unfilled polymer resin using Beer-Lambert's law [54], this is no longer the case in filled media [31].

Due to the high filling volume fraction and the small difference between the light wavelength and particle sizes, an electromagnetic wave description of light is used through Maxwell's equations. Considering that illumination times are much longer than the time required for light to travel through a layer, the time-dependent light propagation is not of interest and the problem is solved in the frequency domain [78]. A form of the Maxwell curl-curl equation for the electric field that holds for dielectric materials can be formulated as [95]

$$\vec{\nabla}_{\mathcal{M}} \times \left(\vec{\nabla}_{\mathcal{M}} \times \vec{E}_{\mathcal{M}} \right) = \zeta_0^2 \tilde{n}_{\mathcal{M}}^2 \vec{E}_{\mathcal{M}}, \tag{4.11}$$

where $\vec{E}_{\mathcal{M}}$ is the electric field, ζ_0 the light wave number in free space and $\tilde{n}_{\mathcal{M}}$ the complex refractive index which is a function of the refractive index $n_{\mathcal{M}}$ and the extinction coefficient $\kappa_{\mathcal{M}}$:

$$\tilde{n}_{\mathcal{M}} \equiv n_{\mathcal{M}} - i\kappa_{\mathcal{M}}. \tag{4.12}$$

The mesoscale problem description is completed by appropriate boundary conditions as addressed in Ref. [116]. These ensure that the light source enters the domain via the

top surface (cf. Fig. 4.1) and they account for the finite domain dimensions through a perfectly matched layer (PML) on the lateral and bottom faces.

The intensity of the light that induces the photopolymerization process is obtained from the wave solution through the magnitude of the time averaged Poynting vector $\vec{S}$:

$$I_{\mathcal{M}} = \|\langle \vec{S}_{\mathcal{M}} \rangle\| = \left\| \frac{1}{2} \Re \left\{ \vec{E}_{\mathcal{M}} \times \vec{H}^*_{\mathcal{M}} \right\} \right\|, \tag{4.13}$$

where $\vec{H}^*_{\mathcal{M}}$ is the complex conjugate of the magnetic field, obtained using Faraday's law.

4.2.3 *Macroscopic problem formulation*

At the macro-scale ($_M$), the focus lies in capturing the influence of VP process conditions, with respect to e.g., layer thickness and illumination conditions to name a few. Relevant balance equations at this scale are mechanical and thermal equilibrium.

The mechanical linear momentum balance at the macro-scale becomes

$$\vec{\nabla}_M \cdot \sigma_M + \rho_M \vec{b}_M = \vec{0}, \tag{4.14}$$

where dynamic contributions are ignored and $\vec{b}_M$ is the body force vector per unit volume and ρ_M the mass density. The thermal equilibrium equation with transient effects and a heat source term is formulated as

$$\left(\rho c_p\right)_M \frac{dT_M}{dt} = \vec{\nabla}_M \cdot \left(k_M \vec{\nabla} T_M \right) + \hat{r}_M, \tag{4.15}$$

where c_p is the specific heat and Fourier's law is substituted for $\vec{q}$.

Mechanical and thermal boundary conditions, on a domain as illustrated in Fig. 4.2 for four individual time steps, complete the macro-scale formulation. For the mechanical boundary conditions, a simple displacement (Dirichlet) constraint ($\Delta\vec{x} = 0$) suffices in the AM process, i.e. a perfect bonding is considered at the interface between the base-plate of the printer and the first slurry layer at t_0. Assuming that the top and the sides

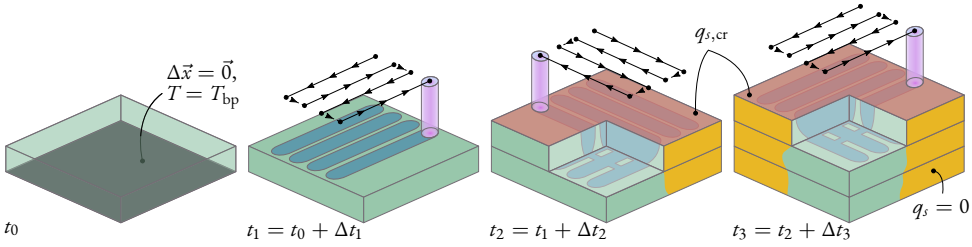

Figure 4.2 Visualization of the macro-scale description. The continuous expansion of the domain in an AM process simulation is indicated for four time steps, starting with the layer deposition at t_0, illumination of the first layer at t_1 and two subsequent layers at t_2 and t_3.

are free to deform makes sense considering only a limited section of the whole fluid vat. The temperature is also fixed at the base-plate at the temperature T_{bp}, where it is mechanically connected. A thermal interaction with the surroundings is accounted for by a combination of convection and radiation on the top surface. This defines a Neumann surface heat flux formulated as [139]

$$q_{s,\text{cr}} = h\left(T - T_e\right) + \mathfrak{e}\mathcal{S}\left(T^4 - T_e^4\right), \tag{4.16}$$

in which h is the convective heat transfer coefficient, $\mathfrak{e}$ the emissivity, $\mathcal{S}$ the Stefan-Boltzmann constant and T_e the surrounding environmental temperature. A no-flux thermal condition is assumed on the side faces of the domain such that there is no thermal gradient in the direction perpendicular to the plane. This assumption is justified as long as the total temperature increase (near the boundaries) remains limited and/or the surface area on the sides is small compared to the top and bottom surface.

Another element that Fig. 4.2 highlights is the additional complexity added by the additive nature of the process. Not only does the domain-size increase from layer-to-layer, also the boundaries change, and, as such, the boundary conditions do as well. This important issue will be further addressed in Section 4.4.1.

4.2.4 Coupling between the scales

To provide the scale-transition relations from micro-to-macro and meso-to-macro, a first-order and offline homogenization scheme is applied. In the current approach, offline implies that homogenized effective properties on the macro-scale are first determined from the scale-transition relationships before conducting the analysis at the component scale. A coupling between the micro- and meso-scale is not considered in the present framework. It is assumed that the change in the (effective) light scattering as a result of polymer conversion and related effects, e.g., shrinkage, photobleaching and changing of the refractive index is insignificant. This implies that the micro-scale evolution does not affect the meso-scale, enabling application of the offline homogenization scheme and greatly increasing computational efficiency. For an extensive motivation behind the latter the reader is referred to Ref. [78].

4.2.4.1 Micro-to-macro

The scale transition for the thermomechanical micro-to-macro problem is well documented in literature, see e.g., Refs. [135–137, 140]. Mechanically, micro-macro consistency is obtained through the classical Hill-Mandel condition which is enforced by application of periodic boundary conditions on the micro-level RVE. This ensures consistency in internal virtual work between both scales. If an RVE is considered with quantities on opposite faces denoted with a $+$ and $-$ superscript, the mechanical

periodic boundary conditions are given by

$$\vec{u}_m^+ = \vec{u}_m^- + \varepsilon_M \cdot [\vec{x}_m^+ - \vec{x}_m^-], \tag{4.17}$$
$$\vec{t}_m^+ = -\vec{t}_m^-, \tag{4.18}$$

where $\vec{x}$ denotes the reference position and $\vec{u}$ and $\vec{t}$ the boundary displacement and traction, respectively.

A similar approach also provides a thermal scale-relation that originates from the second law of thermodynamics, which ensures consistency in entropy due to heat conduction [141]. The corresponding periodic boundary conditions are

$$T_m^+ = T_m^- + \vec{\nabla} T_M \cdot [\vec{x}_m^+ - \vec{x}_m^-], \tag{4.19}$$
$$\vec{q}_m^+ \cdot \vec{n}^+ = -\vec{q}_m^- \cdot \vec{n}^- \tag{4.20}$$

with $\vec{q}$ the heat flux vector and $\vec{n}$ the unit normal to the surface.

In the first-order computational homogenization scheme considered here, the macroscopic gradients of the displacement field and temperature field are equal to the volume average of the microscopic fields, through

$$\sigma_M = \frac{1}{V_m} \int_{V_m} \sigma_m \, dV_m, \tag{4.21}$$
$$\vec{q}_M = \frac{1}{V_m} \int_{V_m} \vec{q}_m \, dV_m. \tag{4.22}$$

Other volumetric quantities follow a similar volume averaging approach, such that [137, 140]

$$\rho_M = \frac{1}{V_m} \int_{V_m} \rho_m \, dV_m, \tag{4.23}$$
$$\hat{r}_M = \frac{1}{V_m} \int_{V_m} \hat{r}_m \, dV_m, \tag{4.24}$$
$$(\rho c_p)_M = \frac{1}{V_m} \int_{V_m} (\rho c_p)_m \, dV_m. \tag{4.25}$$

4.2.4.2 Meso-to-macro

While the micro-to-macro transition is based on a strong scale-separation, this is not the case for the meso-to-macro relation, as the light penetration depth typically surpasses a layer thickness. The meso-to-macro scale transition is only a method to eliminate the dependence on the micro-structural (spatial) realization with respect to light scattering. Even though previous works showed that the illumination conditions on the micro-scale can be highly inhomogeneous locally, at the macro-scale only the resulting cure profile is of interest [78, 116].

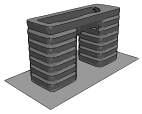

The homogenization approach used in this work is inspired by the experimental approach in Ref. [76], where a known light penetration in an unfilled resin is scaled by a beam width and depth that are corrected for the presence of powder particles. In the current work, the broadening and shallowing, as illustrated in Fig. 4.3, is predicted through numerical simulation.

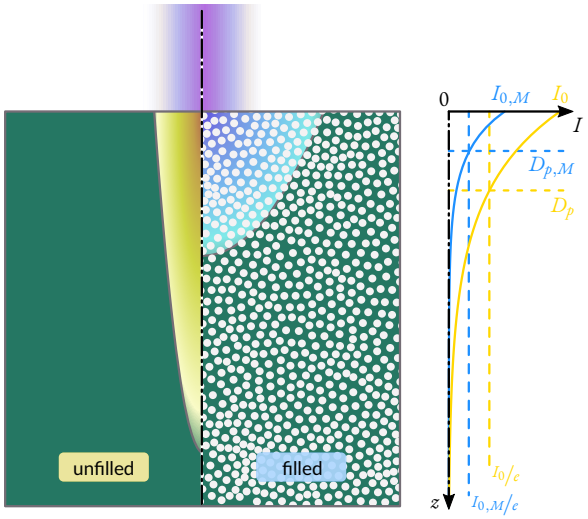

Figure 4.3 Graphical description of the meso- to macro-scale transition for an unfilled versus a filled resin. The line plot on the right illustrates the intensity profile on the line through the horizontal center of the Gaussian laser beam for both the unfilled (yellow) and filled (blue) resin. Light scattering in the filled resin causes a change in apparent intensity, beam width and depth of penetration, whilst conserving laser power.

Using an apparent penetration depth, laser beam radius and intensity present in the slurry, $D_{p,M}$, $w_{0,M}$ and $I_{0,M}$, respectively, the spatial intensity profile induced by the Gaussian laser is assumed to be given by

$$I_M(x,z) = I_{0,M} e^{-2x^2/{w_{0,M}}^2} e^{-z/D_{p,M}}, \tag{4.26}$$

where x and z are the horizontal and vertical direction, respectively. The slurry dependent values will also be compared to values in the homogeneous resin without the alumina filler, i.e. I_0, D_p and w_0, cf. the left hand side of Fig. 4.3. Note that the apparent intensity $I_{0,M}$ is introduced to conserve laser input power, P_L, and as such is related to the beam width according to

$$I_{0,M} = \sqrt{\frac{2}{\pi}} \frac{P_L}{w_{0,M}}. \tag{4.27}$$

In order to transform the local meso-scale intensity field $I_{\mathcal{M}}(x,z)$ to the macro-scale homogenized mathematical form $I_M(x,z)$ in Eq. (4.26), a two-step approach is applied where the surface intensity profile is extracted first and the corresponding penetration depth is determined next. For the considered alumina slurry, this process is illustrated in Section 4.3.1.

In order to conserve the effective conversion through the scale-transition, the volume averaged meso- and macro-scale degree of conversion should be identical. Formally, that implies

$$\int_{V_M} p_M\left(I_M(\vec{x}),t\right) dV = \int_{V_{\mathcal{M}}} p_{\mathcal{M}}\left(I_{\mathcal{M}}(\vec{x}),t\right) dV. \tag{4.28}$$

To ensure that Eq. (4.28) still holds after the homogenization, the conversion description is scaled by introduction of a dimensionless scaling parameter $\mathcal{B}$ and a scaled power n. The macro-scale photopolymerization law, cf. Eq. (4.1), consequently becomes

$$R_{p,M} = -\left(\frac{d[M]}{dt}\right)_M = \mathcal{P}\mathcal{B}\sqrt{I_M(\vec{x})}\left(\frac{I_M(\vec{x})}{I_{0,M}}\right)^n [M]_M. \tag{4.29}$$

To enforce conversion conservation in an effective sense, $\mathcal{B}$ and n are determined by ensuring

$$\frac{1}{V_M}\int p_M\left(I_M(\vec{x}),\mathcal{B},n,t\right) dV - \frac{1}{V_{\mathcal{M}}}\int p_{\mathcal{M}}\left(I_{\mathcal{M}}(\vec{x}),t\right) dV \to 0 \quad \forall\, t, \tag{4.30}$$

such that the difference between macroscopic and mesoscopic domain averaged conversion for all time steps approaches zero. This can also be written as a least squares minimization problem:

$$\min_{\mathcal{B},n} \sum_{t=0}^{t_e} \left(\langle p_M\rangle - \langle p_{\mathcal{M}}\rangle\right)^2, \tag{4.31}$$

where $\langle p\rangle$ denotes the volume averaged conversion and the sum is taken over a discrete number of time-steps $t = 0, \Delta t, \ldots, t_e$. Note that this does not change the conversion kinetics, it simply ensures the correct macro-scale conversion evolution. Additionally, it is useful to realize that although this explicitly only enforces temporal agreement, implicitly, due to the time integrated effect of conversion, the conversion profile will also be captured correctly. This approach is further elaborated in Section 4.3.2.

4.3 Effective property determination

The scale-transition relations introduced in the previous section enable the extraction of effective properties to be used in the solution of the macroscopic problem. In the following, the effective illumination and chemo-thermo-mechanical properties are derived for the photo-reactive alumina slurry, but the approach described in Section 4.2 is generic and can in principle be applied to different filled resin systems as well.

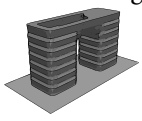

4.3.1 *Effective scattering properties*

The presence of the inclusions causes light scattering to occur, which broadens the apparent laser beam width, typically reducing the penetration depth. To quantify this effect, a penetration depth $D_{p,M}$, beam width $w_{0,M}$ and light intensity $I_{0,M}$ (which is related to $w_{0,M}$ through Eq. (4.27), cf. Fig. 4.3), characterizing the filled medium need to be identified.

For the alumina filler in the monomer/polymer resin at hand, the light propagation through the material is dominated by the difference in optical properties in the complex refractive index $\tilde{n}$, cf. Eq. (4.11). The micro-scale optical properties used for the resin and spherical inclusions with a constant radius are given in Table 4.1. Note that the extinction coefficient κ in Eq. (4.12) is related to the penetration depth D_p through:

$$\kappa = \frac{\alpha\lambda}{4\pi} = \frac{\ln(10)a[C^*]\,\lambda}{4\pi} = \frac{\left(D_p\right)^{-1}\lambda}{4\pi}, \tag{4.32}$$

where λ is the wavelength of the light and α is the absorption/attenuation coefficient [78, 95–97]. Due to the presence of the initiator, which is assumed to be the only absorbing species inside the resin, i.e. $[C^*] = [In]_0$, the resin's absorption is clearly non-zero. At the wavelength of interest the alumina absorption is negligible [31].

The light scattering problem is solved using Comsol's RF module [94] in a two-dimensional finite element setting. The third dimension is ommited in order to reduce the computational cost, which can be attributed to the required resolution to fully resolve the wavelength of light [78]. Motivation can however also be found in the equivalent light scattering efficiency for two- and equivalent three-dimensional shapes [116]. To translate the three-dimensional alumina volume fraction to an equivalent two-dimensional filling fraction, the path length of the light through and from-particle-to-particle is required to be identical. Furthermore, the inclusion's

Table 4.1: Optical properties of the micro/meso-scale constituents and boundary conditions.

Parameter	Value	Unit	Description
n_p	1.5	[-]	Monomer/polymer refractive index
$[In]_0$	1	[mol/L]	Initial initiator concentration
a_{In}	150	[L/(mol cm)]	Molar absorptivity initiator
n_i	1.78	[-]	Alumina refractive index
κ_i	0	[-]	Alumina extinction coefficient
r_i	0.5	[µm]	Alumina inclusion radius
φ_i	0.5	[-]	Alumina volume fraction
I_0	500	[W/m^2]	Source peak light intensity
w_0	6	[µm]	Laser beam width
λ_0	400	[nm]	Light source wavelength

curvature is considered highly relevant for the scattered result [116]. Correspondingly, the two dimensional filling fraction and inclusion radius are taken equal to the three-dimensional values.

The considered square domain with a filling fraction of 50% consists of 1000 circular inclusions, which in turn dictates the length of the domain edges, see the example domain shown in Fig. 4.4 (a). Particles are placed in a periodic arrangement at the left and right boundaries, but they do not cross the top and bottom boundary to account for the free illumination surface at the top.

An example light scattering result is illustrated in Fig. 4.4 (b) for the single realization depicted in Fig. 4.4 (a). Individual particles are not displayed to clearly show the

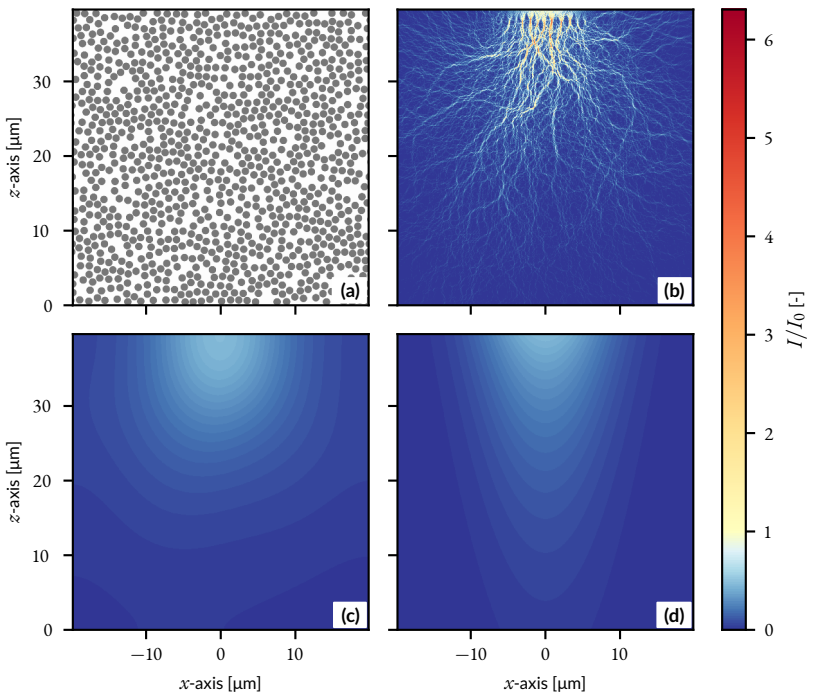

Figure 4.4 Graphical visualization of the homogenization approach for the particle realization depicted in *(a)*. The original scattered intensity field is displayed in *(b)*, after application of the Gaussian smoothing in *(c)* and the corresponding parameterized version that follows Eq. (4.26) in *(d)*.

calculated field information. The color in the plot denotes the intensity field normalized by the source intensity I_0. The non-vertical intensity lines in the inhomogeneous intensity field clearly illustrate the broadening of the light penetration. The subsequent homogenization approach is visualized in Figs. 4.4 (c–d). In Fig. 4.4 (c), an energy conserving Gaussian smoothing is applied to the original intensity field. The magnitude of the Gaussian smoothing, i.e. the standard deviation in the blur operation, is optimized

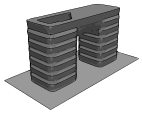

such that the best match is obtained at the top surface ($z = 0$) with a modified set of power conserving source parameters, according to Eq. (4.27). This nested (least squares) optimization, that results in the smeared intensity field in Fig. 4.4 (c), provides the effective Gaussian laser parameters $I_{0,M}$ and $w_{0,M}$, cf. Eq. (4.26). The remaining parameter in this equation, D_p, is subsequently obtained from a minimization of the difference between the Gaussian smeared field in Fig. 4.4 (c) and the parameterized version in Fig. 4.4 (d). Figs. 4.4 (b–c) indicate that the light scattering concentrates the light slightly below the resin surface. The resulting parameterized field displayed in Fig. 4.4 (d) neglects this behavior, but overall remains consistent.

The homogenized effective values for $D_{p,M}$ and $I_{0,M}$ are obtained as the average from 20 different geometrical realizations. The resulting normalized parameter values are displayed in Table 4.2 with their corresponding standard deviation (SD). The

Table 4.2: Normalized effective optical properties at the macro-scale.

Parameter	Value	SD	Unit
$I_{0,M}/I_0$	0.485	0.017	[-]
$D_{p,M}/D_p$	0.546	$2.6 \cdot 10^{-2}$	[-]

magnitude of the normalized values illustrates that for the considered slurry both the depth of penetration and the apparent intensity are roughly two times lower compared to the unfilled resin. Based on Eq. (4.27), the corresponding apparent beam width is approximately twice as wide compared to the actual one. The result for the apparent light source intensity, that approximately equals half the source intensity, closely matches the experimental result obtained by Li et al. [142].

4.3.2 *Effective conversion properties*

Even though the homogenized intensity field introduced in the previous section captures the averaged intensity field quite accurately, the highly inhomogeneous field characteristics are lost. Because the relation with the conversion is non-linear, this could affect the conversion efficiency. To remedy this, the conversion scaling parameter $\mathcal{B}$ and modified power n from Eq. (4.29) are determined here. This analysis is conducted using the properties denoted in Table 4.3. The mean and the 95% confidence interval of the volume averaged meso-scale conversion evolution for the 20 considered geometrical realizations i, $\langle p_{i,\mathcal{M}} \rangle$, is shown in Fig. 4.5. For every geometrical realization, the

Table 4.3: Optical properties of the micro/meso-scale constituents and boundary conditions.

Parameter	Value	Unit	Description
$[\mathcal{M}]_0$	8.2	[mol/L]	Initial monomer concentration
$\mathcal{P}$	0.15	$[\mathrm{m}/(\mathrm{s}\mathrm{W}^{\frac{1}{2}})]$	Polymerization rate constant

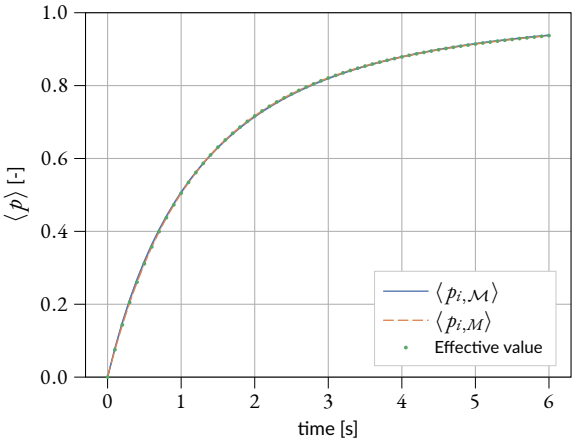

Figure 4.5 Domain averaged conversion in the original scattered (solid) and parameterized (dashed) fields, i.e. $\langle p_{i,\mathcal{M}} \rangle$ and $\langle p_{i,M} \rangle$, respectively, with mean and 95% confidence interval for 20 geometrical realizations. $\langle p_{i,M} \rangle$ is a direct solution of the minimization problem in Eq. (4.31) following Eq. (4.29) with $\mathcal{B}_i$ and n_i. The homogenized effective value (dotted) uses the effective conversion properties from Table 4.4.

corresponding optimized effective $\mathcal{B}_i$ and n_i parameter are determined, according to the minimization problem in Eq. (4.31) with $\Delta t = 0.1\,\mathrm{s}$ and $t_e = 6\,\mathrm{s}$. The resulting mean and the 95% confidence interval of the volume averaged macro-scale conversion evolution, $\langle p_{i,M} \rangle$, is also indicated in Fig. 4.5. Although the variation between the 20 geometrical realizations has been incorporated in Fig. 4.5 in the form of a confidence interval band around the mean for both $\langle p_{i,\mathcal{M}} \rangle$ and $\langle p_{i,M} \rangle$, it is hardly wider than the line thickness itself and therefore considered insignificant. Subsequently, the mean of $\mathcal{B}_i$ for all geometrical realizations (i) provides the effective parameter $\mathcal{B}$, whereas the non-linear value of n is obtained by a least-squares difference minimization to $\langle p_{i,\mathcal{M}} \rangle$ for all i. Resulting values are provided in Table 4.4 and the corresponding volume averaged response is shown by the dotted line in Fig. 4.5. The latter shows that the proposed scaling of the conversion laws facilitates conservation of the photopolymerization efficiency through the scale-transition.

The resulting conversion field over time is illustrated in Fig. 4.6 for intermediate time steps, together with the conversion evolution of a single realization that serves as an

Table 4.4: Normalized effective conversion properties at the macro-scale.

Parameter	Value	SD	Unit
$\mathcal{B}$	0.873	$3.22 \cdot 10^{-2}$	[-]
n	−0.120	n.a.	[-]

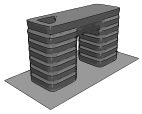

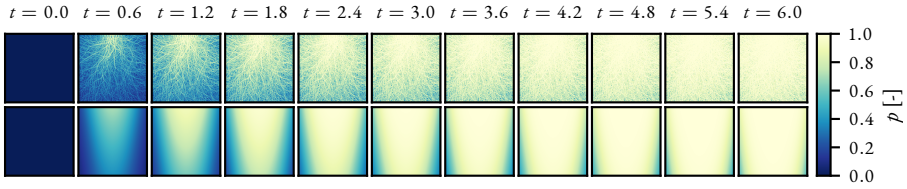

Figure 4.6 Conversion over time [s] for a single realization (top row) compared to the homogenized conversion induced by the homogenized intensity (bottom row), i.e. using effective properties from Tables 4.2 and 4.4.

example.

4.3.3 *Effective mechanical properties*

In this subsection, effective mechanical properties are derived in terms of the effective stiffness, thermal expansion and chemical shrinkage tensor. To this extent a total of 20 unique microstructures are generated using the discrete element package LIGGGHTS [143]. To respect scale-separation, the considered micro-scale domains consist of 10 alumina inclusions with $r = 0.5$ µm, occupying a volume fraction $\varphi = 0.5$. Three example realizations are visualized in Fig. 4.7. Proper dispersion of the inclusion in the matrix material is ensured by first filling the domain to 64 vol.%, before reducing the radius to the specified value.

Effective properties are obtained using Comsol 5.4 [144] by application of periodic boundary conditions and using the constituents' material properties denoted in Table 4.5, at constant temperature and curing degree. The only variable assumed conversion dependent is the polymer Young's modulus, as described by Eq. (4.10).

The resulting effective stiffness, thermal expansion and chemical shrinkage can be characterized as isotropic, as shown in Appendix B. The complete set of obtained effective elastic properties is provided in Table 4.6, with the exception of the volume averaged quantity ρ_M which follows directly from Eq. (4.23). The standard deviation shows the limited spread between the different geometrical realizations.

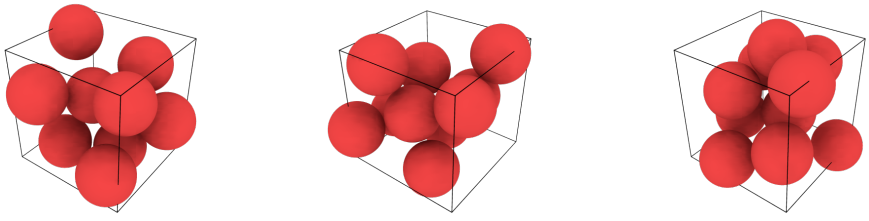

Figure 4.7 Three different realizations of a micro-structure with $r = 0.5$ µm and $\varphi = 0.5$.

Table 4.5: Mechanical properties of the constituents at the micro-scale.

Parameter	Value	Unit	Description
E_p	$2 \cdot 10^9$	[Pa]	Polymer Young's modulus at $p = 1$
e_0	$1 \cdot 10^{-3}$	[-]	Unpolymerized stiffness factor
p_gel	0.2	[-]	Gel-point for conversion
ν_p	0.4	[-]	Polymer Poisson's ratio
$\varepsilon_\mathrm{ch,max}$	-0.05	[-]	Maximum shrinkage strain at $p = 1$
υ_p	$280 \cdot 10^{-6}$	[1/K]	Polymer coeff. of thermal expansion
ρ_p	1150	[kg/m^3]	Polymer density
E_i	$300 \cdot 10^9$	[Pa]	Alumina Young's modulus
ν_i	0.22	[-]	Alumina Poisson's ratio
υ_i	$8 \cdot 10^{-6}$	[1/K]	Alumina coeff. of thermal expansion
ρ_i	3900	[kg/m^3]	Alumina density

Table 4.6: Effective mechanical properties at the macro-scale.

Parameter	Value	SD	Unit
E_M	8.90	0.291	[GPa]
$e_{0,M}$	$1.06 \cdot 10^{-3}$	$3.63 \cdot 10^{-5}$	[-]
ν_M	0.32	$6.67 \cdot 10^{-3}$	[-]
$\varepsilon_{\mathrm{ch,max},M}$	-0.02	$1.49 \cdot 10^{-3}$	[-]
υ_M	$117 \cdot 10^{-6}$	$8.10 \cdot 10^{-6}$	[1/K]

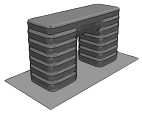

4.3.4 Thermal properties

The same geometrical realizations used for the effective mechanical property determination in Section 4.3.3 (cf. Fig. 4.7) are also used for thermal properties. Apart from the thermal conduction k, all thermal characteristics are obtained by volume averaging following Eqs. (4.24) and (4.25). As with the mechanical properties, the constituents' properties are assumed isotropic at the micro-scale, as given in Table 4.7.

Table 4.7: Thermal properties of the constituents at the micro-scale.

Parameter	Value	Unit	Description
$c_{p,\mathrm{p}}$	1700	[J/(kg K)]	Polymer heat capacity
k_{p}	0.26	[W/(m K)]	Polymer thermal conductivity
ΔH_p	$5.48 \cdot 10^4$	[J/mol]	Polymerization heat
$c_{p,\mathrm{i}}$	900	[J/(kg K)]	Alumina heat capacity
k_{i}	27	[W/(m K)]	Alumina thermal conductivity

The effective conductivity is obtained by applying periodic boundary conditions with a temperature gradient and, subsequently, measuring the resulting heat flux as introduced in Section 4.2.4.1. The determined isotropic thermal conductivity is provided in Table 4.8, cf. Appendix B for the spread in individual realizations.

Table 4.8: Effective thermal properties at the macro-scale.

Parameter	Value	SD	Unit
k_M	1.14	$3.86 \cdot 10^{-2}$	[W/(m K)]

4.4 AM process simulation

To illustrate the relevance of the above homogenization procedure for the simulation of the additive manufacturing process at the macro-scale, the proposed framework is implemented into an in-house developed finite element code. Details of this implementation will be addressed next, after which the applicability of the macro-scale model formulation with the homogenized input is demonstrated.

4.4.1 Implementation of the process simulation framework

For simulating a section of the photopolymerization vat, a layer of slurry is deposited in the form of a voxel mesh with a certain resolution [133]. To fully resolve the penetration depth, the current implementation uses a uniform mesh size with multiple elements per layer thickness. New bulk elements are only added once a new slurry layer is applied.

Initially, the top nodes of the added elements are placed at the intended position, based on the undeformed and as-intended layer. To ensure this initial state is stress free, the initial strains upon activation are subtracted from the element strains in Eq. (4.7) to obtain an updated total strain formulation [133].

The top surface of the domain consists of surface elements to account for the convection and radiation boundary conditions, cf. the red surface in Fig. 4.2. As soon as a new layer is added, the previous surface elements are removed.

The driving force for all physics of interest is the light intensity, which is considered as a volumetric field quantity according to an axisymmetric modification of Eq. (4.26). Movement of the laser (along with the addition of new layers) is driven by a G-code script, which is here generated by the open-source Slic3r software [145]. As soon as the process is completed, the part is removed from the base plate by removing the associated mechanical constraints [133].

4.4.2 Sample bridge process simulation

The macro-scale framework is applied to simulate a 9-layer bridge sample as depicted in Fig. 4.8. The complete dimensions are $(x \times y \times z)$ $200 \times 600 \times 450$ µm with two square pillars. To prevent AM/VP related geometrical inaccuracies induced by slicing the three-dimensional object, the pillars and the deck consist of exactly 6 and 3 layers of 50 µm thick, respectively, and faces are considered flat and either parallel or perpendicular to the printing direction. Temperatures of the constrained printer base-plate and the surrounding environment are set to 20 °C, while the convection and emissivity coefficients are assumed to be 10 $\mathrm{W/m^2K}$ and 0.9, respectively. To discretize

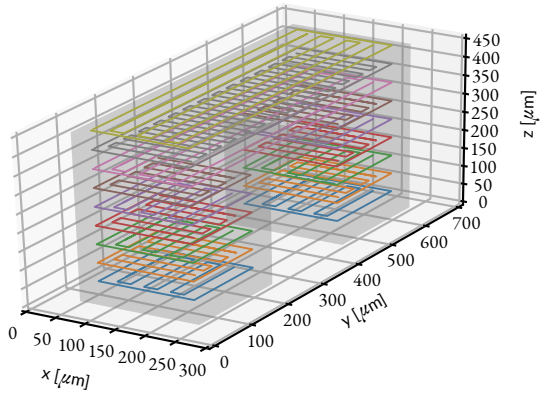

Figure 4.8 Graphical visualization the bridge shaped showcase. The part consists of 9-layers out of which 6 constitute the two pillars and 3 the bridge deck, for which the laser scan patterns are visualized by the lines. Irradiation of each feature, i.e. pillar or deck, starts with the contour after which the infill is scanned at an alternating 0/90 degree angle, as controlled by the G-code input script.

the domain, five linear cube elements are placed over the layer thickness, δ, which is 50 µm. Based on the effective irradiation properties extracted from the meso-scale and a laser speed of 30 µm/s, the cured-line width, C_w, is expected to be 40 µm. Accordingly, the distance between the scanned contour profile and the outer part dimensions is equal to $C_w/2$. After the contour is scanned, the infill of the part is solidified using an alternating 0/90 degree angle inside the *xy*-plane where the line spacing is reduced to 20 µm to ensure proper solidification. Both the contour and the infill strategy are depicted by the lines in Fig. 4.8, where each color designates a single layer.

Resulting fields for degree of conversion, temperature, stress and deformation for intermediate time steps during this process simulation are provided in Fig. 4.9. The

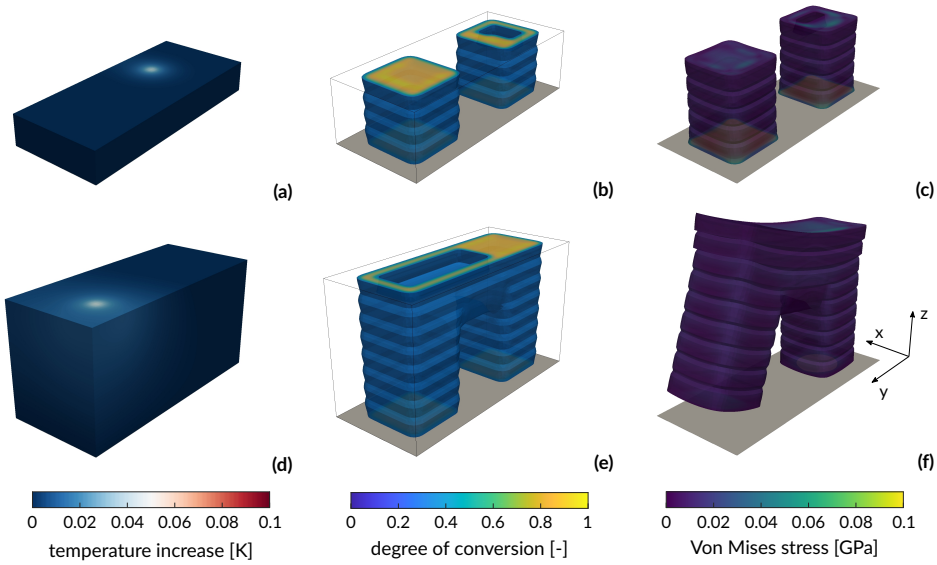

Figure 4.9 Temperature, degree of conversion and Von Mises stress in different time steps throughout the printing process. Temperature (*a*, *d*) is shown in the computational domain. The degree of conversion (*b*, *e*) and the Von Mises stress (*c*, *f*) are displayed in the solidified ($p \geq p_{\text{gel}}$) volume. Deformations depicted in the Von Mises plot are magnified by a factor of 5.

temperature plots show the entire considered section of the slurry bath, while the degree of conversion as well as the Von Mises stress are only shown for the solidified volume with $p > p_{\text{gel}}$. Depicted deformations are multiplied by a factor of 5.

The thermal profile in Figs. 4.9 (a) and (d) immediately shows that, even though the heat generation might be significant, cf. [78], the vat surrounding the laser heat source and the base plate act as a heat-sink and ensure that the part does not overheat during printing. Correspondingly, the temperature increase induced by the exothermic and absorption heat generation is only occurring locally. This is something that might change

for a more voluminous part but could also point to the dominance of the constraint base-plate temperature. However, for the small volume considered and the limited energy input at the considered speed, the assumption of the constrained base-plate temperature is deemed appropriate.

The solidified profiles in Figs. 4.9 (b) and (e) clearly illustrate the geometrical smoothing over individual layers of VP as an AM process, since no clear crevice can be distinguished between layers along the edge of the part. This smoothing, introduced by the required print-through into the previous layer does show in clear undulations on the sides of the object. Furthermore, the conversion field shows that the current scanning speed does not result in fully cured samples and post curing might be required.

A large build-up of stress is evident in Fig. 4.9 (c) where the part is connected to the build-plate. After the part is printed and released from the build-plate this stress largely relaxes, as depicted in Fig. 4.9 (f). The latter also clearly indicates the expected residual deformation from a multi-layer additively manufactured bridge.

A highly resolved cube mesh is to a large extent limiting the feasibility of simulations at a component scale. The possibility to obtain a nearly equivalent accuracy with a course discretization is therefore important to explore. The mesh dependence of the obtained geometry and deformation is shown in Fig. 4.10. It displays the outline of the geometry

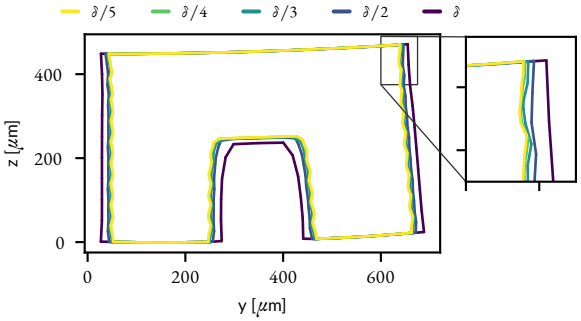

Figure 4.10 Visualization of the deformed outline cross section (deformation at true scale) through the middle of the part ($x = 150$ µm) after release from the base plate, for different element sizes L_e in comparison to the layer thickness $\partial = 50$ µm. From light to dark line colors $L_e = \partial/5, \partial/4, \partial/3, \partial/2, \partial$, respectively.

in a cross-section in the yz-plane through $x = 150$ µm for element sizes L_e that are an increasing fraction of the layer thickness, ∂, i.e. $L_e = \partial/5, \partial/4, \partial/3, \partial/2, \partial$. Fig. 4.10 shows that all different mesh sizes are well capable of capturing the overall deformation, i.e. the warpage of the bridge. To confirm this graphical impression, the curvature of the bridge deck for different mesh resolutions, which is on average equal to 1.2 cm^{-1}, only has a standard deviation of $6.2 \cdot 16^{-3}$ cm^{-1}. For the solidified shape in the horizontal direction, a single element appears to over-predict the dimension of the solidified geometry, while two or more elements already show an adequate agreement.

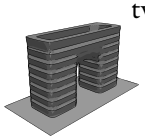

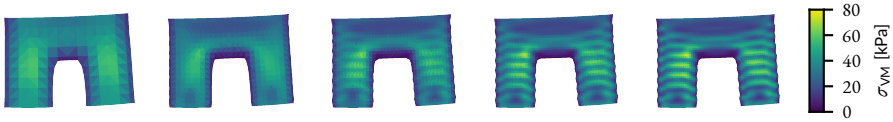

Figure 4.11 Visualization (triangulated) of the Von Mises stress magnitude, σ_{VM} in the middle of the part ($x = 150$ µm) for different element sizes L_e for a layer thickness $\delta = 50$ µm. From left to right $L_e = \delta, \delta/2, \delta/3, \delta/4, \delta/5$, respectively.

The cross-sectional stresses for the different mesh resolutions are provided in Fig. 4.11. For a large resolution in the stress field, a highly resolved mesh is also required. However, if one is only interested in the locations where the largest stress concentrations occur even one or two (linear) elements suffice. It should be noticed that for the magnitude of the stresses and deformations, the relevance of viscous or even plastic material behavior needs to be further examined. The mesh resolution dependency will also change for higher-order elements.

For reference, Figs. 4.12a and 4.12b compare the printed geometry to the intended geometry, both visually and quantitatively, respectively. The most obvious difference is

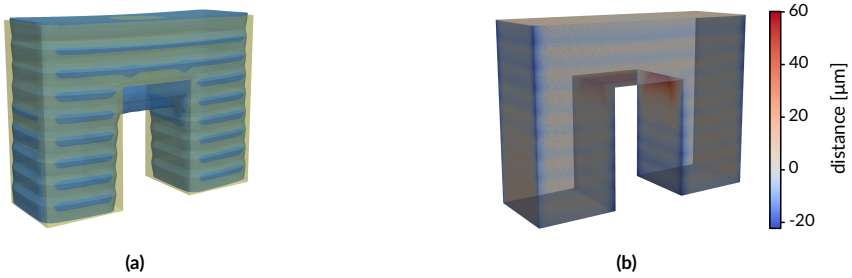

Figure 4.12 Comparison of the printed geometry with $L_e = \delta/5$ (after release from the base plate) to the intended geometry. A purely visual comparison between the intended (yellow) and printed (blue) geometry is provided in (a), while (b) includes the distance from the intended geometry (as displayed) to the printed part.

the large print-through error that can be observed in the additional solidified material underneath the bridge deck. Fig. 4.12b, generated using the open-source software CloudCompare [146], indicates that the additional solidified volume is even more than a single layer thickness. Furthermore, the shrinkage in the bridge deck causes the top to be more narrow than intended, while the deformation in the pillars produces a wider bottom part. Overall, the accuracy in the *xy*-plane is fairly accurate.

The process simulation, based on the homogenized optical, chemical, thermal and mechanical properties of the ceramic-filled resin described above, adequately captures the essential aspects of the multi-physical and multi-scale process in a convenient fashion. Using a limited resolution, it could serve to optimize light path planning or shape modification in an optimization framework to reduce geometrical deviations or

stress concentrations. Note that in spite of the fact that smaller length scales have been eliminated in the offline homogenization steps, the predicted outcome only holds for the considered (composite) material and light source.

4.5 Conclusions

The addition of filler particles to a traditional VP process adds a large degree of complexity. This work proposes a predictive multi-scale and multi-physical simulation framework for the corresponding AM process. The micro-, meso- and macro-scale each reveal distinct features. Whereas the micro-scale provides effective thermo-mechanical properties at a length-scale where the intensity and corresponding conversion are considered homogeneous, the meso-scale accounts for the (wave-like) interaction of the laser light with the particle-filled resin. To enable full process simulations that account for the presence of the inclusions, the offline micro- and meso-scale simulations provide effective material and scattering properties, respectively, used as input in the macro-scale simulation. Although the description of the individual physics may be considered simplistic compared to other individual and tailored (single-physic) models available in literature, the key characteristics of a complete ceramic VP process are captured. Moreover, the modular set-up of the multi-scale modeling framework allows for more advanced models to be incorporated. This framework enables component scale stress and deformation predictions based on the constituents' material properties and process conditions. Simulating the AM process in an immersed setting* that accounts for a section of the resin/slurry-vat enables to capture typical VP characteristics. This would not be possible using a commonly applied geometry-conforming pre-meshing technique.

Although the conducted study was focused on a resin with an alumina filler, it is expected that the model components are easily tailored to alternative systems with small (compared to the wavelength) inclusions or even homogeneous resins. The description of the (solidifying) polymer can be improved by, for example, incorporating viscoelastic behavior and a more advanced polymerization model. Further advancement of the developed framework can be achieved by capturing the relevant light scattering on the meso-scale using more computationally efficient tools. In the current implementation, the finite element formulation of Maxwell's equations is a limiting factor in the applicability to predict light scattering for larger light source diameters and/or layer thicknesses or more realistic three-dimensional light scattering realizations. Possible research directions are alternative near field methods, such as the multi-sphere T-matrix method (limited to spherical inclusions [39]), that should be able to account for light absorption. Furthermore, the current work only considers a scanning laser VP process, whereas irradiation through mask-projection is also widely applied in the fabrication

* In this context *immersed* is meant purely geometrical, for the visualization of structures it may be considered as a level-set.

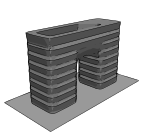

of ceramics. Future work will focus on capturing the relevant effects of that particular approach.

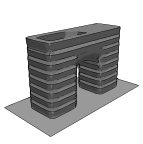

5

Prediction of the deformed geometry: A qualitative validation of the multi-physical model

Abstract

In photopolymerization-based additive manufacturing a complex interplay exists between the vat photopolymerization process characteristics and the (photo-active) resin's material properties, which governs the trajectory from the input target geometry to the resulting true geometry of a printed component. Particularly for fine featured geometries, there might be a clear mismatch between the latter two. Determining whether the entire component is printable can only be properly assessed through a test-print. The current work proposes an alternative modeling-driven route, which, after system and material characterization, facilitates predicting the geometrical defects of the resulting solidified component (including deformation). This is enabled through a coupled multi-physical modeling of irradiation, photopolymerization, mechanical solidification and chemical shrinkage.

Reproduced from: Westbeek, S., Remmers, J. J. C., van Dommelen, J. A. W., Maalderink, H. H. & Geers, M. G. D. Prediction of the deformed geometry of vat photo-polymerized components using a multi-physical modeling framework. *Submitted for publication* (2020)

5.1 Introduction

Vat photopolymerization (VP) is an additive manufacturing (AM) technique capable of fabricating highly accurate polymer components with high speed. The additive process is based on selective irradiation of a photo-active polymer resin by (near) UV light in a layer-by-layer fashion. The relatively low energy input induces a chemical photopolymerization reaction, which in turn causes solidification. Even though the concept of VP might appear more suitable for rapid prototyping, high performance materials with tailored properties for a wide variety of applications are nowadays broadly available [9]. Filling the polymer resin with a powder material—followed by subsequent (post-)processing steps—even enables AM of ceramic or metal components [14, 16, 31, 148].

The challenges in AM generally lie in reproducibility from part-to-part and print-job-to-print-job, productivity/speed of the printing process and size of printable components, i.e. scalability [57]. Adapting a specific process to an intended geometry and/or printer generally also implies a large portion of trial-and-error in tuning process parameters [149]. Naturally, manufacturers provide well documented resins accompanying their proprietary printer in an attempt to resolve part of this issue, but it does not entail a generic solution. A noteworthy path towards increased part quality in VP is the integration of sensors and (closed loop) control schemes into the printer [62, 150, 151].

The complexity of the VP process, in the context of the challenges addressed above, originates from the intrinsic multiphysical nature of the process [78, 131]. Regardless of whether the printing system uses a bottom-up (constrained surface) or top-down irradiation (free surface)—as illustrated in Fig. 5.1 for a two-dimensional irradiation, Digital Light Processing (DLP), system—the VP process starts with the addition of a layer of resin of predefined thickness in the order of 50 μm. As soon as this so-called "recoating" step is completed, the photopolymerization reaction is initiated by a UV projection of the cross-section of the product [19]. Absorption limits the light's penetration depth into the resin. In all locations where enough photons are available to be absorbed by the initiator, the liquid monomer polymerizes; a process which is accompanied by an exothermic temperature increase and chemical shrinkage [152]. As soon as a critical amount of energy, ϵ_c, is supplied, the conversion reaches a threshold and solidification occurs [54]. The accumulated effect of inhomogeneous shrinkage in the stack of layers that shape a component can cause deformation/warpage [63, 108]. The number of relevant physical effects increases further when accounting for effects such as photobleaching [71–74] or the presence of inhibitor species such as oxygen [70, 153–156].

The combination of these effects and their complex interplay makes accurate predictions of the quality of the printed component cumbersome. A simulation tool that captures the multiphysical nature of the AM process greatly enhances the process from design, material, printer and printing conditions towards a functional and

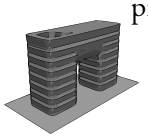

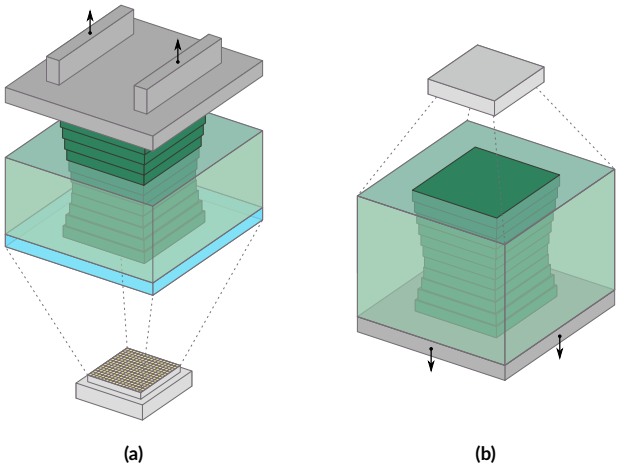

Figure 5.1 Illustration of a typical bottom-up (a) and top-down (b) irradiation DLP system. Compared to the UV light source, the build-plate is located on the opposing side and the arrows denote its direction of motion.

qualitative part. Different authors have worked on modeling the printed part for both scanning laser (stereolithography) and full-field irradiation (mask projection or DLP) systems. Starting from Jacobs' cure depth model [54], in the following papers a rough distinction can be made between attempts that capture the effect of the layered nature of the AM process by applying selective shrinkage to a predefined geometry [55, 63–65, 134] or papers that incorporate highly detailed physics to predict the polymerized profile of a single or a limited number of layer(s) as a function of the UV light input [66, 68–70, 79]. The distinctive characteristic of the current work is that it predicts the printed/solidified geometry on a full-component scale—and the (unintended) deformation/warpage in it—through multi-physical modeling of irradiation, conversion, mechanical solidification and chemical shrinkage, with the sliced cross-sections of the target component as the departing point. This is accomplished by finite element simulation in an immersed setting, for which the model input is the applied irradiation pattern that corresponds to the (sliced) target geometry, analogous to previous work by the authors on VP for ceramics [78, 131]. In contrast to those works, the scope of this work is restricted to the prediction of VP for an unfilled polymer, whilst including a qualitative validation for the DLP process.

In the following, first, the theoretical formulation of the framework will be addressed, after which the experimental approach to obtain validation samples will be introduced. Subsequently, the model parameter identification is presented. The work will be concluded by the validation of the developed simulation framework.

5.2 *Modeling framework*

The developed simulation framework is implemented in a dedicated finite element code tailored for simulating direct and indirect AM processes [133]. The general finite element formulation is considered outside the scope of this work, but the interested reader can find a plethora of relevant literature, e.g., [157, 158]. Within this work, the framework is applied to a bottom-up VP approach (cf. Fig. 5.1), which is schematically depicted in Fig. 5.2. The repetitious process initiates with the build-plate moving upwards by (effectively) a layer thickness. Afterwards, patterned light from the projector enters the vat through the transparent slab, inducing the photopolymerization reaction. The description of the considered physics, i.e. irradiation, photopolymerization, the additive nature of the process and solidification—which rely on the model formulation published in a previous paper [131]—are addressed in the following Sections 5.2.1 to 5.2.4. Effects related to the recoating step, either in a top-down or bottom-up system, are not accounted for and the (instantaneously) deposited layer is considered to be flat [59].

5.2.1 *Illumination*

Capturing the relevant physics starts with a suitable irradiation model for the DLP process at hand, which is based on the work of Kang et al. [68]. In contrast to direct laser illumination, as discussed in Ref. [131], the intensity profile of a single pixel

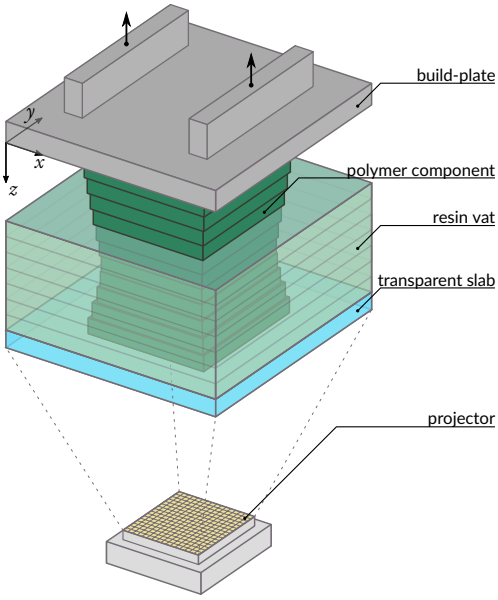

Figure 5.2 Schematic visualization of the bottom-up DLP system considered within this work.

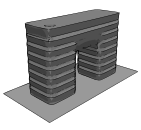

is not a general two-dimensional Gaussian function; instead it reveals a rectangular cross section. The corresponding intensity distribution in a global coordinate system, $\vec{x} \in R^3 = (x, y, z)$, for a pixel i located at $\vec{x}_{S_i} = (x_{S_i}, y_{S_i}, z_{S_i})$, can be formulated as

$$I_{p,i}(\vec{x} - \vec{x}_{S_i}, t) = I_{p,i,\max}(t) \exp\left(-2\frac{[r(\vec{x} - \vec{x}_{S_i})]^2}{[w(\vec{x} - \vec{x}_{S_i})]^2}\right), \tag{5.1}$$

with $I_{p,i,\max}(t)$ the pixel's peak intensity in the horizontal center, i.e. $(x - x_{S_i}, y - y_{S_i}) = (0, 0)$, at time t. In this equation, $r(\vec{x} - \vec{x}_{S_i})$ and $w(\vec{x} - \vec{x}_{S_i})$ are given by

$$r(\vec{x} - \vec{x}_{S_i}) = \|\vec{x} - \vec{x}_{S_i}\|_2, \tag{5.2}$$

$$w(\vec{x} - \vec{x}_{S_i}) = w_0 \frac{r(\vec{x} - \vec{x}_{S_i})}{f_{sq}(\vec{x} - \vec{x}_{S_i})}, \tag{5.3}$$

where w_0 is the intensity distribution's $1/e^2$ Gaussian half-width and f_{sq} ensures the rectangular pixel shape through

$$f_{sq}(\vec{x} - \vec{x}_{S_i}) = \begin{cases} x - x_{S_i}, & \text{if } \left|\frac{y - y_{S_i}}{x - x_{S_i}}\right| \leq 1, \\ y - y_{S_i}, & \text{if } \left|\frac{y - y_{S_i}}{x - x_{S_i}}\right| > 1. \end{cases} \tag{5.4}$$

An example intensity profile of a single pixel is provided in Fig. 5.3. The corresponding total light source intensity profile is then provided by using the cumulative intensity as

$$I_0(\vec{x}, t) = \sum_i I_{p,i}(\vec{x} - \vec{x}_{S_i}, t). \tag{5.5}$$

The horizontal position of a pixel simply follows from the distance between the pixels, i.e. the pitch Π, as $x_{S_i} = \Pi\,(n_x - 1/2)$ and $y_{S_i} = \Pi\,(n_y - 1/2)$. In the latter, n_x and n_y are integers that vary between 1 and the number of pixels in x- and y-direction, respectively, N_x and N_y, i.e. $n_x = 1, 2, \ldots, N_x$ and $n_y = 1, 2, \ldots, N_y$. z_{S_i}, i.e. the out-of-plane position of pixel i, will be addressed later. The result for a 6×6 grid with 8 activated

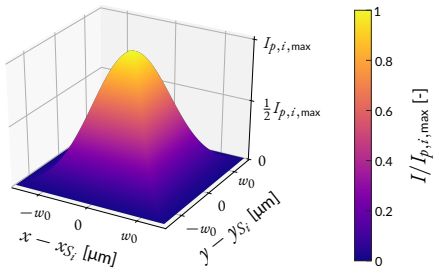

Figure 5.3 Intensity field for a single pixel $I_{p,i}(x_i, y_j)$. The depicted intensity field is normalized by $I_{p,i,\max}$.

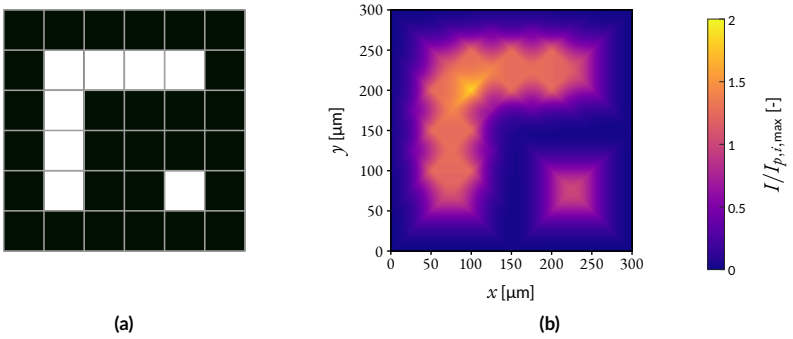

Figure 5.4 Illustration of the accumulative effect of neighboring (activated) pixels for the pixel characteristics shown in Fig. 5.3, $w_0 = 50$ µm and $\Pi = 50$ µm. The activated pixels are shown in (a) and the resulting intensity field is shown in (b). Note that the maximum intensity magnitude is larger than $I_{p,i,\max}$, which is used as a normalization value.

pixels (with characteristics equal to the one in Fig. 5.3, $w_0 = 50$ µm and $\Pi = 50$ µm) is shown in Fig. 5.4. Eq. (5.5) is implemented in the numerical framework as a two-dimensional field that is updated once for every unique layer's bitmap. This is not necessarily equivalent to the number of layers, because components with edges aligned with the z-direction can have the same cross-section across multiple layers.

If we furthermore assume that Beer-Lambert's law provides the in-depth light absorption in the z-direction, the three dimensional intensity profile in the material points (assuming perpendicular incidence) is provided by

$$I(\vec{x}, t) = \tilde{I}_0(x, y, t) \exp\left(-(z_{S_i}(t) - z)/D_p\right) \tag{5.6}$$

with D_p the *penetration depth*, i.e. the depth where the irradiance has reduced to e^{-1} of the initial value [19, 54] and z_{S_i} the z-coordinate where the light enters the material, such that $I(x, y, z_{S_i}, t) = I_0(x, y, t)$, which depends on the number of layers and the layer thickness δ, cf. Fig. 5.2. $\tilde{I}_0(x, y, t)$ in Eq. (5.6) is the result of a linear interpolation step on the (sufficiently refined, but discrete) field I_0, which ensures that the x- and y-coordinates where the two-dimensional intensity field I_0 is stored do not necessarily need to coincide with the (x, y)-coordinate of the material/integration points.

5.2.2 *Photopolymerization*

Different highly sophisticated models exist in literature to capture the physics of photopolymerization in detail [66–75]. For the solidification process, the conversion from monomers to a long-chained polymer is of interest. The conversion process is however influenced by multiple factors that can be accounted for. In a traditional mechanistic form for free radical photopolymerization, one can account for the rate of propagation and termination of the monomer consumption, k_p and k_t, respectively, and

the influence of temperature therein [99], i.e.

$$-\frac{d[M]}{dt} = k_p[M]\left(\frac{\psi I_a}{k_t}\right)^{1/2}. \tag{5.7}$$

$[M]$ in the above equation is the monomer concentration, I_a is the absorbed intensity and ψ the quantum yield for initiation. The differential equation in Eq. (5.7) is completed by an initial condition $[M](0) = [M]_0$. Typically, the progress of the polymerization reaction is quantified by the degree of conversion p:

$$p = \frac{[M]_0 - [M]}{[M]_0} = 1 - \frac{[M]}{[M]_0}. \tag{5.8}$$

Extensions might incorporate more species balances [71–74], the diffusion of species through the resin, or the presence of inhibitor species [70, 159].

To reduce the number of model parameters, this work applies a phenomenological conversion law accompanied by a simple mathematical formulation that accounts for oxygen inhibition. The latter is introduced to capture the limited *print-through*—which is the additional (unintended) solidification in layers before the one currently irradiated—encountered in printed specimens.

The phenomenological monomer evolution can be formulated in a similar form compared to Eq. (5.7), i.e.

$$-\frac{d[M]}{dt} = \mathcal{P}[M]\sqrt{I}, \tag{5.9}$$

with $\mathcal{P}$ a constant rate of polymerization.

Considering that our interest lies in the degree of conversion and not in the evolution of the monomer concentration, the normalized quantity $m = [M]/[M]_0$ is introduced instead. Substituting m into Eqs. (5.8) and (5.9) provides

$$-\frac{dm}{dt} = \mathcal{P}m\sqrt{I}, \tag{5.10}$$

$$p = 1 - m, \tag{5.11}$$

for which $m(t = 0) = m_0 = 1$. This model assumes that eventually all monomer is turned into polymer whereby the conversion reaches one. In practice, after vitrification occurs, the mobility of the non-reacted species decreases and p reaches a plateau value < 1 [31, 62, 154, 160]. To account for this, Eq. (5.11) is pre-multiplied by an asymptote accounting for the degree maximum of conversion, $p_\infty < 1$, such that the absolute conversion reads

$$\hat{p} = p_\infty\,(1 - m)\,. \tag{5.12}$$

In the majority of literature considering VP—instead of accounting for the evolution of the monomer conversion—a relation is identified between the energy input into

the resin and the so-called *cure depth* C_d. For a single source intensity magnitude, a number of different irradiation times is used to characterize the relationship between exposure ϵ and C_d. The relationship between the natural logarithm of exposure, $\ln(\epsilon)$, and C_d is typically found to be linear [54, 159, 161]. The corresponding slope is defined as the penetration depth D_p, i.e. the same parameter as introduced in Eq. (5.6). The intersection with a C_d of zero is the so-called *critical exposure* ϵ_c [19]. To relate the resulting *working curve*, i.e. $C_d(\epsilon)$—and in particular the critical exposure—to Eqs. (5.10) and (5.11), it is key to note that after exposure of the resin with ϵ_c, gelation occurs and solidification initiates. In the framework of polymerization, this tipping point is generally termed the *gel point*, i.e. p_{gel} [54].

The working curve has proven to be a valuable tool for characterizing resins in VP and for tailoring process parameters to improve printing quality. It is, however, derived from a single resin exposure. Consequently, in a multi-layer process, it does not capture the extent of the solidification accurately, or, to put this more clearly: relying only on the exposure in a material point, a large amount of (non-existent) print-through would be predicted. To overcome this limitation, different researchers make use of (partial) differential equations to accurately capture the cure evolution [70, 75, 155, 156, 162]—even while only considering a single irradiation step, i.e. the conversion of a single layer. Usually, the limiting factor is attributed to the inhibition of oxygen. A more phenomenological approach to capture this effect is used in the work of Kang et al. [68], who experimentally identified a critical intensity based on the irradiation time that follows a relationship of the form $I_c = a\ln(t/1[s])+b$, where a is found to be < 0 and b is the intensity threshold at $t = 1$ s. The critical intensity acts as a threshold value; if a certain exposure is applied in a specific time interval, then the intensity should at least be I_c to support solidification. For the time-continuous modeling framework in this work, we invert this logarithmic relationship, giving an inhibition induced time delay:

$$\tau_d = \exp\left(\frac{\iota_c - I(\vec{x})}{\iota_s}\right), \tag{5.13}$$

where ι_c and ι_s are two resin/process constants with the unit of intensity. The purpose of Eq. (5.13) is to postpone the initiation of the conversion process, by enforcing $d[M]/dt = 0$ while $t < \tau_d$. Note that the phenomenon of a time delay is also observed experimentally [62, 150].

5.2.3 *Capturing the additive nature*

In simulating an additive process, the size of the computational domain continuously increases. To circumvent the associated bookkeeping required, the most common methods for AM simulations perform a pre-meshing of the target printed geometry. Imitating the additive nature of the process is typically done using an element activation technique [163, 164].

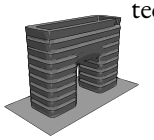

In this work, the outcome/resulting geometry is not assumed a priori, but follows from the process simulation instead—through the input irradiation. A section of the (resin) vat, inside which the part fits, is defined as the computational domain. New elements are added, one layer at a time, before moving to the next irradiation step.

This procedure may seem similar to the aforementioned conventional pre-meshing of the target geometry, but this only partly true. Highly similar is that the nodes of the newly added elements are placed at the coordinates where they were 'intended' in the predetermined computational domain, i.e. the vat section, which can be done conveniently since the finite element mesh is of a voxel type. The major difference lies in the applied immersed setting, which allows updating the contour of the emerging solidified geometry.

5.2.4 Evolution of the mechanical properties

The modeling framework accounts for two aspects affecting the evolution of mechanical properties. These are *(i)* the shrinkage that is associated with the polymerization and *(ii)* the progression of the (solid-like) material's properties during solidification. The influence of temperature is neglected while considering the above aspects in combination with an elastic constitutive behavior, i.e. the process is assumed isothermal. This simplification is made since it is the final printed state that is of interest here (with a homogeneous temperature throughout the component). Only a limited influence of thermal expansion during the irradiation step is expected.

Whereas the physics in Sections 5.2.1 and 5.2.2 can be solved inside a material point using the source and initial conditions, for the mechanics, a balance equation has to be solved on the entire computational domain. The linear momentum balance, omitting dynamic effects, i.e. assuming a quasi-static process, is formulated as

$$\vec{\nabla} \cdot \sigma(\vec{x}) + \rho \vec{b} = \vec{0}, \tag{5.14}$$

where σ is the stress tensor, $\vec{b}$ is the gravitational (body) force vector per unit volume and ρ the mass density. Strains enter Eq. (5.14) through the constitutive equation, which, in this work, is given by Hooke's law:

$$\sigma(\vec{x}) = {}^4\boldsymbol{\mathcal{C}}(\vec{x}) : \varepsilon_{\mathrm{e}}(\vec{x}), \tag{5.15}$$

with ${}^4\boldsymbol{\mathcal{C}}$ the fourth-order elastic stiffness tensor and ε_{e} is the elastic strain tensor.

The total strain consists of the combination of the elastic strain ε_e and the polymerization shrinkage strain $\varepsilon_{\mathrm{ch}}$, i.e.

$$\varepsilon(\vec{x}) = \varepsilon_{\mathrm{e}}(\vec{x}) + \varepsilon_{\mathrm{ch}}(\vec{x}). \tag{5.16}$$

$\varepsilon_{\mathrm{ch}}$ is linearly dependent on the conversion via

$$\varepsilon_{\mathrm{ch}}(\vec{x}) = \tfrac{1}{p_\infty} \hat{p}(\vec{x}) \varepsilon_{\mathrm{ch,max}} I, \tag{5.17}$$

in which $\varepsilon_{\text{ch,max}}$ is the strain at maximum conversion p_∞ and I the unity tensor to account for the volumetric shrinkage. If needed, Eq. (5.16) can be further extended with e.g. thermal, viscous and plastic strains.

Using a finite element discretization, the total strain needs some additional considerations. Upon generation of a new layer of material—with its corresponding new nodes at the intended positions, and pre-existing nodes from the previous layer in a deformed configuration, cf. Section 5.2.3—an initial strain already exists. This prior strain, present in the element upon introduction, should not induce any stress and is therefore extracted from the (current) element's strain (inside the integration points) to obtain the total stain, i.e.

$$\boldsymbol{\varepsilon}(\vec{x}) = \boldsymbol{\varepsilon}^{\text{el}}(\vec{x}) - \boldsymbol{\varepsilon}_0^{\text{el}}(\vec{x}), \tag{5.18}$$

which is next substituted in Eq. (5.16).

The second aspect of the evolution affects Eq. (5.15) through the stiffness tensor ${}^4\boldsymbol{\mathcal{C}}$. The isotropic linear elastic formulation of ${}^4\boldsymbol{\mathcal{C}}$ is a function of the Poisson's ratio ν and the Young's modulus E. To capture the solidification, the Young's modulus is defined conversion dependent:

$$E(\hat{p}) = \begin{cases} e_0 E_{\text{pol}} & \text{for } \hat{p} < p_{\text{gel}}, \\ \left(\frac{1-e_0}{p_\infty - p_{\text{gel}}} \left(\hat{p} - p_{\text{gel}} \right) + e_0 \right) E_{\text{pol}} & \text{for } \hat{p} \geq p_{\text{gel}}. \end{cases} \tag{5.19}$$

This bilinear function uses a lower bound for E, for conversion $< p_{\text{gel}}$, which is much smaller than the polymerized Young's modulus E_{pol} by multiplication with $e_0 \ll 1$. Once the gel point is reached, the Young's modulus linearly increases from $e_0 E_{\text{pol}}$ to E_{pol} at maximum conversion p_∞. Technically, in the fluid phase the resin's E is not defined, but—since the interest lies in the solidification—a value close to zero suffices and facilitates the (immersed) finite element simulation. The resulting stiffness matrix is isotropic and the Poisson's ratio is assumed constant.

The mechanical description is completed by appropriate boundary conditions: at $z = 0$ the displacements of the nodes are fully constrained to account for a proper bonding with the build-plate. Because the simulation only considers a section of the (resin) vat, the lateral boundaries of the domain are allowed to contract freely. The separation force related to bottom-up VP systems—associated with detachment from the transparent slab, cf. Fig. 5.2—is not accounted for.

5.3 Experimental setup

The modeling framework is qualitatively validated through a geometrical correlation with physically printed samples. The following Sections 5.3.1 and 5.3.2 address the experimental approach and the (intention of the) printed geometries, respectively.

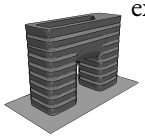

5.3.1 Process characterization

In order to perform the validation step, a number of sample geometries are printed on a Rapidshape S60 mini DLP printer, which was schematically depicted in Fig. 5.2. The pixels' pitch Π is approximately 48 μm and layers are printed with a thickness $\partial = 50$ μm (which are self-corrected with +/–10 μm accuracy).

Samples are printed with a prototyping material containing multiple methacrylates, 2 wt% photo-initiator Irgacure 819 and 0,017 wt% of a blue light-blocking dye. The corresponding working curve parameters are a critical exposure ϵ_c of 11 mJ/cm^2 and a penetration depth D_p of 270 μm. The geometries are not additionally reinforced by support structures during printing. To ensure sufficient bonding with the base plate, the first three layers are printed with an exposure of $\epsilon_0 = 100$ mJ/cm^2, while the exposure for the remaining layers is $\epsilon_1 = 18$ mJ/cm^2.

After printing, the samples are removed from the base plate using a glass scraper and cleaned (twice) using IPA in an ultrasonic cleaner. The samples are not post-cured, in line with the numerical simulations.

To extract the full three-dimensional geometrical shape of the printed samples, an industrial μCT scanner (Phoenix Nanotom) is used. The samples are attached to a rod—on which the sample rotates for imaging purposes—at the build-plate-cut-plane using a small amount of clay material. Using the clay, the samples are placed at an angle to optimize the visualization, but the clay can leave traces in the processed geometries. Although multiple samples are printed of each geometry, see Section 5.3.2, only two are examined. From the resulting three-dimensional voxelized data, obtained with a resolution of 4 μm, the outside contours are extracted in an stl-format—after removal of the air and rod/clay (by thresholding using VGStudioMax software, version 1.0)—to conveniently compare to the numerically obtained data. Using these (relatively) high resolution images allows to assess the solidified contour of individual layers and the presence of small scale defects.

5.3.2 Components' geometry specification

Three different sample categories are printed, all of size ≤ 3 mm. The design of these will be introduced—and compared to the actually printed samples—in Sections 5.3.2.1 to 5.3.2.3. An additional simple brick like shape ($5 \times 4 \times 3$ mm^3) is printed for characterization of the mechanical properties by indentation experiments.

5.3.2.1 Pixel characterization

The first sample, displayed in Fig. 5.5, is tailored to identify the irradiation characteristics of the system. It consists of a rectangular base ($1750 \times 1750 \times 500$ μm^3) that has its lateral faces aligned with the x-, y- and z-direction of the printer, with simple characterizing features on top. The smallest features are two layers high ($2\partial = 100$ μm) with a dimension of 50 μm in the horizontal plane. The dimensions of the square shapes on

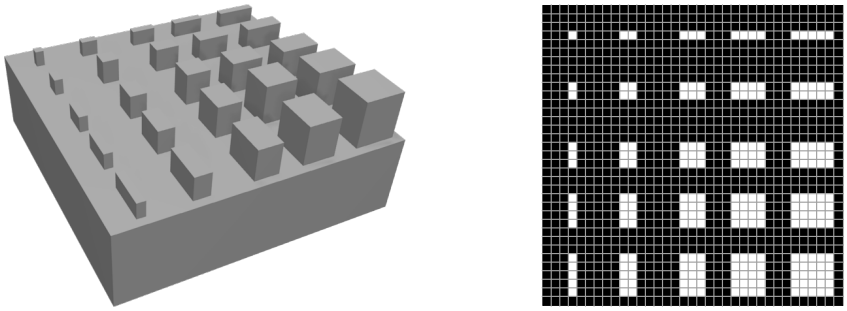

(a) (b)

Figure 5.5 Visualization of the irradiation characterization sample. Total dimensions of the part are $1750 \times 1750 \times 800$ µm^3 and all features are coinciding with a 50 µm interval grid in x-, y- and z-direction. A perspective view is shown in (a) and an xy-plane, just above the base ($z = 500$ µm), is depicted with the grid in (b).

the diagonal from the top-left to the bottom-right equal 50, 100, 150, 200 and 250 µm. From small, to large, the height of these shapes increases by a single layer-thickness δ. The remaining shapes have the same dimensional length, width and height as the (smallest) in-line (w.r.t. the x- and y-axis) shape on the (from the top-left to the bottom-right) diagonal. Due to the pitch between pixels, the shapes are expected to consist of one to five pixels in a row. Considering the printed sample will always be the result of the multi-physical process, the thickness of the base is chosen thick enough to ensure that shrinkage and (resulting) deformation have minimal influence.

Two of the printed geometries are displayed in Fig. 5.6. The samples show the widened first three layers as a result of the increased energy input and a repetitive pattern in both vertical and horizontal directions, induced by the layers and individual pixels,

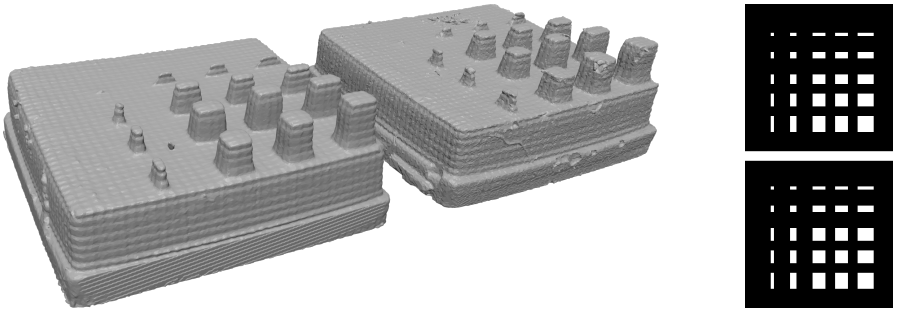

(a) (b)

Figure 5.6 The geometry of two printed samples, as obtained from CT imaging. A perspective view is shown in (a) and the corresponding bitmap (input geometry), for the left (top) and right (bottom) component, at the xy-plane just above the base are depicted in (b).

respectively. Minor variations between the samples exist which are introduced by—but definitely not limited to—minor differences in the sliced cross-sections (as can be deduced from Fig. 5.6b) and inhomogeneities in the intensity field from the mercury-vapor lamp in the DLP system, for different positions on the print bed, and the cleaning process.

When comparing the target geometry (Fig. 5.5) to the actually printed ones (Fig. 5.6) a significant deviation becomes clear. The most obvious differences are the rounded shape of the edges of both the sample's base and pillars and the fact that a single (row of) pixel(s) is insufficient to ensure solidification. For the $100 \times 100\ \mu m^2$ (2×2 pixels) square pillar only hardly distinguishable features remain. This illustrates the profound influence of the pixel characteristics—and the knowledge thereof—for the fabrication of fine featured components.

5.3.2.2 *T-shape*

The second geometry allows to identify the warpage in a free-standing overhang, to tailor the predicted print-through in the model. Different sizes are printed, as shown in Fig. 5.7, with the corresponding (target) dimensions specified in Table 5.1. Note that the different samples are symmetric around the central vertical axis, which motivates the T naming convention. The pedestal is added to ensure proper bonding to the base plate of the

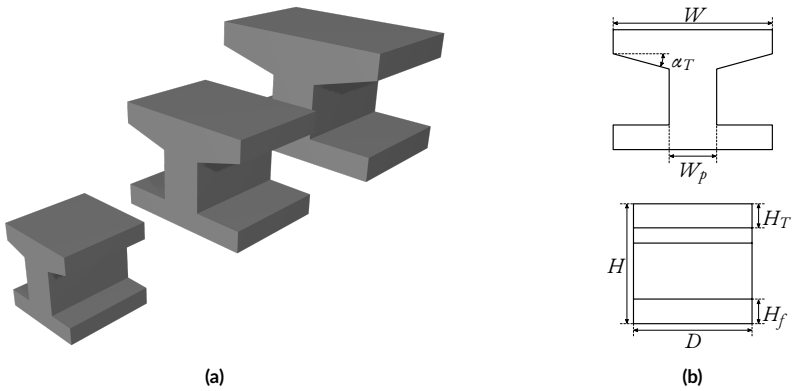

Figure 5.7 Geometry of the target $T_{1\text{-}3}$-samples in (a) with the dimensions in front- and side-view in (b). Values for the dimensions are provided in Table 5.1.

Table 5.1: T-sample dimensions as depicted in Fig. 5.7b.

	W [µm]	W_p [µm]	H [µm]	H_T [µm]	H_f [µm]	D [µm]	α_T [°]
T_1	1000	400	1000	200	200	1000	15
T_2	2000	600	1500	300	300	1500	15
T_3	3000	800	2000	400	400	2000	15

printer.

The result after slicing, printing and cleaning is shown in Fig. 5.8. Whereas in the

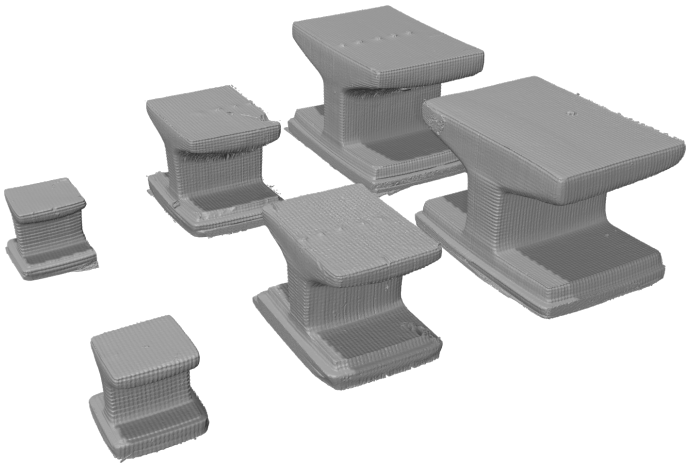

Figure 5.8 Geometry of the printed T_{1-3}-samples with different sizes, i.e. 1, 2 and 3 mm width, two of each.

intended samples the faces are flat and the corners sharp, cf. Fig. 5.7, this is no longer the case for the printed samples. Even though some curvature can be recognized in the top section of the T, the amount of warpage is rather limited. Furthermore, based on the absence of surplus thickness in the overhang, the amount of print-through appears small. These findings should be confirmed in the modeling approach in Section 5.4.

5.3.2.3 H-shape

The final sample category is shaped in the form of an *H* on a pedestal, as shown in Fig. 5.9. Sample dimensions are provided in Table 5.2. This geometry is based on an

Table 5.2: H-sample dimensions as depicted in Fig. 5.9b.

	W [µm]	W_p [µm]	H [µm]	H_H [µm]	H_p [µm]	H_f [µm]	D [µm]	α_H [°]
H_1	1000	200	1500	200	400	500	1000	15
H_2	2000	400	2000	300	600	500	1500	15
H_3	3000	600	2500	400	800	500	2000	15

H-shaped diagnostic sample which is frequently used to benchmark the accuracy of an SLA system [165–168]. However, in comparison, the currently printed H-samples are smaller in size and include a sloped overhang. As a result, they do not require any support structures. The addition of a pedestal ensures proper bonding to the build-plate for the smaller sample(s).

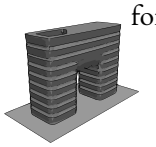

The H-samples were fabricated to quantify a number of interesting phenomena in the VP process [165], which are also shown by the printed samples. This is illustrated in Fig. 5.10, which depicts the three-dimensional scanned geometries and a cross-section through the middle of the part. The cross sectional contours in Fig. 5.10b are incorporated to illustrate that all samples show a particular deformation pattern. Firstly, the cross-sectional width of the part is more narrow in the horizontally connected regions, i.e. near the base and the overhang, compared to in the pillar sections. Furthermore, the top pillars seem to warp outwards—an effect that is most dominant starting from the overhang, which is referred to as a waist distortion [165]. Whereas the overall contour of the part is fairly smooth, indicating sufficient cure, the overhang

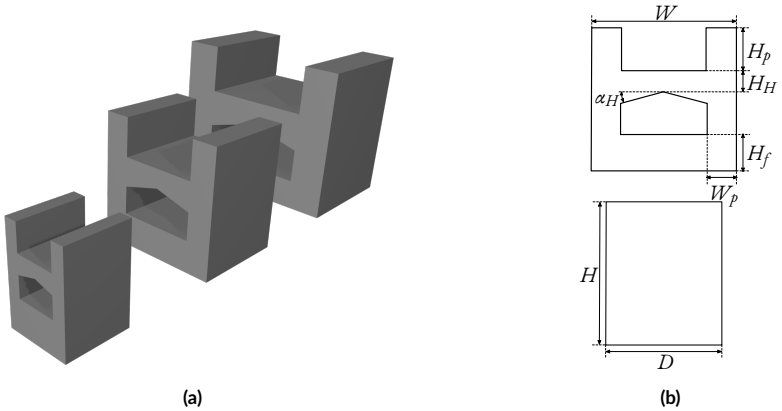

Figure 5.9 Geometry of the target H_{1-3}-samples in (a) with the dimensions in front- and side-view in (b). Values for the dimensions are provided in Table 5.2.

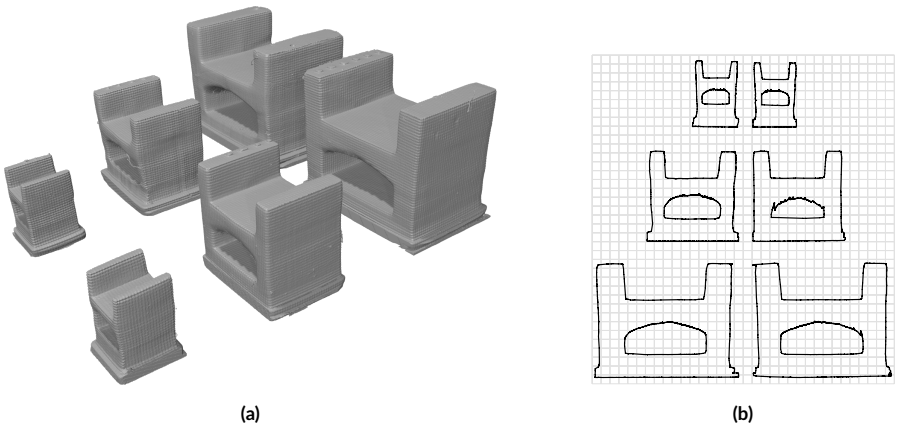

Figure 5.10 Geometry of the printed H_{1-3}-samples in different sizes, i.e. 1, 2 and 3 mm width, two of each are shown in (a). In (b) the middle cross section is displayed on top of a(n arbitrary) square grid for all samples in (a), to better illustrate the deformation.

section is jagged. This illustrates the print-through effect and demonstrates that the cleaning process can have a significant influence on the resulting thickness of overhang regions, when there is no sharp gradient in the conversion profile [153].

5.4 Parameter characterization

In the following Sections 5.4.1 and 5.4.2, first, the conversion parameters are characterized, followed by identification of the solidification characteristics. Even though a subdivision in parameter categories is used, it is key to note that the simulation results are the lumped effect of all the chemo-mechanical model parameters. Simulation results are obtained with 3 cube elements per layer thickness while the intensity interpolation grid points are spaced 5 µm apart and applied exposures are equal to the values denoted in Section 5.3.1. Only the sample in Fig. 5.5 and the smallest samples in Figs. 5.7 and 5.9, i.e. T_1 and H_1, are used for the parameter identification.

5.4.1 Conversion characteristics

The pixel characterization sample introduced in Section 5.3.2.1 is tailored to identify irradiation characteristics. For the input intensity a representative value of $I_0 = 100$ W/m^2 is chosen [159], which, combined with a specific irradiation time provides the critical exposure. Process parameters that have a profound influence are the pixel properties, i.e. $I_{p,i,\max}$ and w_0 in Eqs. (5.1) to (5.3). Together with the conversion parameters, $\mathcal{P}$, ι_c and ι_s, they govern the volume that solidifies.

The optimal combination of these parameters is found as $I_{p,i,\max} = 24$ W/m^2, $\mathcal{P} = 2.25 \cdot 10^{-2}$ m s^{-1}W$^{-1/2}$, $\iota_c = 50$ W/m^2 and $\iota_s = 15$ W/m^2. w_0 follows from the combination of $I_{p,i,\max}$ and the (average) plateau value that provides I_0—for a sufficiently large grid of pixels, i.e. in this case 50×50 using $\Pi = 48$ µm—resulting in $w_0 = 70.32$ µm. The conversion rate $\mathcal{P}$ follows directly from the critical energy. In this case, it is found that the efficiency of the reaction needs to be reduced to 75% of the expected value to account for effects such as the shelf-life of the resin or the status of the light source. The provided value of $\mathcal{P}$ ensures that $\hat{p} = 0.75 p_{\text{gel}}$ is reached after applying the critical exposure ϵ_c whilst accounting for $p_\infty = 0.7$, which will be addressed in Section 5.4.2.

Both the simulation result and the resulting printed pixel characterization sample are displayed in Fig. 5.11 for the two sets of input bitmap slices displayed in Fig. 5.6b. Note that the depicted simulation results show the (deformed) volume with $\hat{p} > p_{\text{gel}}$. The absolute distance between the CT-scanned sample and the simulated geometry—extracted using the open-source software CloudCompare [146]—is included by color grading, revealing that the difference for the majority of the data points remains well below 25 µm. Fig. 5.11 indicates the relevance of the irradiance characteristics. Even though features of $1 \times n$ are irradiated, no (remaining) solidification occurs. On the other hand, the smallest irradiation surface that provides a distinguishable feature on

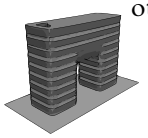

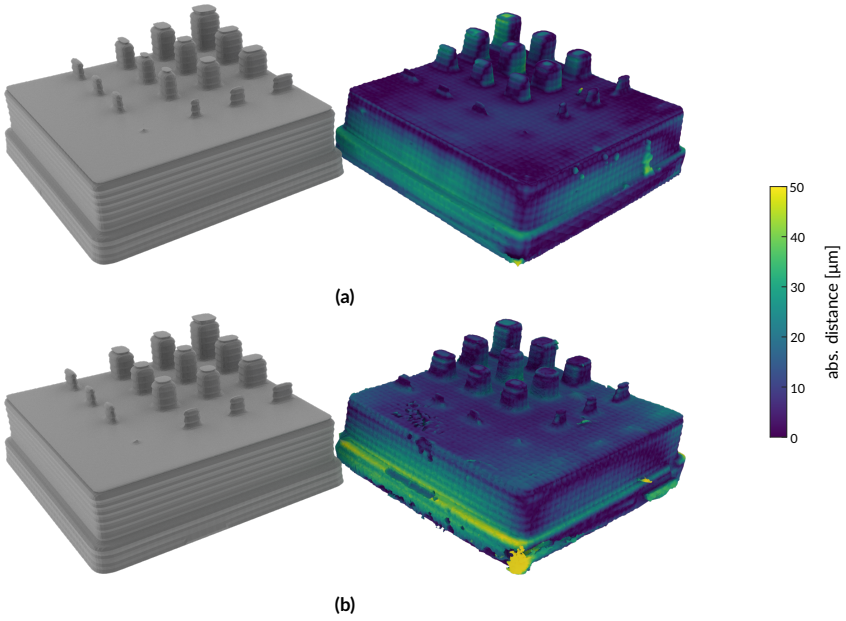

Figure 5.11 Comparison of the simulated geometries for the pixel identification sample with the CT-scanned sample for the identified model parameters. Graphs (a) and (b) show two different simulations with the input bitmap of the corresponding printed sample, as indicated in Fig. 5.6b. Gray image (left) is the simulation result. The colored image (right) illustrates the absolute difference (in µm) between the printed sample and the simulated sample. The range of the color bar is limited to 50 µm.

the resulting print is the 2×2 area. Even though it results in a minimal protrusion, the simulation framework is capable of capturing it. For the printed pillars—and the contour of the base as well—the simulation result under-predicts the widening effect from top to bottom, but this effect is limited and therefore considered acceptable. Note that, unlike the printed samples, the simulated samples are still rigidly connected to the build-plate. Due to the linear-elastic material model and the increased energy dose in the first three layers, with the corresponding higher amount of shrinkage, a build-plate release would induce an unrealistic concave deformation pattern of the sample as a whole. Indeed, the first three layers will be subjected to inelastic strains more significantly. The bottom of the printed samples is also relatively flat because these are cut from the base plate and no subsequent post-curing is applied.

The T-sample in Fig. 5.7 is ideal for identification of the print-through effect. Ideally, the amount of print-through would follow from the experimentally determined working curve, specifically through D_p. Here we require both τ_d, i.e. Eq. (5.13), and a slightly increased absorption, i.e. by 125%. The corresponding D_p that is input in the model is 216 μm, cf. the experimentally obtained value introduced in Section 5.3.1. Even with this reduced depth of penetration, the simulation slightly over-predicts the print-through effect for the T-sample, as shown in Fig. 5.12. The (absolute) difference between two printed samples and the simulation result is again indicated by the coloring of the printed samples, this time for three different views as depicted in Fig. 5.12a-c, respectively. The two dimensional representation is not ideal, but in the following only a single view is presented. In Fig. 5.12 a significant difference is noticeable between the two (right-hand side) printed samples. Whereas for the middle, i.e. first printed, sample the absolute difference is—with exception of some excess material on the pedestal—less than a layer thickness, the second sample does surpass that value. This is a clear indication of the limited reproducibility in the AM process, presumably caused by a local area of reduced intensity in the projection. An interesting observation is that the simulated result shows an influence of the geometrical slicing in the angled overhang, but in the printed samples this effect is hardly noticeable.

5.4.2 Mechanical properties

Two different samples are of interest for the mechanical model description, i.e. the brick like sample and the smallest H-sample in Fig. 5.9. Of these, the former provides the Young's modulus at an assumed Poisson's ratio and the latter is used to determine the resin's shrinkage.

Indentation experiments on the brick-like sample for indentation depths ranging from 5 to 10 μm do provide a consistent Young's modulus of $E \approx 1$ GPa (with $\nu = 0.4$) for an exposure of ϵ_1. This is reflected by the simulation framework through the incorporation of an equivalent value for E at the conversion corresponding to ϵ_1, i.e. ≈ 0.5. Using $p_\infty = 0.7$, the Young's modulus at maximum conversion is chosen as $E_{\text{pol}} = 1.7$ GPa. The corresponding Poisson's ratio is $\nu = 0.4$.

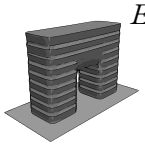

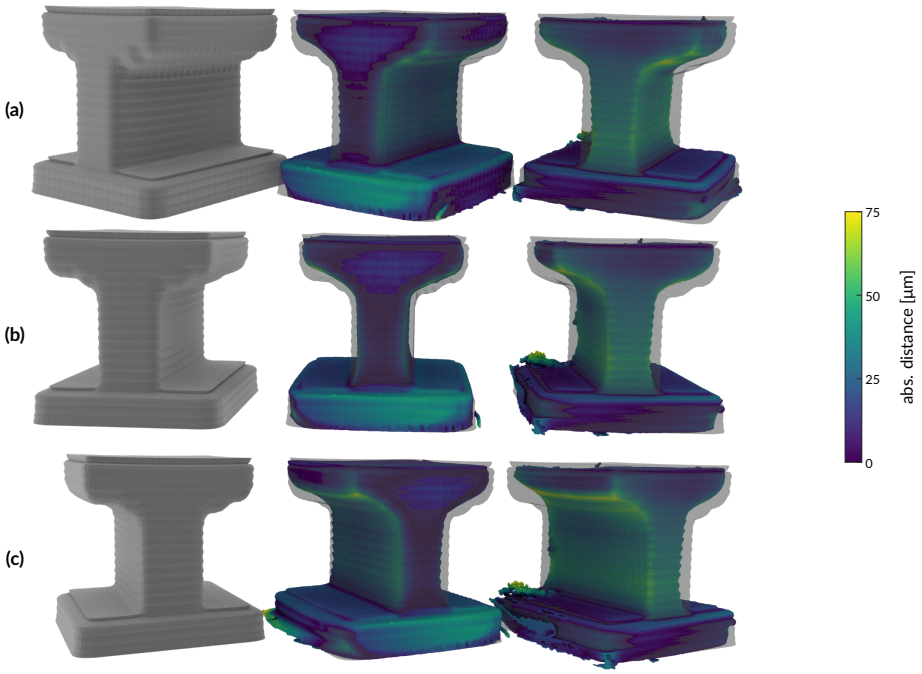

Figure 5.12 Comparison of the simulated geometry for the small T-shape with the CT-scanned sample for the identified model parameters from three different angles, in (a)-(c). Gray image (left) is the simulation result, colored images (other two) illustrate the absolute distance (in µm) from the printed samples to the simulated sample. The range of the color bar is limited to 75 µm. For visual comparison, the CT images also include a transparent simulation geometry.

The shrinkage strain is identified by comparing the deformation of the simulated H-sample to that of the printed ones, giving $\varepsilon_{\text{ch,max}} = -0.05$, which is representative for an acrylic resin [55]. This maximum shrinkage strain holds for the conversion asymptote p_∞, which has been chosen at 70% conversion to capture the physical process limit [31, 62, 154, 159, 160, 169] and, to a lesser extent, to limit the inhomogeneity of shrinkage within the sample, i.e. within a single layer and considering the different input exposures ϵ_0 (first 3 layers) and ϵ_1 (other layers). To account for the gravitational body force, i.e. $\vec{b} = (0, 0, 9.8)$ m/s^2—even though the significance is small at the length scale of the considered samples—the mass density of the medium, ρ, is assumed constant throughout the conversion and equal to 1150 kg/m^3.

The simulation result is visualized in Fig. 5.13 and shows remarkable correspondence with the printed samples. Yet, there are also some notable differences. Even though the widening of the first three layers is correctly captured, the printed samples show a larger shrinkage in the pedestal. For the printed samples, this difference appears more pronounced for the sides aligned with the 'geometrically-extruded' direction. This effect might therefore be induced while printing the remainder of the structure, i.e. the pillars

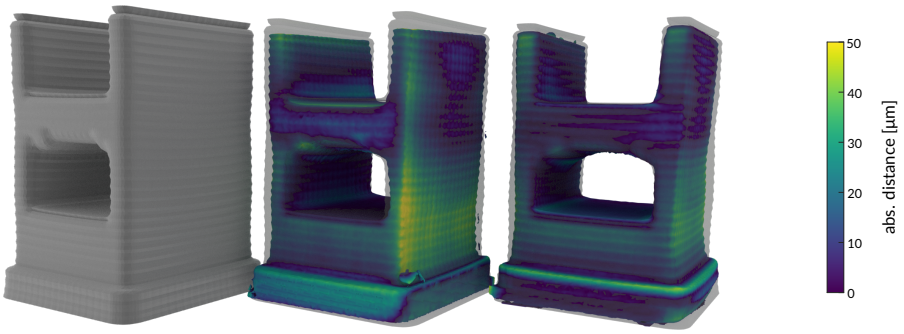

Figure 5.13 Comparison of the simulated geometry for the small H-shape with the CT-scanned sample for the identified model parameters. Gray image (left) is the simulation result, colored images (other two) illustrate the absolute distance (in µm) from the printed sample to the simulated sample. The range of the color bar is limited to 50 µm. For visual comparison, the CT images also include a transparent simulation geometry.

and overhang. The outward directed warpage of the top pillars and the waist of the H-sample is captured accurately, but the total height of the printed samples is roughly a layer thickness less, compared to the simulated result. Note that the printed geometries do not show a variation larger than that, i.e. < 50 µm.

5.5 Model validation

A total of three differently sized T- and H-samples are printed and analyzed, as addressed in Section 5.3. The two larger samples, with a width equal to two and three times that of the small sample (cf. Tables 5.1 and 5.2) are considered for model validation, i.e. to identify whether the size dependence can be captured accurately. The parameter set identified in Section 5.4 is used for this purpose. The largest samples (T_3/H_3) are simulated with a reduced resolution, i.e. 2 cube elements over the layer thickness.

5.5.1 T-shaped sample

The results for the T-shaped samples are depicted in Figs. 5.14 and 5.15 for the 2 and 3 mm wide sample, i.e. T_2 and T_3, respectively. In addition to the comparison of the simulated result to the printed result (top row), the difference between the target geometry—which is used for the sliced input into the DLP printer—and the printed sample is now also included (bottom row). For the T_2 sample, Fig. 5.14, the simulated geometry clearly matches the printed results quite accurately. The difference of the target geometry with the printed samples (experimental deviation) is much more pronounced. For the larger T_3 sample, printing induced geometrical errors become less pronounced. Judging from the shape—including the rounded edges, pedestal broadening and reduction of the pillar width—the simulation does provide an accurate prediction of

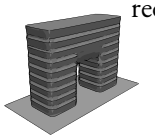

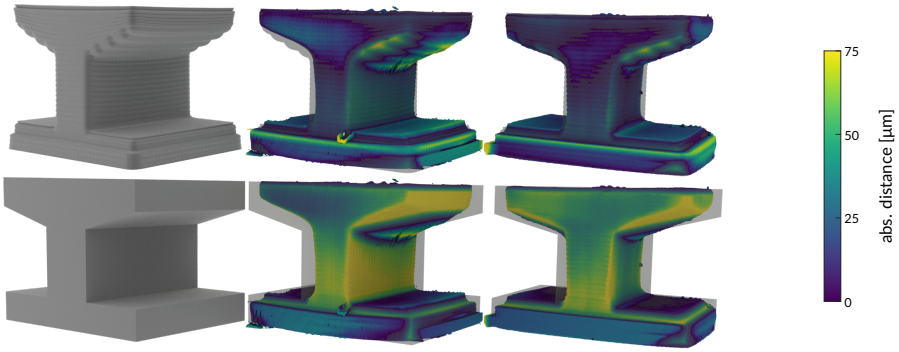

Figure 5.14 Comparison of the simulated geometry with the printed samples (top row) and the target geometry with the printed samples (bottom row) for the T_2-shape. The range of the color bar is limited to 75 µm. For visual comparison, the CT images also include a transparent simulation/target geometry.

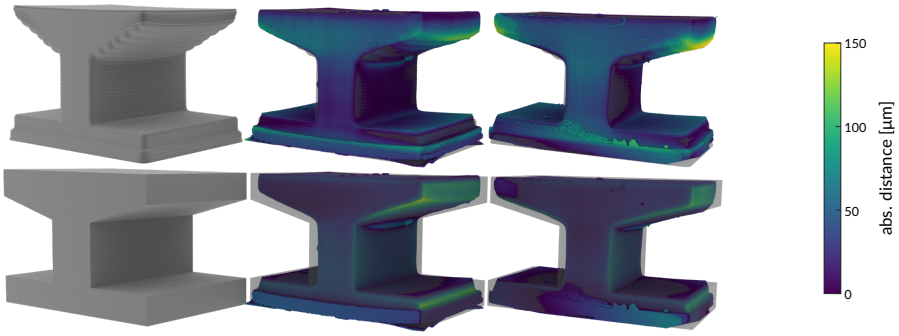

Figure 5.15 Comparison of the simulated geometry with the printed samples (top row) and the target geometry with the printed samples (bottom row) for the T_3-shape. The range of the color bar is limited to 150 µm. For visual comparison, the CT images also include a transparent simulation/target geometry.

the resulting geometry. A significant deformation, which is not present in the printed samples, is however predicted in the overhang inducing narrow end-sections at the edges of the horizontal T-section. This indicates a restriction of the modeling framework in that it does not capture, e.g., the contact with the transparent slab, cf. Fig. 5.2. The differences between the target, predicted and printed samples for the two different sample sizes also indicate that the relevance of (geometry) predictive models in AM is more pronounced when printing samples/features closer to the resolution of the printer.

5.5.2 H-shaped sample

The results for the H-shaped samples are depicted in Figs. 5.16 and 5.17 for the 2 and 3 mm wide sample, i.e. H_2 and H_3, respectively. When comparing the simulated, intended and printed results, the conclusions that were drawn for the T-sample also apply here. A

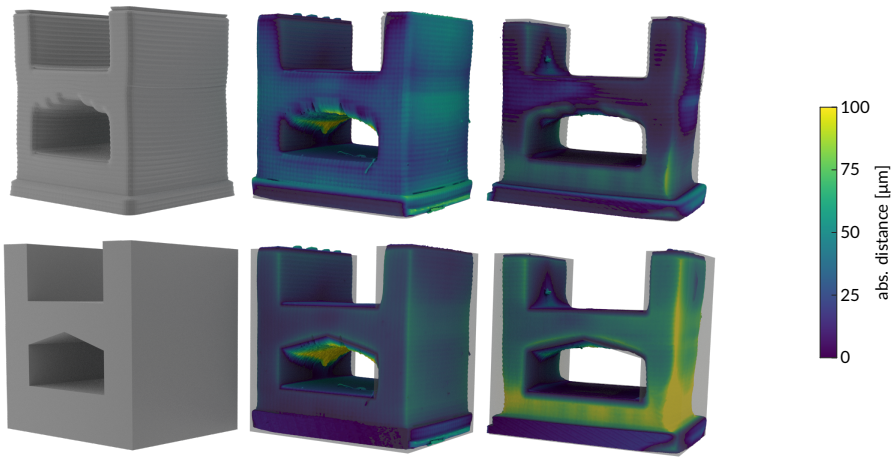

Figure 5.16 Comparison of the simulated geometry with the printed samples (top row) and the target geometry with the printed samples (bottom row) for the H_2-shape. The range of the color bar is limited to 100 µm. For visual comparison, the CT images also include a transparent simulation/target geometry.

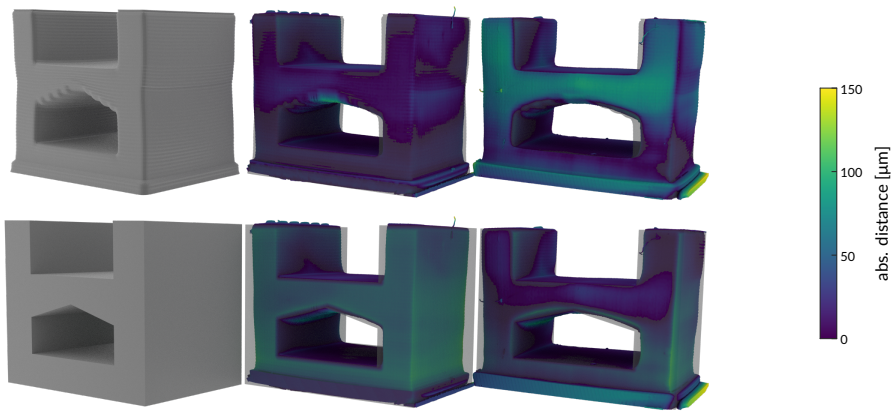

Figure 5.17 Comparison of the simulated geometry with the printed samples (top row) and the target geometry with the printed samples (bottom row) for the H_3-shape. The range of the color bar is limited to 150 µm. For visual comparison, the CT images also include a transparent simulation/target geometry.

large difference is present between the two printed H_2 samples in Fig. 5.16 due to process inaccuracies. This induces a large deviation from the target result in the rightmost printed sample, which is accurately captured by the simulation. For both printed shapes, the overhang (and the corresponding print-through) and the deformation are accurately captured by the simulation. The outward warpage of the top pillars (further away from the waist itself) remains under-predicted.

5.5.3 Discussion

The simulation results in Sections 5.5.1 and 5.5.2 illustrate the need for predictive modeling and the added value of the developed framework. Some additional (more general) remarks need to be made.

Firstly, the limited reproducibility in the printed samples limits the correspondence with simulation results. It is key to identify any causes for a limited reproducibility—which might originate from, e.g., the cleaning process or the characteristics of the irradiation source—and how to overcome these in practice [62]. In the current work, the samples are inspected right after removal from the print bed after printing, i.e. no post-curing is conducted. Note that this might have an additional influence on the resulting shape and (mechanical) properties [170].

The parameter characterization in this work relies on the identification of model parameters through numerical simulations. This implies that the modeling parameters may not be necessarily equal to the physical parameters and the model validation is of a qualitative nature, i.e. to identify whether the correct trends are captured through the multi-physical approach (with some more phenomenological ingredients). The mathematical formulation of the numerical framework is already involved from a parameter identification point of view. From a physical perspective, however, the level of detail is still limited. Due to the restricted fluid behavior, for example, the current method is not ideal for the prediction of printability of an overhang structure. The photopolymerization provides a final conversion between 0 and the peak conversion (p_∞), but it is independent of the depletion of the photoinitiator. Furthermore, the current implementation of oxygen inhibition ensures a good correspondence to the actual printed samples, but assumes full replenishment of oxygen from one irradiation to the next. This might appear oversimplified at first, but the agreement of the predictions indicate an adequate accuracy accompanying the phenomenological description of multiple effects. Possible effects are (but not limited to) the diffusion of oxygen through the resin, substitution of irradiated (but not solidified, i.e. liquid) resin during the recoating step and vitrification [154]. Whereas the phenomenological approach suits the goal of this work, enabling efficient component-scale simulations, a more accurate description might account for the presence of initiator and inhibitor (e.g., oxygen) species though additional ODEs [70, 75]. Although in the current model, the interest lies in geometrical prediction—for a qualitative validation with printed specimens—the mechanical formulation would also allow for the prediction of residual stresses. Due to

the purely linear elastic assumption—neglecting viscous effects—the predicted stresses might be considered an upper limit.

5.6 Conclusion

The characteristics of the AM apparatus and the material properties and process physics have a profound influence on the (quality of the) printed specimens. This work proposes a modeling framework for three-dimensional process simulation of the DLP VP process in order to predict the resulting geometry and the (unintended) deformations therein.

This is enabled through the development of a chemo-mechanical simulation framework that starts with the irradiation characteristics of the DLP system. To ensure that the resulting geometry is not affected by the computational domain, the process is simulated in an immersed region for which a (sufficiently large) volume of the resin vat is simulated. This is distinct from typical component-scale simulation frameworks that initiate from a pre-meshed geometrical realization of the target geometry that is selectively 'activated'. In this work, the model input consists of the sliced and pixelated (based on the resolution of the printer) cross-sections of the target geometry. As a result, the irradiation profile, combined with the polymerization and solidification characteristics, induce the resulting geometry prediction.

The validation of the developed framework is conducted by a direct comparison to printed samples. Although the printed samples show limited reproducibility, the simulated results correctly (both qualitatively and quantitatively) capture the main characteristic features that distinguish the printed samples from the target ones. Considering that the deformation is a direct result of the chemical shrinkage and the underlying linear momentum balance, the model can also be used as a predictive tool for residual stresses—through the constitutive relation. This might prove useful in the design of (complex shaped) geometries with respect to printability, e.g., to prevent the occurrence of cracks/delamination or excessive warpage. In addition, looking ahead, new paths to process optimization are opened as well as pre-manufacturing (digital) compensation of VP-inherent limitations with respect to geometric accuracy.

Future work should focus on alternative parameter identification strategies. Whereas the current work applies an iterative parameter optimization approach, ideally individual parameters should be identified from dedicated experiments. To assess the shape characteristics of printed parts, the current formulation provides accurate results but the underlying stress prediction remains to be validated and, if needed, extended to a visco-elastic formulation. The physical formulation can be further extended by incorporation of temperature effects, or by accounting for the presence of a (static) powder filler that induces e.g., light scattering and more involved mechanical behavior [131].

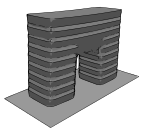

6

Conclusion and outlook

To address the main challenges in the printing of ceramics, in particular the limited feasible component size and wall thickness, as well as the development of defects and cracks, an improved understanding of the manufacturing process is key. The goal of this thesis was to develop a physically based description of the mechanical properties of the printed component through a dedicated computational multi-scale model. As the vat photopolymerization process (applied to ceramics) was not new in itself, from a modeling point of view, there already existed a certain starting point.

Cure-threshold models exist that—based on a certain energy input and, if a powder filled resin is considered, with additional slurry dependent parameters—predict the contour of the solidified region [31, 40–43, 54]. Yet, the binary not-cured/cured origin of this model does not allow to track the evolution of mechanical properties. Alternatively, the existence of sophisticated photopolymerization models serves as a valuable starting point, but their predictive value is limited to the degree of conversion, i.e. nuance in uncured to cured, for unfilled resins [66–76]. By accounting for numerous and detailed physical descriptions, e.g., the species balance and mass transfer of different dissolved components, an excellent correspondence to experimentally obtained cure profiles is found, but the applicability is typically limited to a (few) (two-dimensional) layer(s). Finally, most finite element based methods (applicable to a broad range of additive manufacturing techniques) are suitable for component-scale simulations only. Using an effective (thermo-chemical) strain, which is homogeneous over the layer thickness, allows for a coarse discretization that accounts for a large number of layers efficiently. The applicability is however limited to a single combination of resin/slurry formulation and printing process conditions, e.g., layer thickness and irradiation strategy, after (empirical) determination of a tailored parameter set. Because the target geometry is typically pre-meshed, the predictive value of these approaches—if any—resides in the resulting deformation, not in the distinctive process induced features, e.g., print-through.

To advance the current state-of-the-art of the ceramic vat photopolymerization

process and develop a tailored numerical framework for that purpose, a number of research questions (RQs) have been defined in the Introduction (Section 1.2 – p. 9). In the following, the key concepts and results of this thesis are discussed in relation to these RQs, after which some pending questions, challenges and perspectives for future research are given.

6.1 Conclusions

- In order to capture the numerous relevant physical phenomena in the vat photopolymerization process with appropriate detail, a multi-physical model has been developed (Chapters 2 and 4). The model accounts for irradiation, and the evolution of conversion, temperature and mechanical properties (RQ. I).

- The presence of the inclusions has a profound influence that can not be ignored in the vat photopolymerization process (RQ. II). The most obvious effect is the light scattering induced by the difference in refractive index of the filler and matrix material (RQ. I). The complexity in capturing this effect lies in the high volume fraction of powder filler—which implicates so-called multiple scattering, in contrast to more common single-scattering processes for dilute suspensions—and the small difference in relevant length-scales, i.e. the particle diameter and the wavelength of the UV light. In order to accurately capture the light scattering phenomenon, a wave description of light is essential. This is accomplished through a finite element formulation of Maxwell's electromagnetics equations.

- Due to the gap between the time-scale of light propagation and other process conditions, such as laser movement and the emanating kinetics, the time of the photon passing through a layer is not of interest (RQ. IV). To efficiently capture the response to a single-wavelength light source, the time-harmonic formulation of an electromagnetic field is applied to arrive at the resulting steady-state intensity profile.

- The wave description of light imposes strict requirements on the discretization of the finite element mesh. In order to fully resolve the wavelength (cf. the Nyquist theorem) ~10 elements are necessary. This severely limits the applicability to large slurry areas or volumes (RQ. IV) and motivates the introduction of a multi-scale model in Chapter 4.

- Light scattering phenomena are found to induce a highly spatially inhomogeneous solidification (RQ. II). This has clear implications on the induced spatial conversion profile and the connected evolution of mechanical properties (Chapter 2). A possibly important consequence might be locally extant uncured resin, which is hard to evaluate experimentally.

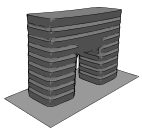

- To quantify the inhomogeneity in the intensity field induced by the presence of the inclusions and their effect on the resulting conversion, two parameters were introduced, i.e. the *intensity inhomogeneity*, $\mathcal{I}_I$, and the *conversion based intensity effectiveness*, $\mathcal{E}_p$ (RQ. II, Chapter 3).

  A parametric study using these parameters on various polygon-based inclusion shapes showed that in a multiple scattering situation there is no clear dependence on the particle geometry, with respect to the intensity inhomogeneity and conversion effectiveness (RQ. III, Chapter 3). It should be noted that this influence is found for the single scattering case, which illustrates the relevance of accounting for the more realistic multiple scattering case.

- A parametric study comparing the results of various polygon geometries to equivalent (three-dimensional) revolved shapes revealed that the two-dimensional results already have a clear predictive value (RQ. III, Chapter 3). Consequently, after translating the powder volume fraction to an equivalent filling fraction, the two-dimensional setting is applied to characterize scattering during (laser) irradiation (RQ. IV, Chapter 4).

- The experimentally found broadening of the solidified contour for filler resins is to a large extent induced by the randomness in the spatial distribution of the ceramic inclusions (RQ. II). In a fictitious scenario where the inclusions are included in a highly repetitive periodic stacking, this phenomenon is expected to diminish (Chapter 2).

- The modeling framework captures the increased residual stresses due to the presence of solid-like inclusions. As far as the temperature evolution is concerned, the inclusions act as a heat sink, slightly reducing the temperature rise due to the exothermic photopolymerization reaction (RQ. III, Chapter 3).

- Throughout this thesis a common type of ceramic is used, i.e. alumina (Al_2O_3). Besides the commonality of alumina, this choice is further motivated because it is not trivial from a modeling perspective, due to its significant refractive index contrast with the resin. The numerical framework is, however, applicable to a broad range of materials by incorporation of the corresponding (optical, thermal, mechanical) material properties.

- To enable full process simulations that account for the presence of the inclusions, a multi-scale modeling framework is proposed (RQ. IV). The offline micro- and meso-scale simulations provide effective material and scattering properties, respectively, used as input in the macro-scale component vat photopolymerization process simulation (Chapter 4).

- Through the multi-physical and multi-scale modeling, the resulting component's quality can be predicted (RQ. V). This is enabled by directly relating material

parameters, i.e. opto-chemo-thermo-mechanical properties, and process conditions, e.g., irradiation strategy, to the development of residual stresses and deformations (Chapter 4).

- To extract effective properties from the micro- and meso-scale, different homogenization approaches are applied (RQ. V, Chapter 4). The micro-to-macro scale transition follows a traditional first-order approach that ensures consistency in internal virtual work and entropy for the mechanical and thermal problem, respectively. The meso-to-macro transition is based on a scaling (that conserves input energy and conversion effectiveness) of the optical and chemical parameters of an unfilled resin. These apparent properties are extracted based on the meso-scale simulation of light scattering.

- Using an immersed simulation setting, where the resin/slurry vat inside which the part fits is accounted for, facilitates the prediction of the resulting component's geometry including its distortion/defects (RQ. V). A key enabling aspect in this analysis is the irradiation strategy, which is applied as the driving model input. In the modeling framework, this is done using sliced two-dimensional cross sections—that would normally be sent to the AM apparatus—defining a planned laser scanning path (Chapter 4) or a pixelized irradiation profile (Chapter 5).

- When attempting to print fine-featured (small) components, knowledge of the irradiation characteristics is crucial (RQ. V). This holds for both laser-scanning and projection based systems. For the former this is simply related to the achievable resolution of the target geometry (Chapter 4), but for the latter this has a more pronounced influence because the number of active adjacent pixels defines the (curvature of the) resulting shape (Chapter 5). The use of significant overlap between pixels can even prevent a small area from solidifying.

- To efficiently determine the result of the accumulated intensity of all individual (active) pixels, the numerical framework applies a linear interpolation scheme (Chapter 5). This is used to relate an independent and predetermined intensity field to the intensity inside the integration points (which is the point inside a discrete element at which all integrals are evaluated). As a result, the resolution of the intensity field is independent on the underlying finite element mesh and looping over all integration points can be done efficiently, i.e. without looping over all active pixels for each integration point, for every iteration.

- The macro-scale model (for unfilled resins) is qualitatively validated through a full three-dimensional comparison of simulated results with printed samples (Chapter 5). Characterization of the geometry of the printed polymer samples is performed through (micro-)CT imaging. The resulting three-dimensional model compares conveniently to the contours of the simulation result. Even

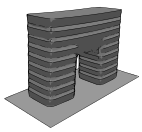

though various simplifying modeling assumptions can be identified, the modeling framework shows its clear predictive value (RQ. V).

6.2 *Remaining questions, challenges, and perspectives on future research*

- The profound influence of the ceramic powder in the vat photopolymerization process for ceramics was delineated in this work, starting from the light propagation through the slurry. From a modeling point of view, capturing the relevant light scattering phenomena using the finite element method has proven to be a bottleneck for application to three-dimensional multiple-scattering conditions. Research into alternative predictive techniques is eminent for the improvement of the understanding of powder filled vat photopolymerization. Key to those methods is that they should provide near-field information and account for absorption of the resin (and inclusions) and for high solid loading. A possible candidate worth considering is the multi-sphere T-matrix method [39].

- In any numerical model/framework a (debatable) balance exists between the level of detail and the computational feasibility. Micro-scale modeling, for example, typically allows for detailed physical descriptions. Throughout this work, the numerical implementation tends more towards a phenomenological approach. In order to further investigate the influence of specific process parameters and material formulations, a higher level of detail is required in the mathematical description of the relevant physics. A large list of possibilities would further refine and increase the complexity of the multi-physical process, but the most prominent candidates to be considered are within the field of conversion and solidification. Notable examples here are the concentration of absorbing species, e.g., photobleaching of the initiator [71–73], a changing refractive index [17, 101] or inhibitor species affecting the photopolymerization reaction [70, 159] and visco-elastic material behavior [107–109]. The separated implementation of individual physics in the modeling framework facilitates a straightforward extension to incorporate the aforementioned (more complex) models.

- The current macro-scale modeling approach proved feasible for the simulation of small physical components. For the prediction of samples of more layers spanning a larger area, exploiting the current implementation was no longer feasible in terms of its computational effort. Different standard/common optimizing modifications are however applicable to this implementation [133], e.g., parallelization, mesh coarsening or reduced order modeling. For the simulation of AM in general, however, the focus should be directed towards inventive principles that account for the addition of material (layers), the continuously expanding computational domain and the diminishing relevance of previously added layers.

- The developed multi-physical framework follows a continuum description

(through finite elements). As such, the model can predict areas where stress concentrations might occur or where conversion and/or bonding is insufficient—which are therefore prone to cracks or debonding. However, in its current form the model is unable to assess the severity of these phenomena. Possible extensions to incorporate debonding and cracking are a cohesive zone approach or a phase-field damage approach, respectively.

- From a validation perspective, the qualitative validation in Chapter 5 is not all-encompassing with respect to the multi-scale modeling framework for vat photopolymerization of ceramics. It provides a clear indication that the multi-physical approach facilitates the prediction of the component's geometry. However, the quality of the component is also related to the homogeneity of the conversion, the corresponding residual stresses and (other) ceramic powder induced phenomena, such as light scattering. The identification/validation of there aspects requires additional experimental efforts.

- The ability to predict the deviation of the printed geometry in comparison to the target geometry enables a pre-manufacturing corrective step. Through the application of an optimization approach that incorporates process physics, the printer input can be tailored to prevent unintended deviations, such that the printed component converges to the target geometry. This is referred to as *inverse modeling* and should encompass optimization of both geometrical deformations and irradiation characteristics.

- The collaboration described in Section 1.2 can be even more fruitful by combining the insights and translating them into practical applications for future vat photopolymerization equipment. Regarding the research in this work, this would require a translation of the multi-physical and multi-scale numerical framework towards more mathematical (feed-forward) closed-loop control oriented models. A possible direction to pursue in this regard is to integrate degree of polymerization sensors in the machine and couple these to predictive models, in order to influence the resulting quality in a targeted way [62, 150, 151].

- From the moment the printing of green ceramics products is no longer a challenge, the post-processing process automatically becomes interesting again. Even after printing seemingly qualitatively satisfactory components, damage might still occur in the debonding and/or sintering process. Although there is a lot of knowledge available from the similar (post-) process for injection molding, the influence of the printing process needs to be investigated. A possibly related issue is, for example, the influence of the recoating step on the distribution of particles through a layer. The current work assumes a homogeneous spread, but statistical deviations in general matter here.

A

Orientation dependence in 3D

The orientation dependent results corresponding to Fig. 3.11 are displayed in Fig. A.1 and Fig. A.2 for $\mathcal{I}_I$ and $\mathcal{E}_p$, respectively. The polar graphs show the orientation of the 3- and 1-axis, i.e. the local inclusion axis initially aligned with the z- and x-axis, respectively. The marker sizes are scaled with the $\mathcal{I}_I$ and $\mathcal{E}_p$-value (corresponding to the marker color) such that the overlapping values are still uniquely visible. Note that the scales of the colorbar are not uniform to emphasize the orientation dependence. For the comparison between individual shapes, the reader is referred to Fig. 3.11.

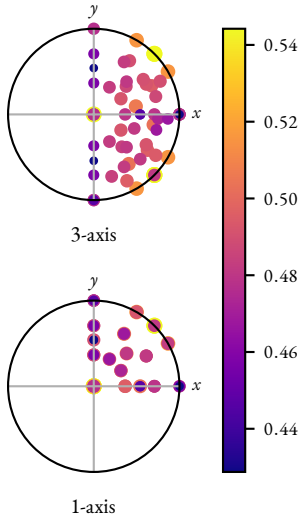

(a) Hexahedron (Fig. 3.9a)

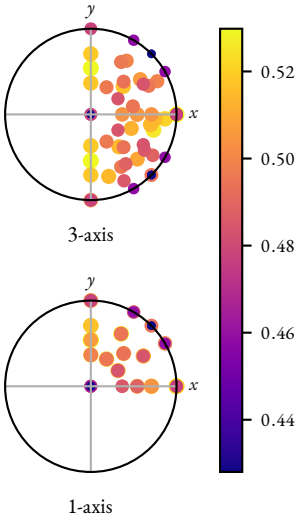

(b) Octahedron (Fig. 3.9b)

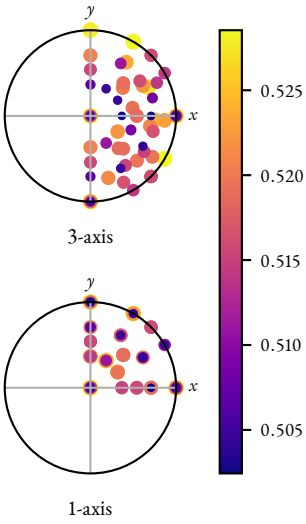

(c) Dodecahedron (Fig. 3.9c)

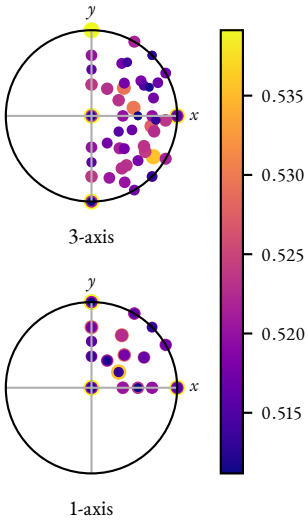

(d) Icosahedron (Fig. 3.9d)

Figure A.1 Orientation dependent $\mathcal{I}_I$ for the platonic shapes. The magnitude of $\mathcal{I}_I$ is displayed for the orientation of the 3- and 1-axis (i.e. the axes initially coinciding with the the global x- and y-axis) using an equal area projection on the xy-plane.

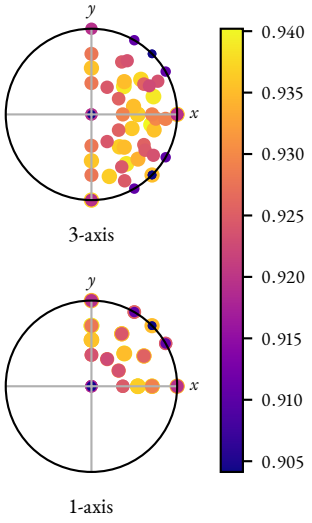

(a) Hexahedron (Fig. 3.9a)

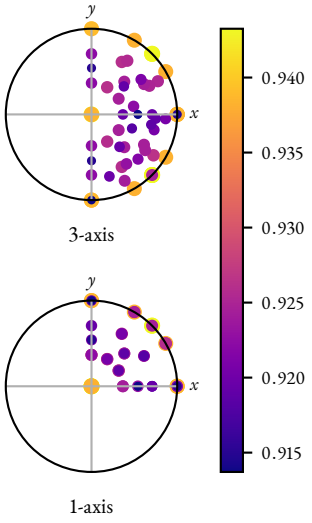

(b) Octahedron (Fig. 3.9b)

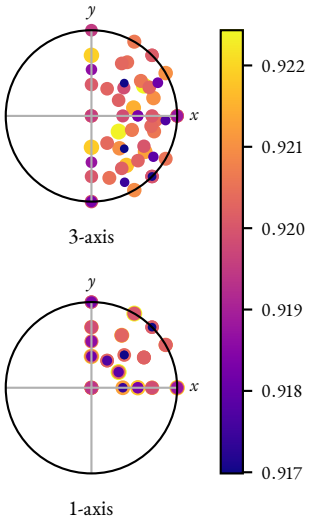

(c) Dodecahedron (Fig. 3.9c)

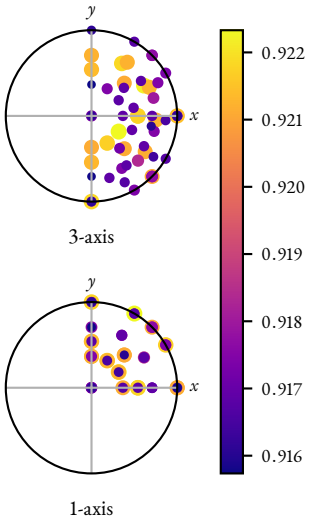

(d) Icosahedron (Fig. 3.9d)

Figure A.2 Orientation dependent $\mathcal{E}_p$ for the platonic shapes. The magnitude of $\mathcal{E}_p$ is displayed for the orientation of the 3- and 1-axis (i.e. the axes initially coinciding with the the global x- and y-axis) using an equal area projection on the xy-plane.

B

Confidence in effective properties

The matrix components of the thermal expansion, chemical shrinkage and thermal conductivity are provided in Figs. B.1a to B.1c, respectively. A box-plot is depicted with the individual values of the realizations depicted by the overlayed circles.

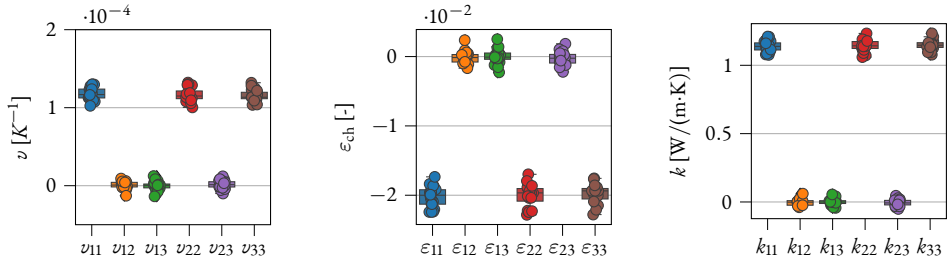

(a) Thermal expansion **(b)** Chemical shrinkage **(c)** Thermal conductivity

Figure B.1 Symmetric thermal expansion, chemical shrinkage and thermal conductivity components.

The derived mean effective stiffness from which the isotropic elastic properties are extracted at final conversion equals

$$D = \begin{bmatrix} 1.25 \cdot 10^{10} & 5.97 \cdot 10^{9} & 5.92 \cdot 10^{9} & -1.20 \cdot 10^{8} & 1.26 \cdot 10^{7} & -7.71 \cdot 10^{6} \\ & 1.25 \cdot 10^{10} & 5.98 \cdot 10^{9} & 9.10 \cdot 10^{7} & -2.52 \cdot 10^{7} & -7.90 \cdot 10^{6} \\ & & 1.26 \cdot 10^{10} & -1.20 \cdot 10^{7} & -8.94 \cdot 10^{7} & 2.98 \cdot 10^{7} \\ & & & 3.49 \cdot 10^{9} & 9.98 \cdot 10^{5} & 2.64 \cdot 10^{6} \\ & & & & 3.54 \cdot 10^{9} & -1.27 \cdot 10^{7} \\ & & & & & 3.47 \cdot 10^{9} \end{bmatrix}. \tag{B.1}$$

Bibliography

1. Carter, C. B. & Norton, M. G. *Ceramic Materials* doi:10.1007/978-1-4614-3523-5 (Springer New York, New York, NY, 2013).
2. Riedel, R. & Chen, I.-W. *Ceramics Science and Technology, Volume 2, Materials and Properties* (WILEY-VCH Verlag GmbH & Co., Weinheim, 2010).
3. Janssen, R., Scheppokat, S. & Claussen, N. Tailor-made ceramic-based components-Advantages by reactive processing and advanced shaping techniques. *Journal of the European Ceramic Society* **28,** 1369–1379 (2008).
4. Evans, J. Seventy ways to make ceramics. *Journal of the European Ceramic Society* **28,** 1421–1432 (Jan. 2008).
5. Leo, S., Tallon, C., Stone, N. & Franks, G. V. Near-Net-Shaping Methods for Ceramic Elements of (Body) Armor Systems. *Journal of the American Ceramic Society* **97,** 3013–3033 (2014).
6. Klocke, F. Modern Approaches for the Production of Ceramic Components. *Journal of the European Ceramic Society* **17,** 457–465 (1997).
7. He, R. *et al.* Fabrication of complex-shaped zirconia ceramic parts via a DLP- stereolithography-based 3D printing method. *Ceramics International* **44,** 3412–3416 (2017).
8. Díaz Lantada, A. *et al.* Monolithic 3D labs- and organs-on-chips obtained by lithography-based ceramic manufacture. *International Journal of Advanced Manufacturing Technology* **93,** 3371–3381 (2017).
9. Melchels, F. P., Feijen, J. & Grijpma, D. W. A review on stereolithography and its applications in biomedical engineering. *Biomaterials* **31,** 6121–6130 (Aug. 2010).
10. Chartier, T. *et al.* Additive manufacturing to produce complex 3D ceramic parts. *Journal of Ceramic Science and Technology* **6,** 95–104 (2015).
11. Bian, W. *et al.* Design and fabrication of a novel porous implant with pre-set channels based on ceramic stereolithography for vascular implantation. *Biofabrication* **3.** doi:10.1088/1758-5082/3/3/034103 (2011).
12. Felzmann, R. *et al.* Lithography-based additive manufacturing of cellular ceramic structures. *Advanced Engineering Materials* **14,** 1052–1058 (2012).
13. Shah, P., Racasan, R. & Bills, P. Comparison of different additive manufacturing methods using computed tomography. *Case Studies in Nondestructive Testing and Evaluation* **6,** 69–78 (2016).
14. Scheithauer, U., Schwarzer, E., Moritz, T. & Michaelis, A. Additive Manufacturing of Ceramic Heat Exchanger: Opportunities and Limits of the Lithography-Based Ceramic Manufacturing (LCM). *Journal of Materials Engineering and Performance* **27,** 14–20 (2018).
15. Travitzky, N. *et al.* Additive manufacturing of ceramic-based materials. *Advanced Engineering Materials* **16,** 729–754 (2014).
16. Zocca, A., Colombo, P., Gomes, C. M. & Günster, J. Additive manufacturing of ceramics: Issues, potentialities, and opportunities. *Journal of the American Ceramic Society* **98,** 1983–2001 (2015).
17. Eckel, Z. C. *et al.* Additive manufacturing of polymer-derived ceramics. *Science* **351,** 58–62 (2016).
18. Schweiger, J., Bomze, D. & Schwentenwein, M. 3D Printing of Zirconia–What is the Future? *Current Oral Health Reports* **6,** 339–343 (2019).
19. Gibson, I., Rosen, D. & Stucker, B. *Additive Manufacturing Technologies* 10–12. doi:10.1007/978-1-4939-2113-3 (Springer New York, New York, NY, 2015).

20. Tian, X., Sun, B., Heinrich, J. G. & Li, D. Scan pattern, stress and mechanical strength of laser directly sintered ceramics. *International Journal of Advanced Manufacturing Technology* **64,** 239–246 (2013).
21. Deckers, J., Vleugels, J. & Kruth, J. P. Additive manufacturing of ceramics: A review. *Journal of Ceramic Science and Technology* **5,** 245–260 (2014).
22. Sing, S. L. *et al.* Direct selective laser sintering and melting of ceramics: a review. *Rapid Prototyping Journal* **23,** 611–623 (2017).
23. Mitteramskogler, G. *et al.* Light curing strategies for lithography-based additive manufacturing of customized ceramics. *Additive Manufacturing* **1,** 110–118 (2014).
24. Wu, H. *et al.* Fabrication of dense zirconia-toughened alumina ceramics through a stereolithography-based additive manufacturing. *Ceramics International* **43,** 968–972 (2017).
25. Hafkamp, T., van Baars, G., de Jager, B. & Etman, P. *A trade-off analysis of recoating methods for VAT photopolymerization of ceramics* in *28th Annual International Solid Freeform Fabrication Symposium: an Additive Manufacturing Conference* (2017), 687–711.
26. Zakeri, S., Vippola, M. & Levänen, E. A comprehensive review of the photopolymerization of ceramic resins used in stereolithography. *Additive Manufacturing* **35,** 101177 (2020).
27. Hinczewski, C., Corbel, S. & Chartier, T. Ceramic suspensions suitable for stereolithography. *Journal of the European Ceramic Society* **18,** 583–590 (1998).
28. Johansson, E., Lidström, O., Johansson, J., Lyckfeldt, O. & Adolfsson, E. Influence of Resin Composition on the Defect Formation in Alumina Manufactured by Stereolithography. *Materials* **10,** 11 (2017).
29. Xing, H. *et al.* Preparation and characterization of UV curable Al_2O_3 suspensions applying for stereolithography 3D printing ceramic microcomponent. *Powder Technology* **338,** 153–161 (2018).
30. Tallon, C. & Franks, G. V. Recent trends in shape forming from colloidal processing: A review. *Journal of the Ceramic Society of Japan* **119,** 147–160 (2011).
31. Halloran, J. W. Ceramic stereolithography: Additive manufacturing for ceramics by photopolymerization. *Annual Review of Materials Research* **46,** 10.1–10.22 (2016).
32. Uematsu, K. & Uchida, N. in *Ceramic Microstructures* 239–246 (Springer US, Boston, MA, 1998). doi:10.1007/978-1-4615-5393-9_21.
33. Zhou, M. *et al.* Preparation of a defect-free alumina cutting tool via additive manufacturing based on stereolithography – Optimization of the drying and debinding processes. *Ceramics International* **42,** 11598–11602 (2016).
34. Manière, C., Kerbart, G., Harnois, C. & Marinel, S. Modeling sintering anisotropy in ceramic stereolithography of silica. *Acta Materialia* **182,** 163–171 (2020).
35. Schwarzer, E. *et al.* Lithography-based ceramic manufacturing (LCM) – Viscosity and cleaning as two quality influencing steps in the process chain of printing green parts. *Journal of the European Ceramic Society* **37,** 5329–5338 (2017).
36. Ganesh, I. Hydrolysis-induced aqueous gelcasting: The latest concept for net-shape consolidation of ceramics-a review. *Materials and Manufacturing Processes* **27,** 233–241 (2012).
37. Wu, H. *et al.* Effect of the particle size and the debinding process on the density of alumina ceramics fabricated by 3D printing based on stereolithography. *Ceramics International* **42,** 17290–17294 (2016).
38. Mendes, M. J., Tobías, I., Martí, A. & Luque, A. Near-field scattering by dielectric spheroidal particles with sizes on the order of the illuminating wavelength. *J. Opt. Soc. Am. A* **27,** 1221–1231 (2010).
39. Egel, A., Pattelli, L., Mazzamuto, G., Wiersma, D. S. & Lemmer, U. CELES: CUDA-accelerated simulation of electromagnetic scattering by large ensembles of spheres. *Journal of Quantitative Spectroscopy and Radiative Transfer* **199,** 103–110 (2017).

40. Tomeckova, V. & Halloran, J. W. Cure depth for photopolymerization of ceramic suspensions. *Journal of the European Ceramic Society* **30,** 3023–3033 (2010).
41. Gentry, S. P. & Halloran, J. W. Absorption effects in photopolymerized ceramic suspensions. *Journal of the European Ceramic Society* **33,** 1989–1994 (2013).
42. Gentry, S. P. & Halloran, J. W. Depth and width of cured lines in photopolymerizable ceramic suspensions. *Journal of the European Ceramic Society* **33,** 1981–1988 (2013).
43. Gentry, S. P. & Halloran, J. W. Light scattering in absorbing ceramic suspensions: Effect on the width and depth of photopolymerized features. *Journal of the European Ceramic Society* **35,** 1895–1904 (June 2015).
44. Goodner, M. D. & Bowman, C. N. Development of a comprehensive free radical photopolymerization model incorporating heat and mass transfer effects in thick films. *Chemical Engineering Science* **57,** 887–900 (2002).
45. Tian, X., Li, D., Chen, Z. & Zhou, W. Study on the fabrication accuracy of ceramic parts by direct stereolithography. *Virtual and Physical Prototyping* **7,** 195–202 (2012).
46. Chartier, T., Badev, A., Abouliatim, Y., Lebaudy, P. & Lecamp, L. Stereolithography process: Influence of the rheology of silica suspensions and of the medium on polymerization kinetics - Cured depth and width. *Journal of the European Ceramic Society* **32,** 1625–1634 (2012).
47. Fu, X. *et al.* Effect of printing strategies on forming accuracy and mechanical properties of ZrO2 parts fabricated by SLA technology. *Ceramics International.* doi:10.1016/j.ceramint.2019.05.328 (2019).
48. Wu, X. *et al.* Effects of soft-start exposure on the curing characteristics and flexural strength in ceramic projection stereolithography process. *Journal of the European Ceramic Society,* 0–1 (2019).
49. Brodnik, N., Schmidt, J., Colombo, P. & Faber, K. Analysis of Multi-scale Mechanical Properties of Ceramic Trusses Prepared from Preceramic Polymers(Revision Prepared for Additive Manufacturing). *Additive Manufacturing,* 100957 (Nov. 2019).
50. Liu, M. *et al.* Digital light processing of lunar regolith structures with high mechanical properties. *Ceramics International,* 0–1 (2018).
51. Bae, C.-J. & Halloran, J. W. Influence of Residual Monomer on Cracking in Ceramics Fabricated by Stereolithography. *International Journal of Applied Ceramic Technology* **8,** 1289–1295 (Nov. 2011).
52. Patel, M., Braden, M. & Davy, K. Polymerization shrinkage of methacrylate esters. *Biomaterials* **8,** 53–56 (Jan. 1987).
53. Watts, D. C. Reaction kinetics and mechanics in photo-polymerised networks. *Dental Materials* **21,** 27–35 (2005).
54. Jacobs, P. F. *Rapid prototyping & manufacturing: Fundamentals of stereolithography* 434 (Society of Manufacturing Engineers in cooperation with the Computer and Automated Systems Association of SME, Dearborn, MI, 1992).
55. Wu, T. *Theoretical modeling and experimental characterization of stress and crack development in parts manufactured through large area maskless photopolymerization* Ph.D Thesis (Georgia Institute of Technology, 2014).
56. Wu, T. & Das, S. *Theoretical modeling and experimental characterization of stress development in parts manufactured through large area maskless photopolymerization* in *Solid Freeform Fabrication Symposium* (2012), 748–760. doi:10.1017/CBO9781107415324.004.
57. Huang, Y., Leu, M. C., Mazumder, J. & Donmez, A. Additive manufacturing: Current state, future potential, gaps and needs, and recommendations. *Journal of Manufacturing Science and Engineering* **137,** 014001 (2015).
58. Kozhevnikov, A., Kunnen, R. P., van Baars, G. E. & Clercx, H. J. Investigation of the fluid flow during the recoating process in additive manufacturing. *Rapid Prototyping Journal* **26,** 605–613 (Dec. 2019).

59. Kozhevnikov, A., Kunnen, R., van Baars, G. & Clercx, H. Influence of the recoating parameters on resin topography in stereolithography. *Additive Manufacturing,* 101376 (June 2020).
60. Hafkamp, T., van Baars, G., de Jager, B. & Etman, P. A feasibility study on process monitoring and control in vat photopolymerization of ceramics. *Mechatronics* **56,** 220–241 (Dec. 2018).
61. Hafkamp, T., van Baars, G., de Jager, B. & Etman, P. A Classification Scheme for AM Control Strategies: the AM V-model. *Proceedings of the 2018 ASPE and Euspen Summer Topical Meeting - Advancing Precision in Additive Manufacturing* **69,** 161–166 (2018).
62. Hafkamp, T. M., van Baars, G. E., de Jager, A. G. & Etman, L. F. P. Real-time feedback controlled conversion in vat photopolymerization of ceramics: A proof of principle. *Additive Manufacturing.* doi:10.1016/j.addma.2019.06.026 (2019).
63. Chambers, R. S., Guess, T. R. & Hinnerichs, T. D. *A phenomenological finite element model of stereolithography processing* tech. rep. March (Sandia National Labs., Albuquerque, 1996).
64. Huang, Y.-M., Kuriyama, S. & Jiang, C.-P. Fundamental study and theoretical analysis in a constrained-surface stereolithography system. *The International Journal of Advanced Manufacturing Technology* **24,** 361–369 (Sept. 2004).
65. Jiang, C.-P., Huang, Y.-M. & Liu, C.-H. Dynamic finite element analysis of photopolymerization in stereolithography. *Rapid Prototyping Journal* **12,** 173–180 (2006).
66. Fang, N., Sun, C. & Zhang, X. Diffusion-limited photopolymerization in scanning micro-stereolithography. *Applied Physics A: Materials Science and Processing* **79,** 1839–1842 (2004).
67. Tang, Y., Henderson, C. L., Muzzy, J. & Rosen, D. W. *Stereolithography cure process modeling using acrylate resin* in *Proceedings of the Solid Freeform Fabrication Symposium* (Austin, Texas, 2004), 612–623.
68. Kang, H.-W., Park, J. H. & Cho, D.-W. A pixel based solidification model for projection based stereolithography technology. *Sensors and Actuators, A: Physical* **178,** 223–229 (2012).
69. Boddapati, A. *Modeling cure depth during photopolymerization of multifunctional acrylates* MSc Thesis (Georgia Institute of Technology, 2010).
70. Jariwala, A. S. *et al.* Modeling effects of oxygen inhibition in mask-based stereolithography. *Rapid Prototyping Journal* **17,** 168–175 (2011).
71. Ivanov, V. V. & Decker, C. Kinetic study of photoinitiated frontal polymerization. *Polymer International* **50,** 113–118 (2001).
72. Terrones, G. & Pearlstein, A. J. Effects of optical attenuation and consumption of a photobleaching initiator on local initiation rates in photopolymerizations. *Macromolecules* **34,** 3195–3204 (2001).
73. Miller, G. A., Gou, L., Narayanan, V. & Scranton, A. B. Modeling of photobleaching for the photoinitiation of thick polymerization systems. *Journal of Polymer Science, Part A: Polymer Chemistry* **40,** 793–808 (2002).
74. Oh, S. J., Lee, S. C. & Park, S. Y. Photopolymerization and photobleaching of n-butyl acrylate/fumed silica composites monitored by real time FTIR-ATR spectroscopy. *Vibrational Spectroscopy* **42,** 273–277 (2006).
75. Emami, M. M. & Rosen, D. W. *An improved vat photopolymerization cure model demonstrates photobleaching effects* in *Proceedings of the Solid Freeform Fabrication Symposium* (Austin, Texas, 2018), 1940–1952.
76. Tarabeux, J., Pateloup, V., Michaud, P. & Chartier, T. Development of a numerical simulation model for predicting the curing of ceramic systems in the stereolithography process. *Journal of the European Ceramic Society* **38,** 4089–4098 (Sept. 2018).
77. Tomeckova, V. & Halloran, J. W. Predictive models for photopolymerization of ceramic suspensions. *Journal of the European Ceramic Society* **30,** 2833–2840 (2010).
78. Westbeek, S., van Dommelen, J. A. W., Remmers, J. J. C. & Geers, M. G. D. Multiphysical modeling of the photopolymerization process for additive manufacturing of ceramics. *European Journal of Mechanics - A/Solids* **71,** 210–223 (Sept. 2018).

79. Tang, Y., Henderson, C., Muzzy, J. & Rosen, D. W. Stereolithography cure modelling and simulation. *International Journal of Materials and Product Technology* **21,** 255 (2004).
80. Yan, W. *et al.* Multi-physics modeling of single/multiple-track defect mechanisms in electron beam selective melting. *Acta Materialia* **134,** 324–333 (2017).
81. Gan, Z., Liu, H., Li, S., He, X. & Yu, G. Modeling of thermal behavior and mass transport in multi-layer laser additive manufacturing of Ni-based alloy on cast iron. *International Journal of Heat and Mass Transfer* **111,** 709–722 (2017).
82. Schmocker, A. *et al.* Photopolymerizable hydrogels for implants: Monte-Carlo modeling and experimental in vitro validation. *Journal of biomedical optics* **19,** 35004 (2014).
83. Swinehart, D. F. The Beer-Lambert Law. *Journal of Chemical Education* **39,** 333 (July 1962).
84. Fairbanks, B. D., Schwartz, M. P., Bowman, C. N. & Anseth, K. S. Photoinitiated polymerization of PEG-diacrylate with lithium phenyl-2,4,6-trimethylbenzoylphosphinate: polymerization rate and cytocompatibility. *Biomaterials* **30,** 6702–6707 (2009).
85. Leiner, C. *et al.* Multiple interfacing between classical raytracing and wave-optical simulation approaches: a study on applicability and accuracy. *Optics Express* **22,** 16048–16060 (2014).
86. Griffith, M. L. & Halloran, J. W. Scattering of ultraviolet radiation in turbid suspensions. *Journal of Applied Physics* **81,** 2538–2546 (1997).
87. Horvath, H. Gustav Mie and the scattering and absorption of light by particles: Historic developments and basics. *Journal of Quantitative Spectroscopy and Radiative Transfer* **110,** 787–799 (2009).
88. Thiele, E. S. & French, R. H. Light-Scattering Properties of Representative, Morphological Rutile Titania Particles Studied Using a Finite-Element Method. *Journal of the American Ceramic Society* **81,** 469–479 (1998).
89. Liew, S. F., Popoff, S. M., Mosk, A. P., Vos, W. L. & Cao, H. Transmission channels for light in absorbing random media: From diffusive to ballistic-like transport. *Physical Review B - Condensed Matter and Materials Physics* **89,** 1–10 (2014).
90. Jin, J.-M. *The Finite Element Method in Electromagnetics* Third, 876 (John Wiley & Sons, Inc., Hoboken, New Jersey, 2014).
91. Monk, P. *Finite Element Methods for Maxwell's Equations* 464. doi:10.1093/acprof:oso/9780198508885.001.0001 (Oxford University Press, Newark, NJ, 2003).
92. Scharf, T. *Polarized Light in Liquid Crystals and Polymers* 400. doi:10.1002/047007437X (John Wiley & Sons, Inc., Hoboken, NJ, USA, Dec. 2006).
93. Demkowicz, L. *Computing with hp-adaptive finite elements: Volume 1 - One and Two Dimensional Elliptic and Maxwell Problems* 398 (Chapman and Hall/CRC, 2006).
94. *Comsol Multiphysics RF Module User's Guide* tech. rep. (Comsol Multiphysics, 2014).
95. Joannopoulos, J. D., Johnson, S. G., Winn, J. N. & Meade, R. D. *Photonic crystals: molding the flow of light* Second, 286 (Princeton University Press, 2008).
96. Jennings, S. G., Pinnick, R. G. & Gillespie, J. B. Relation between absorption coefficient and imaginary index of atmospheric aerosol constituents. *Applied Optics* **18,** 1368–1371 (1979).
97. Hecht, E. *Optics* 4th ed. (Pearson, San Francisco, CA, 2002).
98. Navid, A. & Pilon, L. Effect of polarization and morphology on the optical properties of absorbing nanoporous thin films. *Thin Solid Films* **516,** 4159–4167 (2008).
99. Odian, G. *Principles of Polymerization* doi:10.1002/047147875X (John Wiley & Sons, Inc., Hoboken, NJ, USA, Jan. 2004).
100. Andrzejewska, E. Photopolymerization kinetics of multifunctional monomers. *Progress in Polymer Science (Oxford)* **26,** 605–665 (2001).
101. Aloui, F., Lecamp, L., Lebaudy, P. & Burel, F. Relationships between refractive index change and light scattering during photopolymerization of acrylic composite formulations. *Journal of the European Ceramic Society* **36,** 1805–1809 (2016).

102. Silikas, N., Al-Kheraif, A. & Watts, D. C. Influence of P/L ratio and peroxide/amine concentrations on shrinkage-strain kinetics during setting of PMMA/MMA biomaterial formulations. *Biomaterials* **26,** 197–204 (Jan. 2005).
103. Loshaek, S. & Fox, T. G. Cross-linked Polymers. I. Factors Influencing the Efficiency of Cross-linking in Copolymers of Methyl Methacrylate and Glycol Dimethacrylates 1. *Journal of the American Chemical Society* **75,** 3544–3550 (July 1953).
104. Flach, L. & Chartoff, R. P. *A Simple Polymer Shrinkage Model Applied to Stereolithography* in *Solid Freeform Fabrication Symposium* (1994), 225–233.
105. Huang, Y.-M. & Jiang, C.-P. Curl distortion analysis during photopolymerisation of stereolithography using dynamic finite element method. *The International Journal of Advanced Manufacturing Technology* **21,** 586–595 (2003).
106. Meuwissen, M. H. H., De Boer, H. A., Steijvers, H. L. A. H., Schreurs, P. J. G. & Geers, M. G. D. Residual stresses in microelectronics induced by thermoset packaging materials during cure. *Microelectronics Reliability* **44,** 1985–1994 (2004).
107. Koplin, C., Jaeger, R. & Hahn, P. A material model for internal stress of dental composites caused by the curing process. *Dental Materials* **25,** 331–338 (2009).
108. Hossain, M. & Steinmann, P. Degree of cure-dependent modelling for polymer curing processes at small-strain. Part I: consistent reformulation. *Computational Mechanics* **53,** 777–787 (2013).
109. Liebl, C., Johlitz, M., Yagimli, B. & Lion, A. Simulation of curing-induced viscoplastic deformation: A new approach considering chemo-thermomechanical coupling. *Archive of Applied Mechanics* **82,** 1133–1144 (2012).
110. Berenger, J.-P. A perfectly matched layer for the absorption of electromagnetic waves. *Journal of Computational Physics* **114,** 185–200 (Oct. 1994).
111. Nedelec, J. C. Mixed finite elements in R3. *Numerische Mathematik* **35,** 315–341 (1980).
112. Pomplun, J., Burger, S., Zschiedrich, L. & Schmidt, F. Adaptive finite element method for simulation of optical nano structures. *Physica Status Solidi (B)* **244,** 3419–3434 (2007).
113. *Comsol Multiphysics User's Guide* (2014).
114. Schäfer, J., Lee, S. C. & Kienle, A. Calculation of the near fields for the scattering of electromagnetic waves by multiple infinite cylinders at perpendicular incidence. *Journal of Quantitative Spectroscopy and Radiative Transfer* **113,** 2113–2123 (2012).
115. Goodner, M. D. & Bowman, C. N. Modeling primary radical termination and its effects on autoacceleration in photopolymerization kinetics. *Macromolecules* **32,** 6552–6559 (1999).
116. Westbeek, S., van Dommelen, J. A. W., Remmers, J. J. C. & Geers, M. G. D. Influence of particle shape in the additive manufacturing process for ceramics. *Computers & Mathematics with Applications* **78,** 2360–2376 (Oct. 2019).
117. Colombo, P., Mera, G., Riedel, R. & Sorarù, G. D. Polymer-Derived Ceramics: 40 Years of Research and Innovation in Advanced Ceramics. *Journal of the American Ceramic Society* **93,** no–no (June 2010).
118. Zhou, W., Li, D. & Chen, Z. The influence of ingredients of silica suspensions and laser exposure on UV curing behavior of aqueous ceramic suspensions in stereolithography. *International Journal of Advanced Manufacturing Technology* **52,** 575–582 (2011).
119. Wu, K. C. & Halloran, J. W. Photopolymerization monitoring of ceramic stereolithography resins by FTIR methods. *Journal of Materials Science* **40,** 71–76 (2005).
120. Nobbs, J. H. Kubelka-Munk Theory and the Prediction of Reflectance. *Review of Progress in Coloration and Related Topics* **15,** 66–75 (1985).
121. Abouliatim, Y., Chartier, T., Abelard, P., Chaput, C. & Delage, C. Optical characterization of stereolithography alumina suspensions using the Kubelka-Munk model. *Journal of the European Ceramic Society* **29,** 919–924 (2009).

122. Liao, H. *Stereolithography Using Compositions Containing Ceramic Powders* PhD Thesis (University of Toronto, 1997), 170.
123. Sun, C. & Zhang, X. The influences of the material properties on ceramic micro- stereolithography. *Sensors And Actuators* **101,** 364–370 (2002).
124. Sun, C. & Zhang, X. Experimental and numerical investigations on microstereolithography of ceramics. *Journal of Applied Physics* **92,** 4796–4802 (2002).
125. Demkowicz, L. & Vardapetyan, L. Modeling of electromagnetic absorption / scattering problems using adaptive finite elements. *Computer Methods in Applied Mechanics and Engineering* **152,** 103–124 (1998).
126. Shin, W. & Fan, S. Choice of the perfectly matched layer boundary condition for frequency-domain Maxwell's equations solvers. *Journal of Computational Physics* **231,** 3406–3431 (2012).
127. Webb, J. P. Application of the finite-element method to electromagnetic and electrical topics. *Reports on Progress in Physics* **58,** 1673–1712 (1995).
128. Urbach, H., Janssen, O., van Haver, S. & Wachters, A. On the modeling of optical systems containing elements of different scales. *Journal of Modern Optics* **58,** 496–508 (2011).
129. Chatterjee, A., Jin, J. M. & Volakis, J. L. Edge-Based Finite Elements and Vector ABC's Applied to 3-D Scattering. *IEEE Transactions on Antennas and Propagation* **41,** 221–226 (1993).
130. Cromwell, P. R. *Polyhedra* 451 (Cambridge University Press, 1997).
131. Westbeek, S., Remmers, J. J. C., van Dommelen, J. A. W. & Geers, M. G. D. Multi-scale process simulation for additive manufacturing through particle filled vat photopolymerization. *Computational Materials Science* **180,** 109647 (July 2020).
132. Wang, X., Jiang, M., Zhou, Z., Gou, J. & Hui, D. 3D printing of polymer matrix composites: A review and prospective. *Composites Part B: Engineering* **110,** 442–458 (2017).
133. Knippenberg, J. J. M., Westbeek, S., Geers, M. G. D. & Remmers, J. J. C. A framework for the thermomechanical analysis of AM processes. *In preparation* (2020).
134. Yang, Y., Li, L. & Zhao, J. Mechanical property modeling of photosensitive liquid resin in stereolithography additive manufacturing: Bridging degree of cure with tensile strength and hardness. *Materials & Design* **162,** 418–428 (Jan. 2019).
135. Sengupta, A., Papadopoulos, P. & Taylor, R. L. A multiscale finite element method for modeling fully coupled thermomechanical problems in solids. *International Journal for Numerical Methods in Engineering* **91,** 1386–1405 (Sept. 2012).
136. Özdemir, I., Brekelmans, W. A. M. & Geers, M. G. D. FE^2 computational homogenization for the thermo-mechanical analysis of heterogeneous solids. *Computer Methods in Applied Mechanics and Engineering* **198,** 602–613 (2008).
137. Berthelsen, R., Denzer, R., Oppermann, P. & Menzel, A. Computational homogenisation for thermoviscoplasticity: application to thermally sprayed coatings. *Computational Mechanics* **60,** 739–766 (2017).
138. Bathe, K.-J. *Finite Element Procedures* Second (Prentice Hall, Pearson Education, Inc., Watertown, MA, 2014).
139. Comini, G., Del Guidice, S., Lewis, R. W. & Zienkiewicz, O. C. Finite element solution of non-linear heat conduction problems with special reference to phase change. *Int. J. num. Meth. Engng.* **8,** 613–624 (1974).
140. Pina, J., Kouznetsova, V. & Geers, M. Thermo-mechanical analyses of heterogeneous materials with a strongly anisotropic phase: the case of cast iron. *International Journal of Solids and Structures* **63,** 153–166 (June 2015).
141. Özdemir, I., Brekelmans, W. A. M. & Geers, M. G. D. Computational homogenization for heat conduction in heterogeneous solids. *International Journal for Numerical Methods in Engineering* **73,** 185–204 (Jan. 2008).

142. Li, X., Hu, K. & Lu, Z. Effect of light attenuation on polymerization of ceramic suspensions for stereolithography. *Journal of the European Ceramic Society* **39,** 2503–2509 (2019).
143. Kloss, C., Goniva, C., Hager, A., Amberger, S. & Pirker, S. Models, algorithms and validation for opensource DEM and CFD-DEM, Progress in Computational Fluid Dynamics, An International Journal. *Progress in Computational Fluid Dynamics* **12,** 140–152 (2012).
144. COMSOL Multiphysics. *Comsol Multiphysics Reference Manual: Version 5.4* tech. rep. (COMSOL, Inc, 2018).
145. Ranellucci, A. & Lenox, J. *Slic3r: G-code generator for 3D printers* 2019.
146. *CloudCompare (version 2.10.1) [GPL software]* GPL Software, 2019.
147. Westbeek, S., Remmers, J. J. C., van Dommelen, J. A. W., Maalderink, H. H. & Geers, M. G. D. Prediction of the deformed geometry of vat photo-polymerized components using a multi-physical modeling framework. *Submitted for publication* (2020).
148. Bartolo, P. & Gaspar, J. Metal filled resin for stereolithography metal part. *CIRP Annals* **57,** 235–238 (2008).
149. Liravi, F., Das, S. & Zhou, C. Separation force analysis and prediction based on cohesive element model for constrained-surface Stereolithography processes. *CAD Computer Aided Design* **69,** 134–142 (2015).
150. Classens, K. H. J., Hafkamp, T. M., Westbeek, S., Remmers, J. J. C. & Weiland, S. Real-Time Nonlinear Tracking Control of Photopolymerization for Additive Manufacturing. *Submitted for publication* (2020).
151. Classens, K. H. J., Hafkamp, T. M., Westbeek, S., Remmers, J. J. C. & Weiland, S. Multiphysical modeling and optimal control of material properties for photopolymerization processes. *Additive Manufacturing,* 101520 (Aug. 2020).
152. Narahara, H., Tanaka, F., Kishinami, T., Igarashi, S. & Saito, K. Reaction heat effects on initial linear shrinkage and deformation in stereolithography. *Rapid Prototyping Journal* **5,** 120–128 (1999).
153. Ligon, S. C., Husár, B., Wutzel, H., Holman, R. & Liska, R. Strategies to Reduce Oxygen Inhibition in Photoinduced Polymerization. *Chemical Reviews* **114,** 557–589 (Jan. 2014).
154. Pierrel, J., Ibrahim, A., Croutxé-Barghorn, C. & Allonas, X. Effect of the oxygen affected layer in multilayered photopolymers. *Polym. Chem.* doi:10.1039/C7PY00974G (2017).
155. Lin, J. T., Liu, H. W., Chen, K. T. & Cheng, D. C. Modeling the Kinetics, Curing Depth, and Efficacy of Radical-Mediated Photopolymerization: The Role of Oxygen Inhibition, Viscosity, and Dynamic Light Intensity. *Frontiers in Chemistry* **7,** 1–14 (2019).
156. Christmann, J., Ley, C., Allonas, X., Ibrahim, A. & Croutxé-Barghorn, C. Experimental and theoretical investigations of free radical photopolymerization: Inhibition and termination reactions. *Polymer* **160,** 254–264 (2019).
157. Hughes, T. J. R. *The Finite Element Method: Linear Static and Dynamic Finite Element Analysis* 1st ed., 704 (Dover Publications, 2000).
158. De Borst, R., Crisfield, M. A., Remmers, J. J. C. & Verhoosel, C. V. *Non-Linear Finite Element Analysis of Solids and Structures* Second, 540. doi:10.1002/9781118375938 (John Wiley & Sons, Ltd, Chichester, UK, Aug. 2012).
159. Metral, B., Bischoff, A., Ley, C., Ibrahim, A. & Allonas, X. Photochemical Study of a Three-Component Photocyclic Initiating System for Free Radical Photopolymerization: Implementing a Model for Digital Light Processing 3D Printing. *ChemPhotoChem* **3,** 1109–1118 (2019).
160. Flach, L. & Chaftoff, R. P. A Process Model for Nonisothermal Photopolymerization With a Laser Light Source. I: Basic Model Development. *Polymer Engineering & Science* **35,** 483–492 (1995).
161. Bennett, J. Measuring UV curing parameters of commercial photopolymers used in additive manufacturing. *Additive Manufacturing* **18,** 203–212 (2017).

162. Decker, C. & Jenkins, A. D. Kinetic Approach of O2 Inhibition in Ultraviolet and Laser Induced Polymerizations. *Macromolecules* **18,** 1241–1244 (1985).
163. Bikas, H., Stavropoulos, P. & Chryssolouris, G. Additive manufacturing methods and modelling approaches: a critical review. *The International Journal of Advanced Manufacturing Technology* **83,** 389–405 (2016).
164. Gouge, M. F. & Michaleris, P. *Thermo-Mechanical Modeling of Additive Manufacturing* doi:10 . 1016/c2016-0-00317-0 (Elsevier, 2018).
165. Pang, T. H., Guertin, M. D. & Nguyen, H. D. Accuracy of Stereolithography Parts: Mechanism and Modes of Distortion for a "Letter-H" Diagnostic Part. *Solid freeform Fabrication Proceedings,* 170–180 (1995).
166. Huang, Y. M., Jeng, J. Y. & Jiang, C. P. Increased accuracy by using dynamic finite element method in the constrain-surface stereolithography system. *Journal of Materials Processing Technology* **140,** 191–196 (2003).
167. Koplin, C., Gurr, M., Mülhaupt, R. & Jaeger, R. Shape accuracy in stereolithography: a material model for the curing behavior of photo-initiated resins. *International User's Conference on Rapid Prototyping & Rapid Tooling & Rapid Manufacturing (Euro-uRapid), Berlin* (2008).
168. Xu, K. & Chen, Y. Mask Image Planning for Deformation Control in Projection-Based Stereolithography Process. *Journal of Manufacturing Science and Engineering* **137,** 031014 (2015).
169. Goodner, M. D., Lee, H. R. & Bowman, C. N. Method for Determining the Kinetic Parameters in Diffusion-Controlled Free-Radical Homopolymerizations. *Industrial & Engineering Chemistry Research* **36,** 1247–1252 (1997).
170. Wu, D., Zhao, Z., Zhang, Q., Qi, H. J. & Fang, D. Mechanics of shape distortion of DLP 3D printed structures during UV post-curing. *Soft Matter* **15,** 6151–6159 (2019).

List of publications

- Westbeek, S., van Dommelen, J. A. W., Remmers, J. J. C. & Geers, M. G. D. Multiphysical modeling of the photopolymerization process for additive manufacturing of ceramics. *European Journal of Mechanics - A/Solids* **71,** 210–223 (Sept. 2018)

- Westbeek, S., van Dommelen, J. A. W., Remmers, J. J. C. & Geers, M. G. D. Influence of particle shape in the additive manufacturing process for ceramics. *Computers & Mathematics with Applications* **78,** 2360–2376 (Oct. 2019)

- Westbeek, S., Remmers, J. J. C., van Dommelen, J. A. W. & Geers, M. G. D. Multi-scale process simulation for additive manufacturing through particle filled vat photopolymerization. *Computational Materials Science* **180,** 109647 (July 2020)

- Classens, K. H. J., Hafkamp, T. M., Westbeek, S., Remmers, J. J. C. & Weiland, S. Multiphysical modeling and optimal control of material properties for photopolymerization processes. *Additive Manufacturing,* 101520 (Aug. 2020)

- Classens, K. H. J., Hafkamp, T. M., Westbeek, S., Remmers, J. J. C. & Weiland, S. Real-Time Nonlinear Tracking Control of Photopolymerization for Additive Manufacturing. *Submitted for publication* (2020)

- Westbeek, S., Remmers, J. J. C., van Dommelen, J. A. W., Maalderink, H. H. & Geers, M. G. D. Prediction of the deformed geometry of vat photo-polymerized components using a multi-physical modeling framework. *Submitted for publication* (2020)

- Knippenberg, J. J. M., Westbeek, S., Geers, M. G. D. & Remmers, J. J. C. A framework for the thermomechanical analysis of AM processes. *In preparation* (2020)

Acknowledgments

Truth be told; I never expected to get to a point where I (am about to) finish the PhD trajectory. At the same time, however, it ís a dream come true to arrive at this point. Even though about four and a half years ago I had no idea—or even the intention—that I might embark on this journey, I am truly glad that I did. It is often claimed that the PhD (and research in general) has its 'ups' and 'downs'; fortunately I have only been able to experience this trajectory, despite the hard work required, as an 'up'. A lot of fantastic people have contributed to—or even enabled—this and I would like to thank them below.

Being the first in our research group (Mechanics of Materials – MoM) dealing with 3D printing has clear advantages. The most prominent of these is my supervision dream-team of first promoter **Marc** and co-promoters **Hans** and **Joris**. Right from the start it was clear that the project posed many interesting challenges that were slightly outside our usual comfort zone and that we all were eager to tackle. I experienced our weekly/monthly progress meetings—and especially the dynamics within them—as delightful, highly constructive, yet always with a healthy dose of criticism. Outside those (scheduled) meetings, you were all also easily approachable; both in the corridor, coffee corner and via e-mail. Whenever we set a goal you were all very accommodating to reach it, including, e.g., same evening or over-weekend article reviews. Such dedication is incredibly inspiring and motivating. The above praise was not entirely surprising, as I completed my bachelor's degree with Hans (and Johan), and my master's project with Joris. I would like to thank Joris for convincing me to pursue a philosophical degree through this project. Even though you were well aware that I had no intention of striving for a career in academia, you recognized the fit between me and the project and the potential of a PhD for my future career. Within the same context, my thanks also go to **Tom Engels** and **Leon van Gerwen**.

Especially in the initial phase of the project, my TNO colleagues were of great value in navigating the world of additive manufacturing and getting a good feel for general practices and challenges in the field. My special thanks go to **Gregor**, **Tessa**, **Rik**, **Fidel**, **Kun**, **Marc**, **Edwin**, **Erwin**, **Fabien** and last, but definitely not least, **Hessel** (our collaboration even resulted in a very nice final paper). To capture the multi-physical character of the printing process, I found the discussion with TU/e colleagues **Martijn van Beurden** and **Rob Mestrom** from the Electromagnetics research group very useful.

To my academic brothers, **Thomas** (from the Control Systems Technology research group; we even share our PhD start and defense date) and **Andrei** (from the research group Fluids and Flows); we made a great CerAM team. Most of all, I would like to say that it is a pity that we have not really been able (time-wise) to integrate our research

projects into the ideal ceramic-AM equipment. Our quarterly meetings, with numerous **knowledgeable supporters**, were extremely useful, particularly to see the whole project in a broader picture. What the audience usually recognized as the 'battle of the graphics' was proper motivation to produce high-quality presentations during our sessions and elsewhere. I would also like to thank **Hoi-Yan** for ensuring our research gets the exposure it deserves.

Typically, projects within our research group are either purely numerical or purely experimental—either mostly residing at the fourth floor or in the basement of the Gemini building—which creates a nice competition between practitioners from both categories. This project was originally, and for most of its duration, intended to be purely numerical. Consequently, it came as a surprise to pretty much everyone when I knocked on the door of the Multiscale lab, located in the basement, in the beginning of this year. I want to express my gratitude to all its '**residents**' (it sometimes seemed that severe at least) for making me feel welcome there as well. My sincere thanks go out to **Marc** and **Niels** for supporting and guiding me during my experimental excursion.

I am also very grateful to the students I got to supervise: **Jeroen** (before he became a direct colleague), **Cas**, **Rick**, **Willian**, **Wouter** and **Koen**. Supervising you was deeply rewarding and your work was very valuable in providing increased insight and sometimes even assisted with or resulted in publications. "Petje af", Koen.

I am also very grateful to my **committee** for thoroughly reviewing my manuscript. In addition, I would like to thank **TNO** and the **TU/e High Tech Systems Center** for financing the project (through the **TU/e Impuls** program).

At a greater distance from the project I would like to thank my **office- and MoM-group-mates** and its excellent support team, in the form of **Alice** and **Rachel**. I truly had a great time thanks to all of you. To my 4.13 office mates throughout time; **Rody**, **Stefan**, **Jim**, **Sandra**, **Maqsood**, **Mirka**, **Siavash**, **Salman**, **Mohsen**, **Majido**, **Luv**, **Vahid**, **Job**, **Sven**, **Lei**, **Zülal**, **Jessica**, **Tom**, **Nik**, **Ignasi**; thank you for great discussions at the coffee machine, moral support, great office events and BBQs, "3-uurtjes" and lots of laughs. **Mirka**, you were my esteemed 'Comsol' buddy; **Jeroen**, it was great to share our development journey of 'DAWN-AM' together. To my early-bird coffee/tea buddies **Sandra**, **Rody**, **Sven** and **Zülal**; we had ourselves a great morning routine. **Ondrej**, **Jim**, **Franz**, **Rody**, **Varun**, **Mathieu**, **Vahid**, **Robin**, **Job**, **Niels** and **Tijmen**, and '**Team-AM**' a.k.a. **Jeroen**, **Nicky**, **Tim** and **Bram**; I deeply appreciated our good times at hotels and rented apartments and homes during courses and conferences.

Moving to the beautiful city of Maastricht and its lovely hilly surroundings—that still manage to provide me that holiday-feeling every time—after the first months of my project occasionally provided a (train) commuting challenge. My sincere gratitude is in order for the numerous convenient ánd nice sleep-overs, thank you **Stefan**, **Sven**, **Rody**, and **Vahid** for always providing me with a place to crash.

Furthermore, I am grateful for the valuable people in my life who (also) succeeded in distracting me from the stress that the PhD brings with it. I will keep the list of good friends with whom great times were spent short just by referring to our team names;

many thanks to the '**Taxi Group**', the '**Fenne Fan Club**', '**HEERS**', and '**Snacks + Spellen**'!

I initially hesitated to include the current COVID-19 outbreak in the world in my acknowledgements, but I have come to the conclusion that some words are in order (for future reference). I should firstly acknowledge that I got very lucky. At the time the Netherlands went into lock-down, I had just finished my experiments and only analysis and writing remained. Two things that can easily be done through digitization and from home. Furthermore, the virus has not entered my personal circle—'knock on wood'—and I sincerely hope anyone reading this is equally fortunate. Staying connected with your group-members while mainly working from home is challenging. Thanks to **Joris** for hosting a highly entertaining 'Food Festival'; the recipes that we shared, prepared and discussed in our weekly e-meeting—in order of appearance: **Jeroen**, **Tommaso**, **Joris**, **Tom**, **Britt**, **Bram** and **Ruben**, thank you all!—will certainly return to my kitchen. I also had the privilege of starting my new job in April. Many thanks to my new colleagues for the warm welcome in these strange times and in particular to **Luc Groenen** and **Stijn Berden** for providing me with the flexibility to simultaneously complete my PhD in a proper manner.

To my dear family—technically not (yet) all of you, but I know the feeling is mutual—**Mariëtte**, **Anja** & **René**, **Jelle** & **Ashley**, **Lonneke** & **Kaïn**, **Mathijs** & **Bo**, **Jeanne** & **Giuseppe** and **family located further away**; I consider myself lucky to have you and am thankful for the bond that we have. Thank you for always caring, showing interest and simply being there whenever I needed you. I love our coffees, board/video game nights, sleepovers, weekends, trips, holidays and vacations together.

And finally, to my dearest **Eefje**. I know that whatever I write here you will find cliché and you will deny your contribution; believe me: you have definitely earned your mention here. This ride simply wouldn't have been so smooth without you. You already know whenever something bothers me before I do and then you know how to translate it into such wise words that it surprises (and helps) me over and over again. You've made my life richer in so many ways. You help me realize that happiness is in the little things—like our best fluffy friend **Guus**. You make my heart beat faster and at the same time you are my "beste maatje". For all that and so much more, I am infinitely grateful to you. I look forward to continue shaping our future together!

Steyn Westbeek
Maastricht, August 27th, 2020

Curriculum vitae

Steyn Westbeek was born on the 24th of October 1991 in Tilburg, the Netherlands. After finishing secondary school (VWO) at Theresialyceum in Tilburg in 2009, he enrolled in the Bachelor program of Mechanical Engineering at Eindhoven University of Technology. Steyn received his Bachelor's degree in 2013 while also completing the Technology Management Certificate at the faculty of Industrial Engineering & Innovation Sciences at Eindhoven University of Technology that same year.

Continuing his education he enrolled in the Master program of Mechanical Engineering at the same university. As part of his curriculum, Steyn completed a traineeship at GKN Fokker (Technologies) on "Mori-Tanaka Based Homogenization of a Short Fiber Composite Butt-Joint". In addition to the regular curriculum, Steyn also spent two years as part of the Formula Student team University Racing Eindhoven (URE), in the role of (design) engineer. He received his Master's degree (*with great appreciation*) within the Mechanics of Materials group of prof. dr. ir. Marc Geers in the beginning of 2016 on the thesis entitled "Modeling thermo-mechanical fatigue crack growth using a cohesive zone approach", under the supervision of dr. ir. Joris Remmers and in collaboration with DAF Trucks N.V.

After graduation, Steyn was offered a Ph. D. position in the same research group on the 3D printing of ceramic components. The work entitled "Multi-scale modeling of the additive manufacturing of ceramics by vat photopolymerization", of which the results are presented in this thesis, was supervised by dr. ir. Joris Remmers, dr. ir. Hans van Dommelen and prof. dr. ir. Marc Geers (as 1st promotor), in a collaboration between TU/e High Tech Systems Center and TNO.